Systematic mechanical characterization and micromechanical modelling of woven glass fibre reinforced laminates for PCB applications

Master Thesis

by

Markus Frewein

Submitted to the

Institute of Materials Science and Testing of Polymers

at the Montanuniversitaet Leoben

prepared at

AT&S Austria Technologie & Systemtechnik AG

Thesis supervisor: Dipl.-Ing. Thomas Krivec, Dr.mont. Qi Tao

Academic supervisor: Univ.-Prof. Dr. Gerald Pinter

Leoben, August 2018

EIDESSTATTLICHE ERKLÄRUNG

Ich erkläre an Eides statt, dass ich diese Arbeit selbstständig verfasst, andere als die angegebenen Quellen und Hilfsmittel nicht benutzt und mich auch sonst keiner unerlaubter Hilfsmittel bedient habe.

AFFIDAVIT

I declare in lieu of oath, that I wrote this thesis and performed the associated research myself, using only literature cited in this volume.

LEOBEN, August 2018 **(Markus Frewein)**

ACKNOWLEDGEMENT

First of all, I would like to thank Univ.-Prof. Dr. Gerald Pinter for being my academic supervisor and supporting me during the development of this work. My special thanks go to Dr. Martin Pletz for sharing his know-how in micromechanical modelling and offering valuable advice. I would also like to thank Dipl.-Ing. Peter Guttman for advising me in the field of dynamic mechanical analysis. In addition, I would also like to thank Jürgen Grosser and Gerald Maier for the implementation of the monotonic tensile test at the Institute of Materials Science and Testing of Polymers.

I am thankful to AT&S Austria Technologie & Systemtechnik AG for giving me the opportunity to perform this work. My special thanks go to Thomas Krivec and Qi Tao for advising me. I highly appreciate their valuable input, helpful guidance and friendly support during the development of this work and in general over the last years at AT&S. Particularly, I would like to thank Mr. Hyung Wook Park for providing me the resin material studied in this work. I thank Ms. Anke Steinberger, Dipl.-Ing. Julia Zündel and Ms. Esther Stering for their support regarding the cross sectioning, re-viewing results and implementing experimental methods.

Moreover, I also would like to express my gratitude to my family and friends and especially, Margit, Herbert, Robert and Sandra. Without their love and steady backup, I would not be where I am today.

Finally, I would like to thank Dr. Peter Fuchs who offered me the opportunity to get a start in the world of work.

KURZFASSUNG

Da die Anwendung der Simulation, vor allem jene, der Finiten-Elemente-Methode, in der Leiterplattenindustrie immer mehr an Bedeutung gewinnt, strebt man nach möglichst realistischen Materialmodellen, um zuverlässige Ergebnisse generieren zu können. Dies ist notwendig, um anwendungsbezogene Ergebnisse abzuleiten. Mit der Zielsetzung etwaige Fehlermoden einer Leiterplatte zu identifizieren, werden virtuelle Torsionsversuche, Fallversuche und Thermische Wärme-Wechselversuche durchgeführt. Die neun temperaturabhängigen orthotropen Materialkonstanten der glasfaserverstärkten Laminat-Materialien haben einen wesentlichen Einfluss auf das Simulationsergebnis.

Die vorliegende Masterarbeit befasst sich mit der Optimierung von konventionellen mechanischen Charakterisierungs-Methoden und mikromechanischen Methoden, um die neun orthotopen Konstanten zu bestimmen. Im experimentellen Teil der vorliegenden Studienarbeit wurden drei glasfaserverstärkte Epoxidharz Dielektrikum-Materialien und deren Matrix Harzsystem selbst ausgewählt. Die Laminate und Harzproben wurden in einem automatisierten Fräsverfahren hergestellt. Diese hergestellten Proben wurden im Anschluss systematisch mechanisch charakterisiert. Es folgte die Durchführung monotoner Zugversuche bei erhöhten Temperaturen und die Dynamisch Mechanische Analyse. Ferner wurde die temperaturabhängige Querkontraktionszahl näher untersucht. Der Einfluss der Probenvorbereitung wurde erforscht/analysiert, sowie die unterschiedlichen, gemessenen Modulergebnisse der oben genannten Methoden ebenfalls evaluiert. Um den volumetrischen Harzgehalt der untersuchten Laminate zu ermitteln, wurde die hydrostatische Wägung, sowie die thermogravimetrische Analyse durchgeführt. Es wurden Einheitszellen-Modelle mit den gemessenen Daten als Eingangsparameter in der Finite Elemente Umgebung generiert, um die orthotropen Konstanten im Mikromechanik-Teil zu bestimmen. Die Software Abaqus®/Standard wurde dafür genutzt. Den Einheitszellen wurden unterschiedliche Faserbündel-Geometrien und periodische Randbedingungen zugewiesen. Im Anschluss wurden die Ergebnisse des experimentellen und mikromechanischen Teiles miteinander verglichen, um die jeweiligen Potentiale der einzelnen Methoden zu evaluieren.

Dabei konnte gezeigt werden, dass bei einer gründlich durchgeführten Probenvorbereitung der monotone Zugversuch und die Dynamisch Mechanische Analyse zuverlässige und vergleichbare Ergebnisse generieren. Aus einem experimentellen und numerischen Blickwinkel konnte gezeigt werden, dass die präsentierte Methode brauchbare Ergebnisse

lieferte, um den Harzgehalt der Laminate mithilfe der thermogravimetrischen Analyse zu bestimmen. Die Charakterisierung der Querkontraktionszahl der dünnen Laminat-Proben in der Ebene, stellte sich als überaus anspruchsvoll heraus. Generell konnte gezeigt werden, dass die generierten experimentellen und numerischen Ergebnisse gut übereinstimmen.

ABSTRACT

Since the application of simulation, especially the finite element method, has become more and more significant in the printed circuit board (PCB) industry, realistic material models have become more important. This is necessary to create application related results. For example, virtual torsion tests, drop tests and thermal cycle/shock tests are applied to predict the failures of a PCB. Thereby the nine temperature-dependent orthotropic engineering constants of the woven glass fibre reinforced laminates have a major impact on the simulation outcome.

The present master thesis focuses on the optimization of conventional mechanical characterization methods and micromechanical methods for the determination of the engineering constants. For the experimental part, three different glass fibre reinforced epoxy dielectric materials and their resin matrix were chosen. The laminate and resin specimens were prepared by an automated routing procedure. All of the investigated materials were systematically mechanically characterized by monotonic tensile test at elevated temperatures and dynamic mechanical analysis. In addition, the temperature dependent Poisson's ratio was investigated more closely in this study. A focus was also on the clarification of the different modulus outcome with respect to the mentioned methods and the specimen preparation procedure. The volumetric resin content of the laminates was determined by hydrostatic weighing and thermogravimetry. For the micromechanical part, a unit-cell model was implemented into a finite element environment to predict the engineering constants with the measured data as inputs. Abaqus®/Standard software was the applied numerical tool. Different yarn fibre aspect ratios and periodic boundary conditions were applied to the model. The results from the experimental and micromechanical part were compared to evaluate the potentials of micromechanical methods.

It can be shown that the monotonic tensile test and dynamic mechanical analysis are creating reliable comparable data when preparing the specimens in a proper way. In addition, the presented methodology to determine the resin content by thermogravimetry can produce quite useful results, from an experimental and numerical point of view. In contrast, the characterisation of the in-plane Poisson's ratio at elevated temperatures of thin laminates can be seen as a challenging procedure. However, the obtained numerical results were in a good agreement with the experimental findings.

TABLE OF CONTENTS

1 INTROTUCTION AND OBJECTIVE 3

2 BACKGROUND 5

2.1 PRINTED CIRCUIT BOARDS 5
2.2 EPOXY RESIN 6
2.3 GLASS FIBRE REINFORCED PREPREGS 6
2.4 ORTHOTROPIC MATERIAL PROPERTIES 7
2.5 BASICS OF MEASUREMENT TECHNOLOGY 9
2.5.1 Hydrostatic Weighing 9
2.5.2 Thermogravimetry 9
2.5.3 Uniaxial Tensile Test 10
2.5.4 Digital Image Correlation 11
2.5.5 Dynamic Mechanical Analyses 12
2.6 BASICS OF NUMERICAL METHODS 14
2.6.1 Finite Element Method 14
2.6.2 Periodically Repeating Unit Cell 16

3 MATERIALS AND SPECIMENS 17

3.1 RESIN SPECIMEN PREPARATION 17
3.2 LAMINATE SPECIMEN PREPARATION 19
3.3 SUMMARIZED SPECIMEN INFORMATION 23

4 EXPERIMENTAL 24

4.1 HYDROSTATIC WEIGHING 24
4.2 THERMOGRAVIMETRY 24
4.3 MONOTONIC TENSILE TEST 27
4.3.1 Implementation of the DIC 30
4.4 DYNAMIC MECHANICAL ANALYSIS 31
4.5 CROSS SECTIONING 34

5 NUMERICAL 35

5.1 GENERAL CONSIDERATIONS 35
5.2 MICROMECHANICAL MODELLING 37

6 RESULTS 40

6.1 EXPERIMENTAL RESULTS 40
6.1.1 Evaluation of the Density 40
6.1.2 Evaluation of the Inorganic Filler Content 41

6.1.3 Evaluation of the Poisson's Ratio 43
6.1.4 Evaluation of the Modulus at Different Panel Positions and in 45° Direction 47
6.1.5 Evaluation of the Modulus at Elevated Temperatures 51
6.1.6 Evaluation of the Cross Sectioning 58
6.2 NUMERICAL RESULTS 59
6.2.1 Evaluation of the General RUC Response and the Influence of the Yarn Aspect Ratio 59
6.2.2 Evaluation of the Applied Boundary Condition 61
6.3 VERIFICATION OF NUMERICAL RESULTS 63
6.4 SUGGESTIONS FOR THE FINAL MATERIAL MODEL 65

7 SUMMERY AND OUTLOOK 67

8 LITERATURE 69

APPENDIX 73

1 INTROTUCTION AND OBJECTIVE

Over the recent decades, the trends of miniaturization, increasing interconnect density and new manufacturing technologies in terms of electronic devices pushing engineers and scientists in the electronic industry. These trends have also been pushing negative side effects like causing high local stress concentrations at the component level, which can cause a malfunction in a finished product during application. In addition, the development period of electronic devises from the design phase to the finished product has decreased significantly new, e.g., mobile devices are released annually. Besides, a high reliability assessment is also required to guarantee a certain lifetime of an electronic device (Gschwandl et al, 2016, Moore and Shi, 2014).

Printed circuit boards (PCBs) are electronic components and generally needed in all electronic devices. In order to overcome the above-mentioned challenges, the finite element based simulation is a topic of growing interest in the PCB industry. From the aerospace industry to construction work, the finite element analysis (FEA) is state of the art, while in the PCB industries still not common. This can be attributed to the fact that PCBs are complex geometrical and functional systems and therefore challenging to implement into FEA. Additionally, when implementing a PCB model, the direction dependent material definition of the laminate layers and the highly non-linear behaviour of the copper structures have to be considered to achieve a reasonable simulation output. Besides, the material properties of the laminate layers are also temperature dependent. For example, when performing a virtual FEA based thermal shock test reliability assessment of an assembled PCB, these temperature dependent material properties of the laminates have also to be taken into account (Tao et al., 2018, Zukowski et al., 2015).

In order to model the individual laminate layers accurately, the nine orthotropic engineering constants must be determined. The in-plane parameters of the engineering constants can be obtained with a combination of experimental and analytical approaches. Meanwhile, the out-of-plane components can only be obtained by using a micromechanical approach (Fuchs, 2012). To perform the micromechanical analysis, the properties of the resin matrix of the laminates must be investigated accurately. Hence, the present thesis focuses on the systematic experimental determination of the temperature depended resin and in-plane laminate properties. Additionally, the missing input parameters at room temperature should be evaluated by using a micromechanical approach based on the experimental data. In order to achieve this, three different woven fibreglass dielectric materials from the same

material family with the corresponding epoxy resin matrix were selected and systematically characterised. Finally, a fully orthotropic material model for the implementation into the FEA should be established.

Previous studies at AT&S Hinterberg did not always show reliable results, regarding the reproducibility of the modulus of elasticity, when utilizing the available laboratory press and preparing specimens manually. Therefore another aim of this study was to improve and standardize the specimen preparation methodology. In order to create better and more consistent results, a PCB production press within AT&S was used to laminate the prepreg material. Additionally, an automated routing procedure for resin and laminate specimens was developed.

In the experimental part of this study, the in-plane orthotropic properties were determined, the specimen preparation methodology was evaluated and data for the micromechanical analyses were collected. Investigations regarding the cross sectional view of the fibre bundles and different boundary conditions were conducted in the numerical studies. Moreover, the in-plane properties from the numerical and experimental part were compared and a material model was presented.

2 BACKGROUND

2.1 Printed Circuit Boards

The purpose of a printed circuit board (PCB) is to mechanically support and electrically connect electronic elements. Modern PCBs are made of insulating reinforced plastic and conductive copper layers, whereby the conducting paths are etched onto the copper layers. Figure 2-1 shows a schematic build-up of a PCB. Prepregs (PP) and copper cladded laminates (CCL) representing different reinforced plastics. They can be differentiated into a matrix (epoxy resin) and a glass fibre fabric style. Copper cladded fully cured prepreg layers (one or more layers) are the so-called core materials. The core is usually a big panel. PPs have a curing degree of around 30% (B-staged) and are laminated during the PCB production procedure. The sequence and number of prepreg and core layers vary according to different applications of a PCB. Vias (plated through holes) are electrical connections made of conductive materials which are realized as a metallic drill hole. Figure 2-1 shows three types of vias; the plated through hole (1) passes all the way thru the PCB, the blind via (2) goes from the top layer to an inner layer of the PCB, and the buried via (3) is inside the PCB (Coombs, 2001, Tao, 2018).

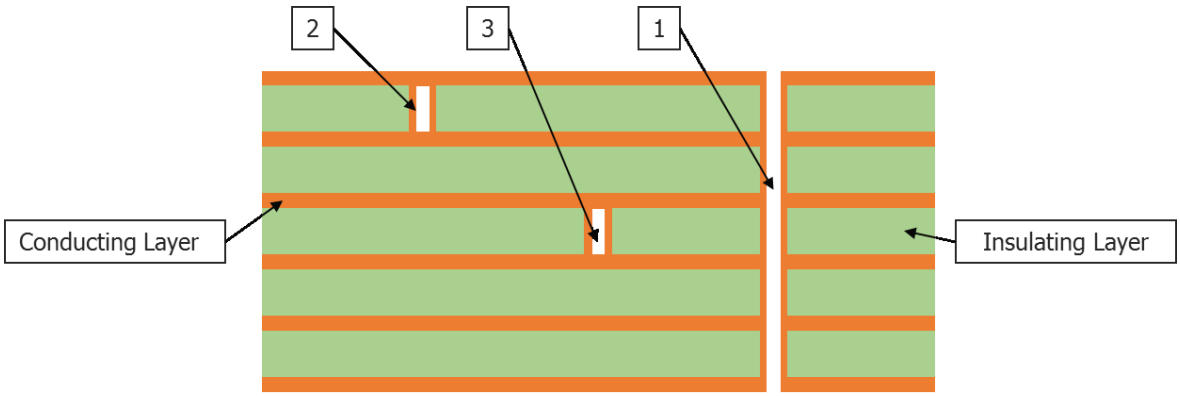

Figure 2-1: Schematic cross section view of a multilayer PCB, displayed with alternating conducting and insulation layers. In addition, the through hole via (1), blind via (2) and buried via (3) are depicted.

The surface of the board is usually covered by a solder mask, while the needed contacts for surface mounted components remain open. The solder mask protects the PCB against corrosion and mechanical damage (Coombs, 2001).

The PCB manufacturing procedure can be seen as a complicated technology. A good overview is presented in Tao, 2018.

2.2 Epoxy Resin

Epoxy or modified epoxy resins are in widespread use within the PCB industry (Jawitz, and Jawitz, 2007). They are classified as thermosetting plastics. During the curing reaction, epoxy resins do not release any volatile components and the occurring chemical shrinkage is low compared to other thermosets. They have excellent mechanical properties in the fully cured stage. In addition, a low tendency to stress cracking, high chemical resistance, high strength during quick static and dynamic loading conditions, good electrical and di-electrical properties and low flammability can be highlighted, compared to other thermosetting plastics like unsaturated polyester resin. From a chemical point of view, epoxy resins are chemical connections formed by multiple highly reactive epoxide and hydroxyl end groups. The two reactive end groups react in order to crosslink and form a chemical network. Figure 2-2 represents the chemical structure of bisphenol-A and epichlorhydrin, with highlighted reactive end groups (Dominighaus et al., 2008).

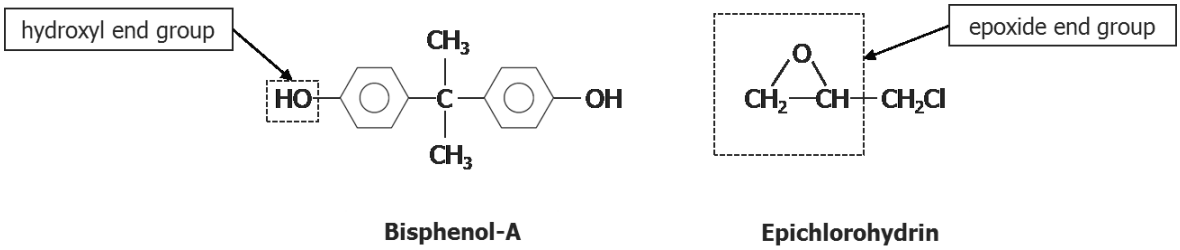

Figure 2-2: Chemical structure of bisphenol-A and epichlorhydrin, with highlighted epoxide and hydroxyl end groups.

Usually small filler particles are added in order to achieve, enhance or tailor a certain required application profile of the epoxy. Those fillers are added to reduce the thermal expansion coefficient, to improve the reliability and machinability and/or to decrease the cost. There is a wide range of inorganic filler materials available; from kaolin clay powder to tiny hollow glass particles and other inorganic particles (Coomb, 2001).

2.3 Glass Fibre Reinforced Prepregs

Preimpregnated glass fibres (Prepres or PP) are two-phase composites made of glass fibres and partially cured resins. A woven fibre reinforcement and an epoxy resin are usually used in PPs for PCB manufacturing. The PP manufacturing is a quite challenging procedure. During the PP production, the woven fibreglass is impregnated in the liquid resin system and afterwards a certain heat level is applied to create the partially cured B-staged PP (Jawitz and Jawitz, 2007).

There is a wide range of glass types available. For general PCB applications, usually E-glass is used because of its good electrical and mechanical properties and additional good water, acid and heat resistance. Furthermore, a low cost profile makes E-glass attractive. Only the plain weave fabric has gained importance in the PCB industry. Figure 2-3 shows three different woven fibre fabrics with a plain weave architecture. A fabric is differentiated into two yarns. The warp yarns are placed in the machining direction and the weft or fill yarns are positioned perpendicular to the warp yarns. A plain weave architecture is usually so built-up that one warp yarn passes over and under a weft yarn in an alternating pattern. The individual yarn bundles generally differ in the filament diameter and the number of filaments in warp and weft direction. The final PP thickness is defined depending on the resin content and fabric style (Coobs, 2001, Jawitz and Jawitz, 2007).

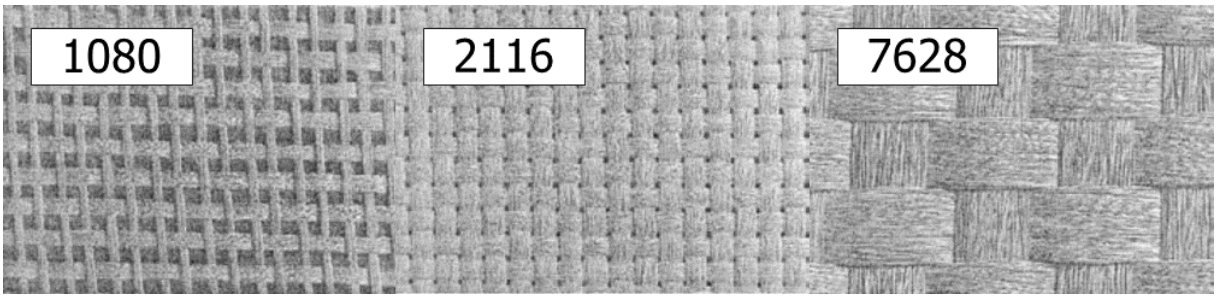

Figure 2-3: Three different woven fibre plain weave fabrics with specification number marking (Coombs, 2001).

2.4 Orthotropic Material Properties

The stress and strain relationship according to Hooke's law for a linear elastic three-dimensional anisotropic body in a 1-2-3 orthogonal Cartesian coordinate system exhibits the following form:

$$\underline{\sigma}=\underline{\underline{C}}\,\underline{\varepsilon} \tag{1.1}$$

where $\underline{\underline{C}}$ is the [6X6] stiffness tensor including the 36 elastic constants. The stress vector $\underline{\sigma}$ includes the normal (σ) and shear (τ) stress components; the strain vector $\underline{\varepsilon}$ includes the normal (ε) and shear strain (γ) components. As shown in Kaw, 2006, the stiffness tensor is usually a symmetric tensor. Thus, only 21 individual stiffness constants are placed in $\underline{\underline{C}}$. By rearranging equation (1.1), the stiffness tensor has to be inverted. The new equation includes now the inverted stiffness tensor (compliance tensor $\underline{\underline{S}}$), which is also a symmetric tensor with 21 entries, as shown in equation (1.2).

$$\begin{bmatrix}\varepsilon_{11}\\ \varepsilon_{22}\\ \varepsilon_{33}\\ \gamma_{23}\\ \gamma_{31}\\ \gamma_{12}\end{bmatrix}=\begin{bmatrix}S_{11} & S_{12} & S_{13} & S_{14} & S_{15} & S_{16}\\ & S_{22} & S_{23} & S_{24} & S_{25} & S_{26}\\ & & S_{33} & S_{34} & S_{35} & S_{36}\\ & & & S_{44} & S_{45} & S_{46}\\ & & & & S_{55} & S_{56}\\ & & & & & S_{56}\end{bmatrix}\begin{bmatrix}\sigma_{11}\\ \sigma_{22}\\ \sigma_{33}\\ \tau_{23}\\ \tau_{31}\\ \tau_{12}\end{bmatrix} \tag{1.2}$$

A subcategory of the anisotropic material definition is the orthotropic definition. Three orthogonal planes of symmetry with corresponding different property definitions along the preferred directions are required to define a material as orthotropic. According, Kaw, 2006, materials such as single laminate layers with a rectangular fibre architecture, wooden bars and rolled steels can be considered as orthotropic. The coupling between shear strains (γ), normal stresses (σ), as well normal strains (ε), and shear stresses (τ) are non-existent. Considering these assumptions has lead to the symmetric orthotropic compliance tensor, which includes 9 independent orthotropic engineering constants, as shown in equation (1.3). This tensor includes three moduli (E1, E2 and E3), three Poisson's ratios (v12, v13 and v23) and three shear moduli (G12, G13 and G23). The relationship between the individual moduli and Poisson's ratios due to the symmetry is given in equation (1.4) (Kaw, 2006, Tuttle, 2004).

When representing a laminate material with an orthotropic material definition, usually the engineering constants are temperature dependent. This effect is caused by the polymeric matrix. Figure 2-4 represents a schematic drawing of the temperature dependent engineering constants of a woven glass fibre reinforced laminate (AT&S 2017).

$$\underline{\underline{S}}=\begin{bmatrix}\frac{1}{E_1} & -\frac{v_{21}}{E_2} & -\frac{v_{31}}{E_3} & 0 & 0 & 0\\ -\frac{v_{12}}{E_1} & \frac{1}{E_2} & -\frac{v_{32}}{E_3} & 0 & 0 & 0\\ -\frac{v_{13}}{E_1} & -\frac{v_{23}}{E_2} & \frac{1}{E_3} & 0 & 0 & 0\\ 0 & 0 & 0 & \frac{1}{G_{23}} & 0 & 0\\ 0 & 0 & 0 & 0 & \frac{1}{G_{12}} & 0\\ 0 & 0 & 0 & 0 & 0 & \frac{1}{G_{13}}\end{bmatrix} \tag{1.3}$$

$$\frac{v_{ij}}{E_i}=\frac{v_{ji}}{E_j} \text{ for } i\neq j \text{ and } i,j=1,2,3 \tag{1.4}$$

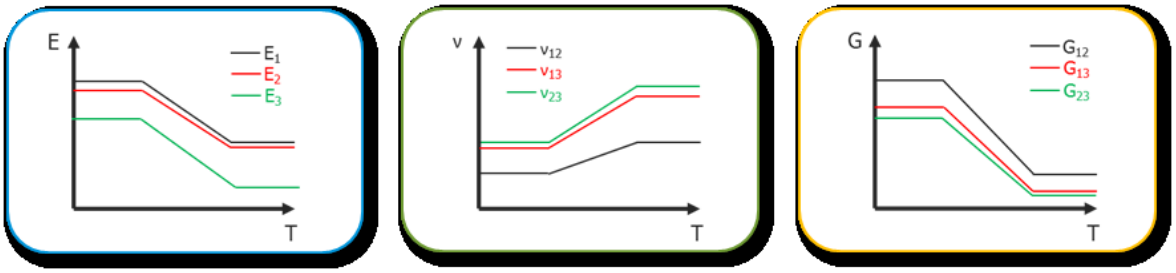

Figure 2-4: Schematic representation of the temperature dependent orthotropic engineering constants of a woven glass fibre reinforced laminate (AT&S, 2017).

2.5 Basics of Measurement Technology

2.5.1 Hydrostatic Weighing

The hydrostatic weighing technique is the most commonly used technique for the evaluation of the density. Archimedes' principle for determining the density of a solid body is the fundament of the technique. For the density evaluation of a specimen ($\rho_{Specimen}$), the specimen has to be weighted in the dry state (m_{Air}) and afterwards in the measurement fluid (m_{Fluid}). When the body enters the measurement liquid, the body experiences a buoyancy. The resulting buoyant force is equal to the weight of fluid displaced by the specimen. The density of the fluid (ρ_{Fluid}) at the measurement temperature must be known. Afterwards, the density of the specimen can be calculated by equation (1.5) (Frick and Stern, 2011).

$$\rho_{Specimen} = \frac{m_{Air}}{m_{Air} - m_{Fluid}} \rho_{Fluid} \tag{1.5}$$

2.5.2 Thermogravimetry

The mass or the mass change of a specimen as a function of temperature and time can be measured by thermogravimetry (TG). Evaporation, decompensation, chemical reaction and magnetic or electronic transformation can cause the mass change of a material. The TG is standardized in DIN EN ISO 11358, 1997 and DIN 51 006, 1990. To avoid the possibility of confusion of TG and the glass transition temperature (T_g), it is common to use the abbreviation TGA, for thermogravimetric analysis. The selection of the purge gas and the condition of the sample chamber are highly relevant for the measurement outcome. Inert or oxidation purge gasses, for example, nitrogen, helium, argon, oxygen or air are used. In individual cases, the measurement is executed in a vacuum. The heat transfer of the sample depends on the purge gas flow velocity. Figure 2-5 shows a schematic representation of a

horizontal thermobalance. Also vertically constructed thermobalance devices are available. The mass change during the measurement is controlled to the zero position by an electromagnetic or an electromagnetic compensation balance via a light barrier controlled regulatory cycle. The mass change as a function of the time and temperature is determined by the compensation signal (Ehrenstein et al., 2003).

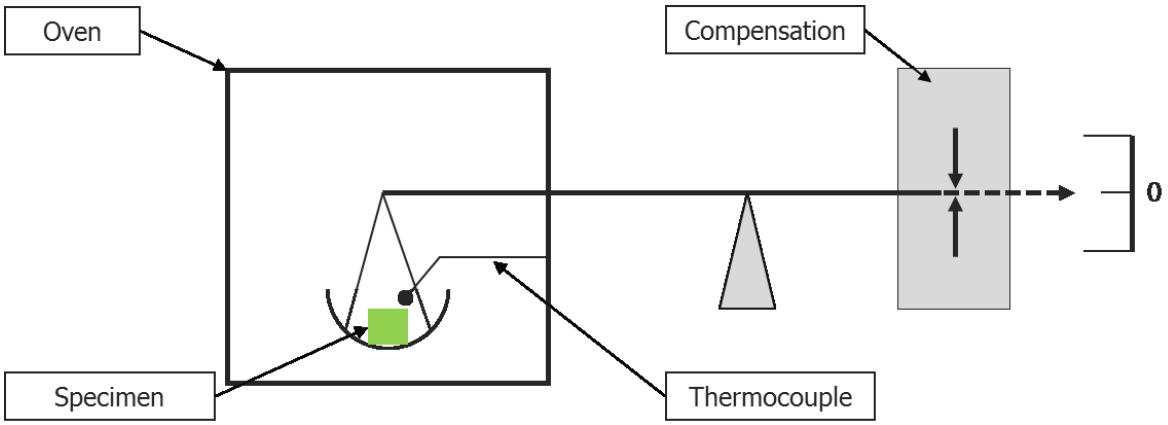

Figure 2-5: Schematic representation of a thermocouple. Adapted from Ehrenstein et al., 2003.

2.5.3 Uniaxial Tensile Test

Figure 2-6a illustrates a three-dimensional body with tensile specimens taken from different positions. When loading the specimens in the depicted directions, the corresponding property response can be anisotropic. More precisely, the moduli of the three specimens differ in every direction (E1≠E2≠E3). On the other hand the response can be isotropic; the corresponding moduli are the same when loading the specimens (E1=E2=E3). By establishing the assumption that specimen 1 is loaded in the direction 1 by executing a uniaxial tensile test, a normal stress σ_{11} is introduced and reaches a maximum level during the test. For an anisotropic material, the stress will introduce all six-strain components shown in equation (1.2) (ε_{11}, ε_{22}, ε_{33}, γ_{23}, γ_{31} and γ_{12}). A schematic illustration of the introduced strains is shown in figure 2-6b. Now only considering the properties related to normal strains and stresses leads to the definition of the Young's modulus E11. The Young's modulus E11 is basically the slope of the normal stress σ_{11} and strain components ε_{11} and is defined in equation (1.6). The relationship between the transverse strains (ε_{22} and ε_{33}) and normal strains (ε_{11}) is described by the Poisson's ratio. The Poisson's ratio is defined as the quotient of the negative transverse normal strain and axial normal strain, shown in equation (1.7). As represented in equation (1.7), the first letter in the Poisson's ratio

describes the direction of the applied stress and the second letter the direction of the transverse strain component (Tuttle, 2004).

$$E11=\frac{\sigma_{11}}{\varepsilon_{11}} \tag{1.6}$$

$$v_{12}=-\frac{\varepsilon_{22}}{\varepsilon_{11}} \text{ and } v_{13}=-\frac{\varepsilon_{33}}{\varepsilon_{11}} \tag{1.7}$$

Grellman and Seidler, 2007 presented more detailed information regarding the theoretical background, specimen preparation, test parameters and evaluation of the uniaxial tensile test.

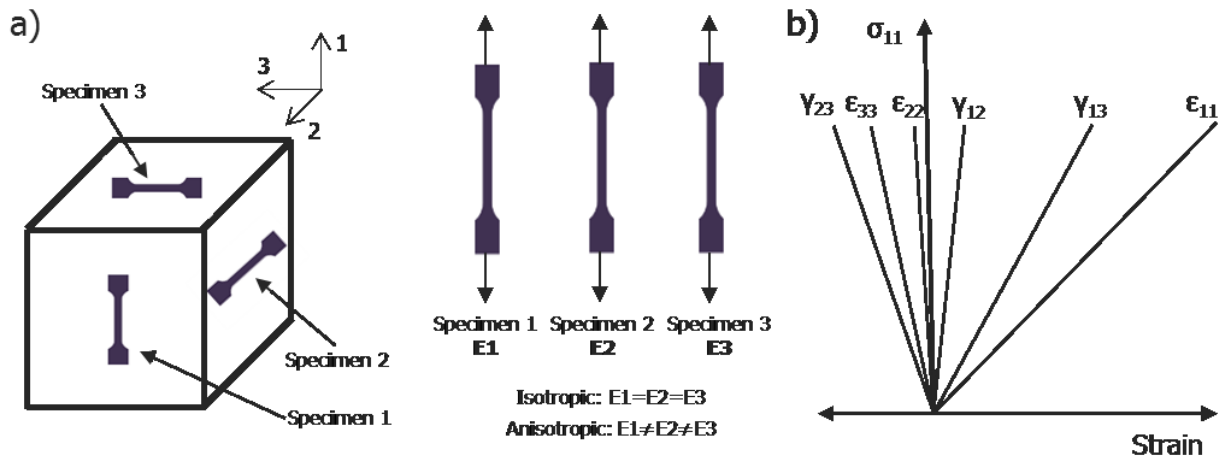

Figure 2-6: Three different tensile specimens machined in different directions from the same overall "block". b) Anisotropic strain components when performing a tensile test of specimen 1. Adapted by Tuttle, 2004.

2.5.4 Digital Image Correlation

Digital image correlation (DIC) is an optical measurement method based on tracking the displacement and deformation in 2D or 3D images of a sample. The principle of the DIC technique was developed by Sutton M, 1983. According to his theory, the image of a body can be represented by a discrete function. Therefore, a correlation function has to be fitted for a group of pixels, called pattern. This discrete function named f(x,y) represents the body before the deformation and will be transformed into another discrete function known as f*(x*,y*) after deformation. The theoretical relation between those two discrete functions can be written as:

$$f^{*}(x^{*},y^{*})-f(x+u(x,y)+v(x,y))=0 \tag{1.8}$$

where u(x,y) and v(x,y) represent the displacement fields in x and y direction for a pattern. Figure 2-7 shows the basic idea of the correlation calculation. Execution and evaluation of the strain measurement with DIC is described in the literature by Jerabek, 2010.

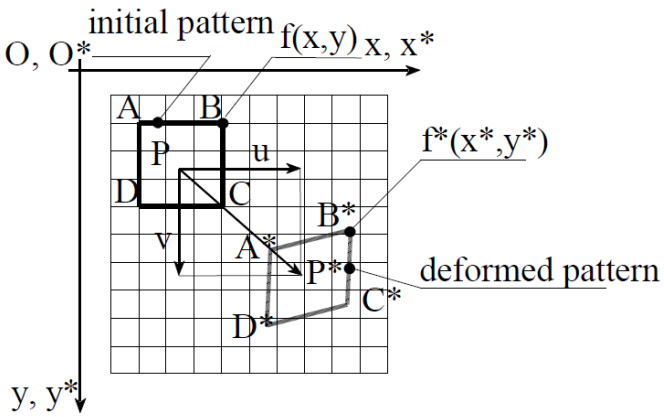

Figure 2-7: Basic idea of the correlation calculation (Mguil-Touchal et al., 1997).

2.5.5 Dynamic Mechanical Analyses

In a dynamic mechanical analyses (DMA) specimens are subjected to oscillating loads. The various methods of DMA are standardized in DIN EN ISO 6721-1, 1996. In case of linear-viscoelastic material behaviour, steady-state stress and strain signals exhibit the same frequency ($\omega=2\pi f$), but varying phase angles (Grellman and Seidler, 2007). The measured values in a DMA experiment are the strain and stress amplitudes and the corresponding time shift (δ/ω) between those amplitudes (Ehrenstein et al., 2003). Figure 2-8a shows the applied oscillating strain signal and the resulting stress signal.

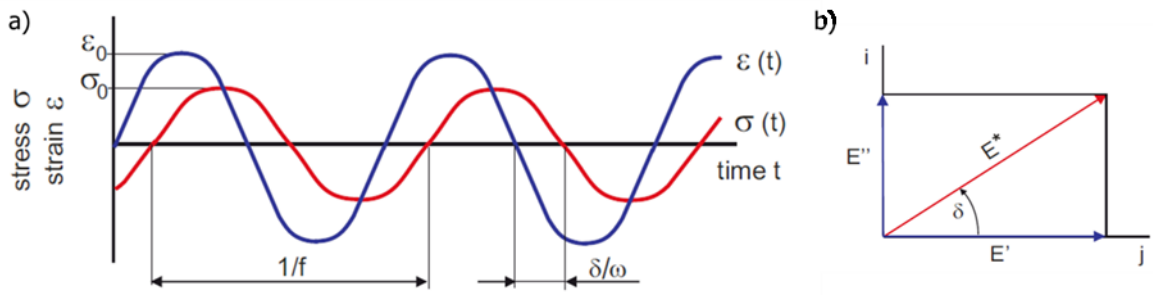

Figure 2-8: a) The applied oscillating stress and the resulting strain signal. b) Diagram of modulus E* in the complex plane (Grellman and Seidler, 2007).

The complex modulus E^* describes the stress-strain relationship as a result of the phase shift δ between stress and strain:

$$\left|E^*\right| = \frac{\sigma_0}{\epsilon_0} \tag{1.9}$$

$$E^{*}=E'+iE'' \tag{1.10}$$

where E' is the storage modulus, E'' the loss modulus, σ_0 the stress amplitude and ϵ_0 the strain amplitude. With the vectorial trigometric relations shown in figure 2-8b, E' and E'' can be distinguished as:

$$E'(\omega)=\left|E^{*}\right|\cos(\delta)=\frac{\sigma_0}{\epsilon_0}\cos(\delta) \tag{1.11}$$

$$E''(\omega)=\left|E^{*}\right|\sin(\delta)=\frac{\sigma_0}{\epsilon_0}\sin(\delta) \tag{1.12}$$

Consequentially, the loss factor tan(δ) can be written as:

$$\tan(\delta)=\frac{E''(\omega)}{E'(\omega)} \tag{1.13}$$

The storage modulus E' represents the stiffness of a viscoelastic material and is proportional to the stored elastic work during a load period. It corresponds approximately to a monotonic tensile load at low loading conditions and reversible deformation. The loss modulus (E'') is proportional to the dissipated work in the material during a one load period. It characterises, for example, the dissipated heat energy and is a measure for the non-recoverable, transformed oscillation energy, per oscillation. Thus, the real part (E') of the complex modulus describes the elastic properties of a material and the imaginary (E'') part the viscous characteristics. Their units are specified in [N/mm^2] or [MPa]. The phase angle (δ) marks the phase shift between dynamic stress and dynamic strain of a viscoelastic material during sinusoidal oscillations and with a unit of [Rad]. The loss factor tan(δ) is a measure for the energy loss per oscillation of the recoverable energy. It characterises the mechanical damping or the inner friction of a viscoelastic system. Highly non-elastic deformation components in a material are described by high tan(δ) values. The loss factor is dimensionless [-] (Ehrenstein et al., 2003). During the heating phase of a DMA experiment, a polymeric material usually passes through transition temperatures. During these transitions, the above-mentioned viscoelastic functions exhibit major changes attributed to increasing free volume at elevated temperatures. A detailed description about transitions from a polymer physics point of view can be found in Menard, 1999.

An essential component of the test, in terms of the quality and accuracy of a DMA experiment, is the applied deformation. The deformation region where a material shows linear-viscoelastic behaviour has to be experimentally obtained. Therefore the deformation

dependence of the modulus at a fixed frequency should be determined. In the linear viscoelastic region, the applied displacement should not influence E' and E''. Plotting the storage modulus and/or loss modulus vs. the displacement, or force amplitude, at a defined frequency and temperature, enables the evaluation of the linear-viscoelastic limits. As long as the two moduli are constant, the displacement and force amplitudes are in the linear-viscoelastic region. When the storage and/or loss modulus drops, plastic deformation and/or damage processes occur. Linear-viscoelastic approaches are not valid any more (Ehrenstein et al., 2003). This procedure is known as force scan. Figure 2-9 represents the evaluation of the linear-viscoelastic region. By plotting the relationship of the force and displacement amplitudes, the linear slope in the beginning also indicates the linear-viscoelastic region.

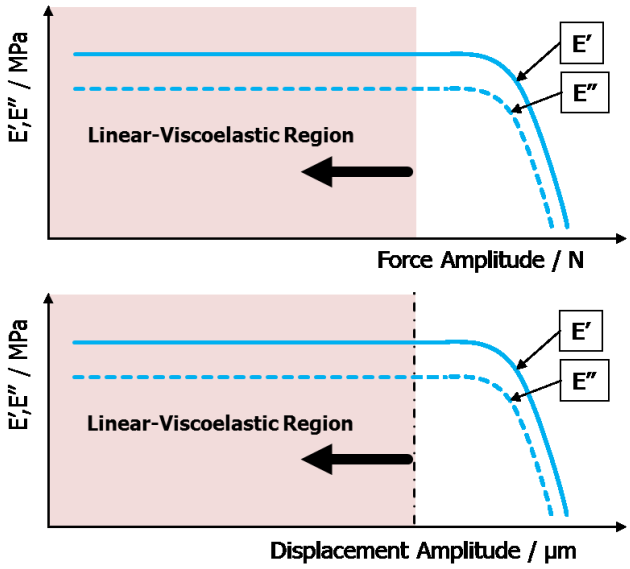

Figure 2-9: Evaluation of the linear-viscoelastic region. Storage modulus and loss modulus as a function of the force and displacement amplitude.

2.6 Basics of Numerical Methods

2.6.1 Finite Element Method

In general terms the finite element method (FEM) represents a combination of procedures, algorithms and methods from different disciplines to enable a mathematical prediction of a field problem. These disciplines are, for example, mathematics, numerics, continuum mechanics or fluid mechanics, materials science and programming technologies. To find a solution for a problem, certain equations have to be established to connect known and unknown parameters. Therefore, FEM cuts a structure into pieces, the so-called "elements". A small piece of a structure is called a "finite element". Afterwards FEM reconnects the elements at the "nodes". Connecting nodes share the same degree of freedom (DOF) at

adjacent elements. The result of this procedure is a set of simultaneous algebraic equations. The number of degrees-of-freedom is finite. Lots of engineering phenomena can be expressed by differential equations and boundary conditions. The most common problem is that all equations are known, but it is not possible to solve them. The FEM approximates the differential equations and boundary conditions into a set of simultaneous algebraic equations, at the nodes. This set of simultaneous algebraic equations is defined as:

$$[K]\{u\}=\{F\} \tag{1.14}$$

where [K] represents a property (e.g. stiffness, conductivity viscosity or dielectric permittivity), {u} represents the behaviour (e.g. displacement, temperature, velocity or electric potential) and {F} stands for the action (e.g. force, heat force, body force, charge). The unknown behaviour can be calculated with the equation (1.15).

$$\{u\}=[K]^{-1}\{F\} \tag{1.15}$$

The interpolation of a field quantity is executed polynomially over an element. As a result of this procedure, the entire structure is interpolated in a piecewise fashion (Department of Aeronautical and Astronautical Engineering, 2004, Strommel et al., 2011).

According Strommel et al., 2011, the finite element method executed by a commercial software, can be differentiated into the subsequent listed steps:

- Pre-Processing: A model is generated and implemented into the FE-environment
- Solving: The CPU conducts the numerical analysis (processing).
- Post-Processing: The results are reviewed.

The pre- and post-processing steps are usually handled by the user. Figure 2-10 represents a brief overview of the FEM.

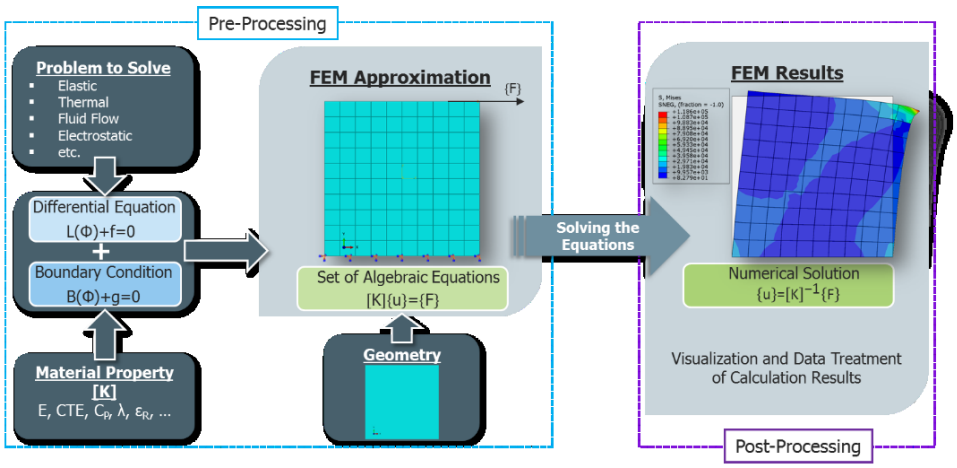

Figure 2-10: Overview of the FEM.

2.6.2 Periodically Repeating Unit Cell

In order to perform a micromechanical analysis, it is common to describe the micro geometry of a system by a periodically repeating unit cell (RUC). Figure 2-11 presents eight different schematic minimum-size cells. All eight cells describe the overall two-dimensional volume in the same periodic manner. When applying periodic boundary conditions to the cells, the property response of every individual RUC should be the same (Böhm, 2017). The solution field φ of a periodic field response can be expressed as follows:

$$\varphi(x_j+p_j^{\alpha})=\varphi(x_j)+\langle\frac{\partial\varphi}{\partial x_j}\rangle p_j^{\alpha} \tag{1.16}$$

where x_j is the coordinate, $\langle\frac{\partial\varphi}{\partial x_j}\rangle$ the far-field of the solution field and p_j^{α} is the vector of periodicity (depicted in figure 2-11), respectively. A solution field φ can be a displacement or temperature with a corresponding solution field $\langle\frac{\partial\varphi}{\partial x_j}\rangle$ as displacement or temperature gradient (Dassault Systèmes, 2017). A more detailed and good overview about the basics of micromechanical approaches is presented in Böhm, 2017.

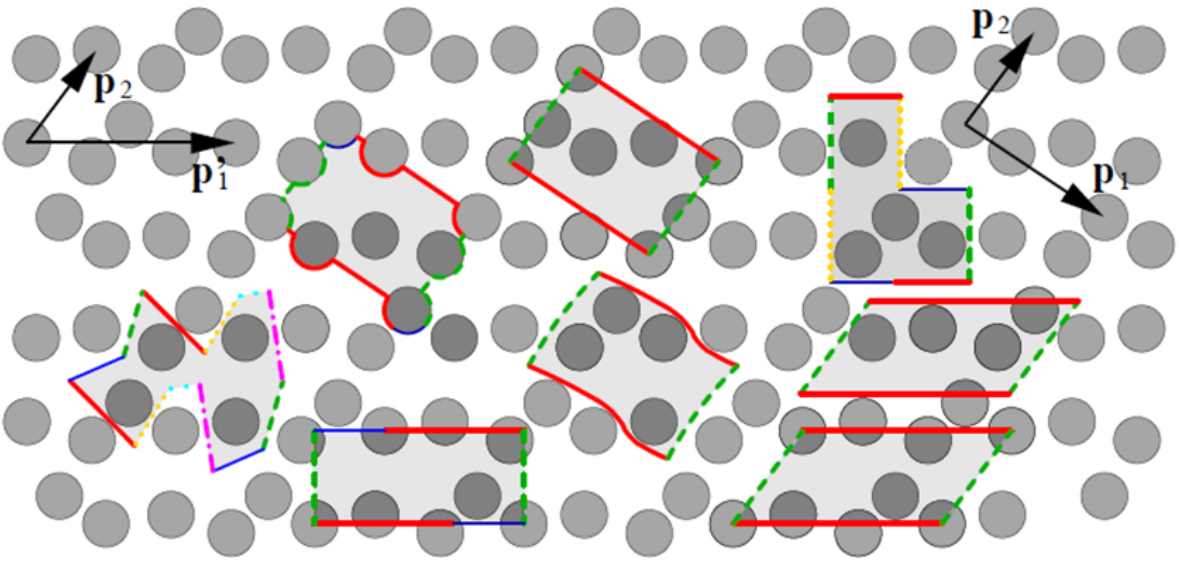

Figure 2-11: Overall two-dimensional volume with eight different minimum size cells presenting the overall volume in the same way (Böhm, 2017).

3 MATERIALS AND SPECIMENS

One purpose of this thesis was the preparation of specimens for tensile tests and DMA measurements by an automated routing procedure of resin-only and laminate materials used in PCBs. The material family was defined beforehand by AT&S. The established specimen preparation methodology should be investigated in the experimental part. Therefore, monotonic tensile tests and DMA measurements in different laminate specimen directions should be executed in a systematic way. However, the corresponding different Young's and storage modulus outcome should also be examined. In order to investigate the panel position influence of the modulus due to the PCB production press, one prepreg material was laminated in the production at the AT&S Shanghai (SHA) plant. In order to achieve these goals, with respect to the specimen preparation, four steps were designed and executed.

First a prepreg and core were selected from the same material family. This means that the chosen prepreg and core material have the same resin system. Therefore, two core materials (CCL) and one prepreg material were selected, determined by the availability at the AT&S SHA plant. The PCB material manufacturer delivered the corresponding epoxy matrix in the form of the requested resin board without glass fabric reinforcement. Second, a methodology for an automated laminate specimen preparation was established and executed. For this purpose, the laminate specimens were prepared in the production process in SHA, according to the defined methodology. This approach provided a way to laminate the selected prepreg directly in the PCB production. Third, the resin specimen preparation was conducted in AT&S Hinterberg (HTB). Finally, the specimens were tested in the experimental part of the present study.

3.1 Resin Specimen Preparation

The resin-only board (100 x 100 x 1 mm) was delivered by a third party manufacturer in Japan and is represented in figure 3-1a. In total, seven of these boards were delivered to AT&S HTB. With the intention of preparing tensile test specimens from the semi-finished resin board, a routing program was defined at AT&S HTB. The specimen geometry was defined according DIN EN ISO 572-1, 2010; the small tensile specimen ISO 572 Type 1BA was selected. Ideally, tensile specimens should fracture in the middle of the specimen in order to investigate the fracture properties accurately (Grellmann and Seidler, 2007). Therefore, the position for the insertion holes of the routing tool should not be within the

area of the specimen shoulder, to avoid the development of a predetermined breaking point. Six tensile specimens were routed out per resin board. Figure 3-1b shows the basic idea of the developed routing program.

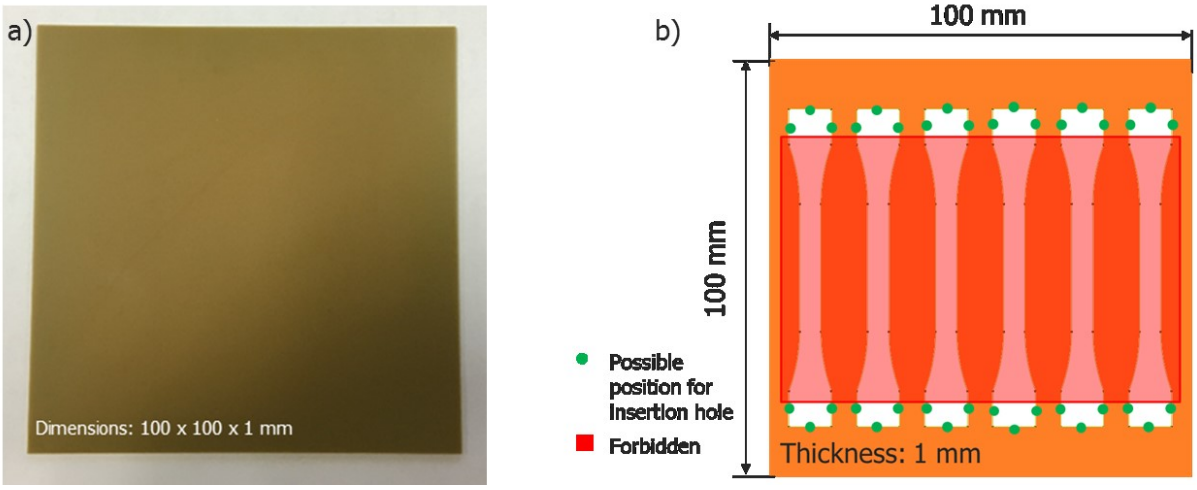

Figure 3-1: a) Epoxy resin board. b) Basic idea of the routing program for the preparation of the tensile specimens.

The specimens were prepared with a routing machine for PCB manufacturing (Schmoll Maschinen GmbH, Rödermark/Ober-Roden, Deutschland). The routing parameters (e.g. routing tool, diameter of the tool, velocity) were selected based on the experience of the Process Quality Engineer in the production. In addition, the DMA stripes were cut out manually with a diamond saw at the Physics Lab in AT&S HTB. They were prepared with a 3 mm width from the remaining resin boards.

The manufacturer did not provide additional information about the exact composition and the curing degree of the delivered resin boards. Hence, preliminary investigations by DMA were executed (appendix figure A-1). Ehrenstein et al., 2003, presented a good overview of the influence and evaluation of the curing degree to the viscoelastic functions. The results indicated that the delivered resin boards were not fully cured. Golestanian and Sherif, 1996, reported a linear correlation between the curing degree and the modulus of a thermosetting system. However, detailed investigations of the effects from the curing degree to the modulus were not within the scope of the thesis. According to the datasheet, the T_g's of the laminates were somewhere between 160°C and 200°C, depending on the applied measurement technology. In order to ensure a fully cross-linked and dry state of the thermosetting system in the experimental studies, the specimens were conditioned above the T_g at 200°C for two hours before executing a measurement. These conditioning parameters additionally ensure full post-curing of the resin, while the storage time is not

sufficient to introduce significant aging effects. Figure 3-2 shows the prepared specimens after conditioning.

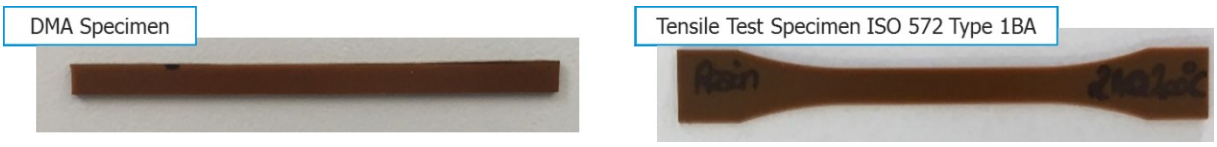

Figure 3-2: Resin specimens after conditioning.

3.2 Laminate Specimen Preparation

In the following, the warp direction will be referred as direction 1, the fill direction as direction 2. The direction Z is perpendicular to the laminate plane and is denoted as direction 3. The 45° direction is located in a 45° angle between the 1 and 2 directions. To prepare the laminate specimens, the steps listed below were executed:

1) Two CCLs with a copper thickness of 12 µm were selected. They can be differentiated in terms of the fabric architecture, laminate thickness and the resin content. Both CCLs were composed of one laminate layer. Afterwards, the prepreg was selected and laminated with a 12 µm copper foil at AT&S SHA, using the proposed press parameters from the material manufacturer. Therefore, two equal prepreg layers were pressed in order to achieve an appropriate final specimen thickness. After the pressing procedure, this material can be seen as equivalent to a panel size CCL. The three manufacturing panels were defined as so-called "test vehicles". Figure 3-3 presents the build-ups of these test vehicles. Table 3-1 summarizes the most important information needed in the PCB production at AT&S SHA. Usually only copper layers are counted in terms of the PCB production. The defined test vehicles correspond to a base manufacturing panel of a two layer PCB.

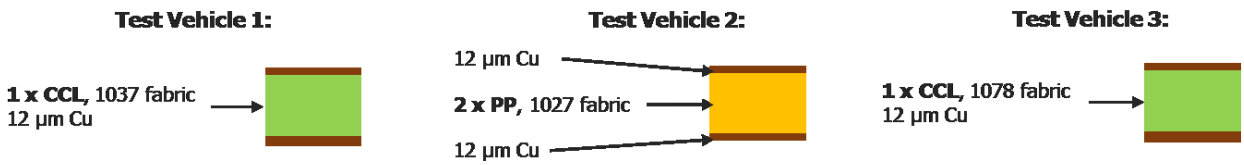

Figure 3-3: Graphical illustration of the three different test vehicles.

Table 3-1: Summarized test vehicle information, needed in the PCB production.

Layer	Test Vehicle 1	Test Vehicle 2	Test Vehicle 3
1	12 µm	Cu, 12 µm	12 µm
1-2	#1037, 50 µm	#1027, 40 µm	#1078, 60 µm
		#1027, 40 µm	
2	12 µm	Cu, 12 µm	12 µm

2) The tensile test and DMA specimens in the 1, 2 and 45° direction were utilized as a PCB card layout. Likewise, the same tensile test specimen geometry was chosen for the resin specimen (ISO 572 Type 1BA). The DMA tensile stripes were placed directly beside the tensile test specimens, in an attempt to create comparable moduli in the experimental part (figure 3-4 and figure 3-5). Predetermined breaking points were added, as can be seen in figure 3-4. In order to obtain a reasonable material utilization, rectangular specimens for other tests like thermogravimetry, hydrostatic weighing, differential scanning calorimetry and laserflash measurements were placed accordingly. The card layout is shown in figure 3-5.

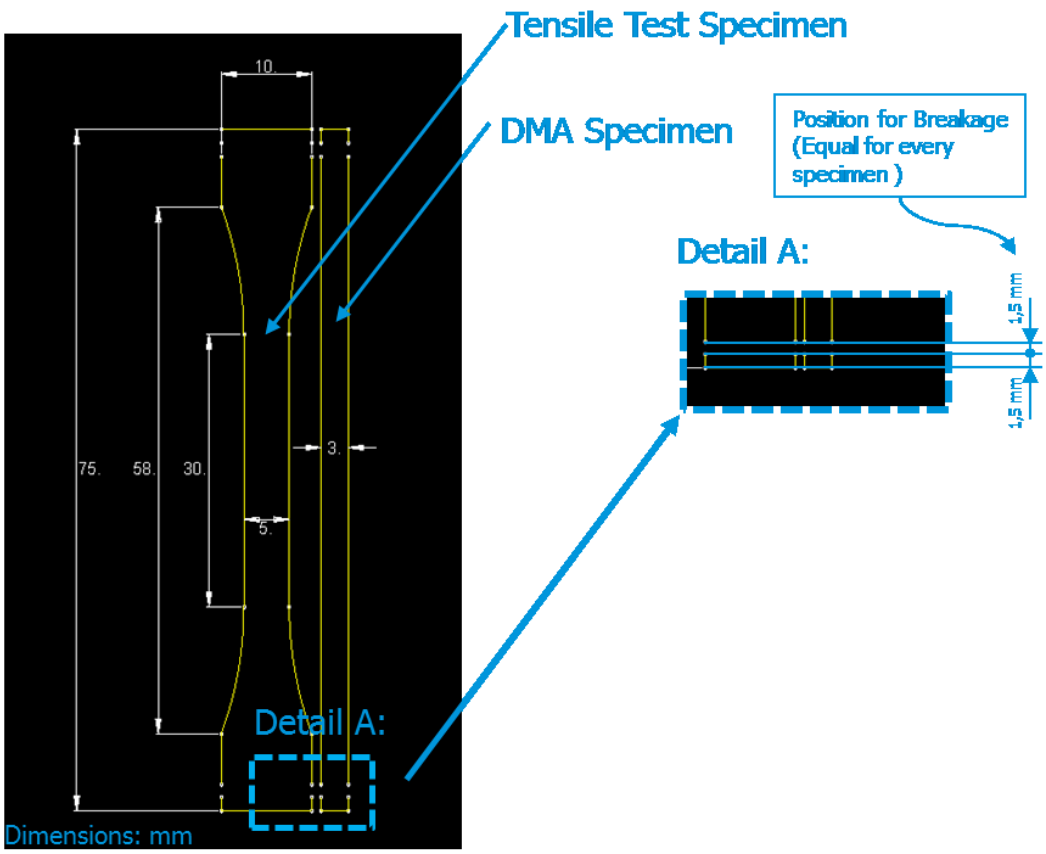

Figure 3-4: Tensile and DMA routing specimen geometry with added positions for predetermined breaking points.

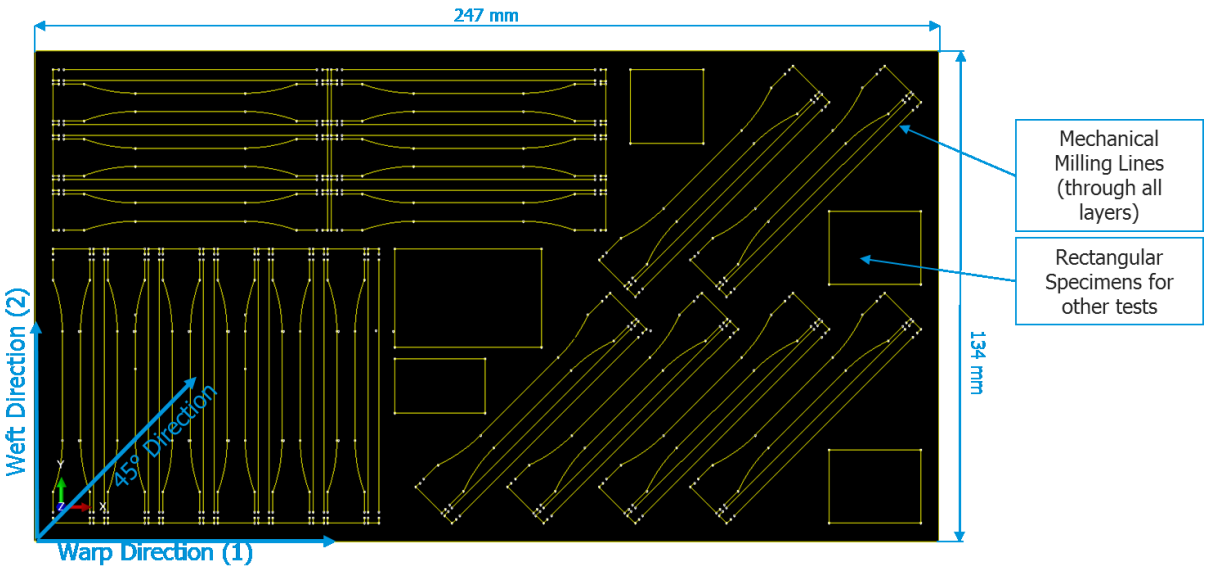

Figure 3-5: Card layout with different specimens.

3) In the next step, the panel layout was defined by taking the individual panel size of the three test vehicles into account. For every panel, six card layouts were placed at different panel positions. This approach enabled the investigation of the modulus at different positions, with respect to the in-house pressed test vehicle 2. Figure 3-6 represents the panel layout with additional geometric information of the card layout placement.

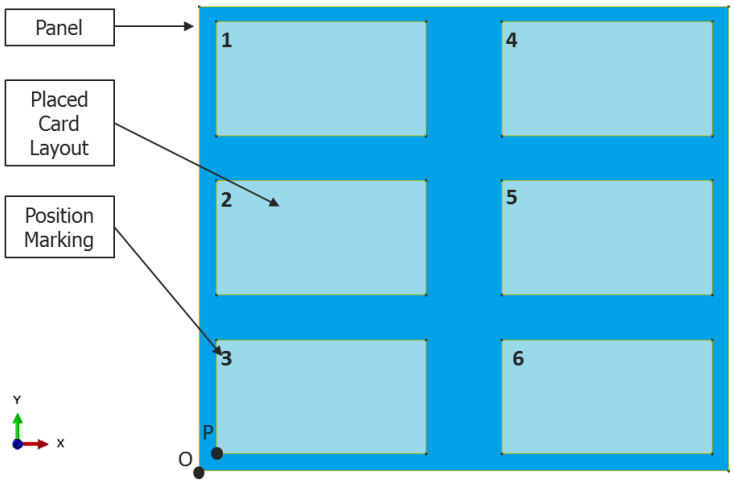

	[mm]	
O	X:0 Y0	
P	X:20 Y:20	
L_Array-X	247	
L_Array-Y	134	
Step in X	336	Test Vehicle 2 (623 x 546)
Step in Y	187	
Step in X	331	Test Vehicle 1 & 3 (618 x 541)
Step in Y	182	

Figure 3-6: Designed panel layout with additional card layout placement information.

4) After designing the card and panel layout, the corresponding PCB production-routing program was developed by a Product Engineer at AT&S SHA. Every card layout was marked with the positions defined in figure 3-6. The depanelization process is according to Coombs, 2001, the executed numerical control (NC) routing of the manufacturing panel in order to get the finished PCB product. This procedure was

executed at AT&S SHA. Afterwards, the individual cards were delivered to AT&S HTB. Unfortunately, the card layouts at position 1 and 4 of test vehicle 2 were not delivered to AT&S HTB for unknown reasons. The individual specimens were carefully extracted from the cards. Afterwards, the copper on the top and bottom surfaces was etched of by using dissolved copper (II) chloride ($CuCl_2$), in hydrogen chloride (HCL). In order to not mix up different specimen directions during the etching procedure, the specimens were appropriately marked beforehand. Figure 3-7 shows the delivered cards, the used etching solution and the specimens after the etching procedure.

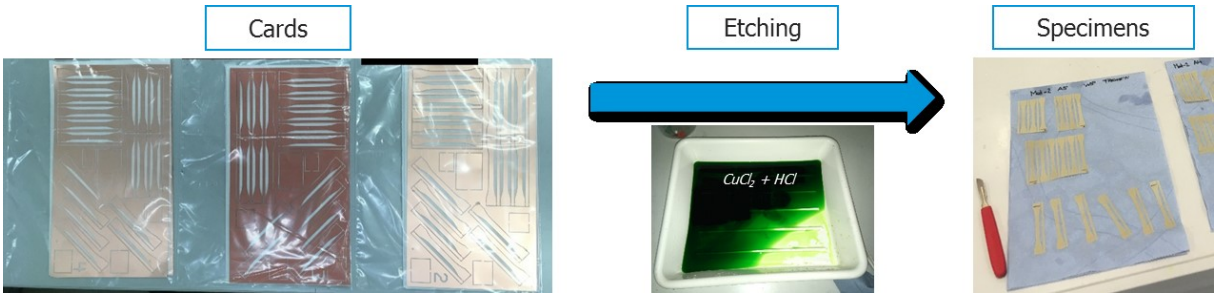

Figure 3-7: Final routed cards, the used etching solution and the specimens after performing the etching procedure.

5) The final specimens were conditioned in the temperature chamber before the measurements were performed. Laminate 1 (test vehicle 1) and 3 (test vehicle 3) were conditioned for one hour at 105°C, to ensure no moisture content inside the specimens (IPC-TM-650 2.4.24C, 1994). No additional precondition was needed for the two laminates, because it could be assumed that they had already been fully cured by the material manufacturer (core materials). On the other hand, the intention was to mechanically characterise both core materials in the initial state. Laminate 2 was the in-process pressed test vehicle 2. In order to exclude effects on the modulus, due to perhaps not fully cured spots on the different panel positions, the specimens were post-cured in the temperature chamber for two hours at 200°C. Using this approach enabled the investigation of the modulus based on the fully cured resin distribution at different panel positions. After conditioning laminate 2, significant warpage of the specimens was observed, as shown in figure 3-8. In addition, the influence of fabric shifts caused by the resin flow during the lamination procedure could be observed by optically reviewing the specimens, as shown in figure 3-8. The summarized specimen information of the laminates is listed in table 3-2.

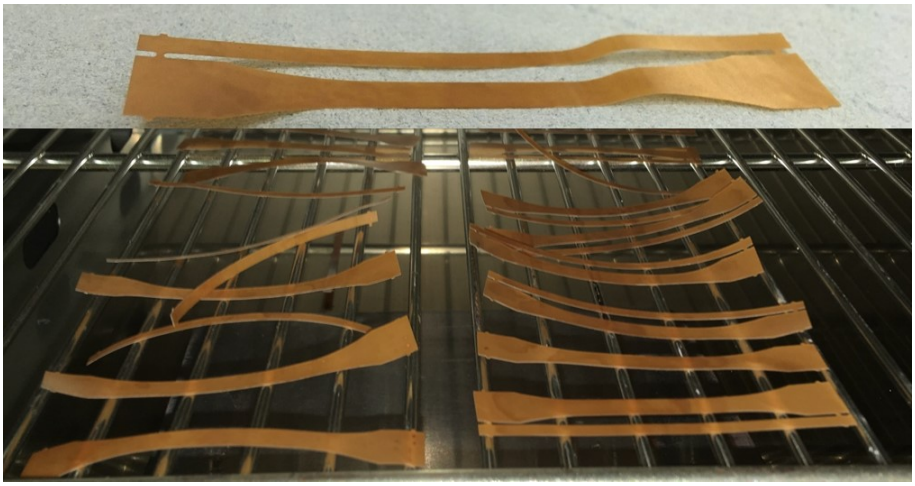

Figure 3-8: Specimen warpage of laminate 2 after the conditioning.

3.3 Summarized Specimen Information

Table 3-2 summarizes the most important specimen information. The investigated laminates differ in their woven fibre architecture and are specified in IPC-4412A, 2008. Laminates 2 (fabric type 1027) and 3 (fabric type 1078) have the same number of fibres in the 1 direction and 2 direction and are therefore so-called "balanced fabrics". On the other hand, laminate 1 with a 1037 woven fibre architecture is not balanced. Thus, laminate 1 should behave differently in the 1 and 2 direction from an experimental and numerical point of view. Because of the different fibre architectures, the corresponding resin contents are expected to differ among the three laminates. In general, the nature of the specimens (resin and laminates) can be seen as quite brittle and fragile.

Table 3-2: Summarized resin and laminate specimen information.

Material	[-]	**Resin**	**Laminate 1**	**Laminate 2**	**Laminate 3**
Fabric	[-]	-	1037	1027	1078
Warp and Fill Count	[cm]	-	27,6 x 28,7	29,5 x 29,5	21,3 x 21,3
Lamination Executer	[-]	-	Supplier	AT&S	Supplier
Manufacturing Panel	[-]	-	Test Vehicle 1	Test Vehicle 2	Test Vehicle 3
Pressed Layers	[-]	-	1	2	1
Conditioning	[-]	2 Hours at 200°C	1 Hour at 105°C	2 Hours at 200°C	1 Hour at 105°C
Thickness	[µm]	1000	50	80	60

4 EXPERIMENTAL

Another general aim of this study was the implementation of experimental methods, in order to investigate the engineering constants and the developed specimen preparation approach at the experimental level. Additionally, experimental data acquisition for the numerical part of the thesis was executed.

4.1 Hydrostatic Weighing

The density measurements were executed at the Polymer Competence Center Leoben GmbH (PCCL) with the analytical balance XS205DU (Mettler Toledo International Inc., Schwerzenbach, Switzerland) as shown in figure 4-1a. In order to calculate the resin volume content for a micromechanical approach, the density of the resin must be determined. The densities of the materials listed in table 3-2 were measured. For this four repetition measurements per material were conducted. In the first step, the specimen weight was measured in the dry state. In the second step, the specimens were weighed in a beaker filled with distilled water (figure 4-1b). Additionally, the water temperature was determined by the use of a thermometer (figure 4-1b) prior to the measurements. Those input parameters were provided to the software of the analytical balance. The densities of the tested materials were calculated then by the software of the analytical balance.

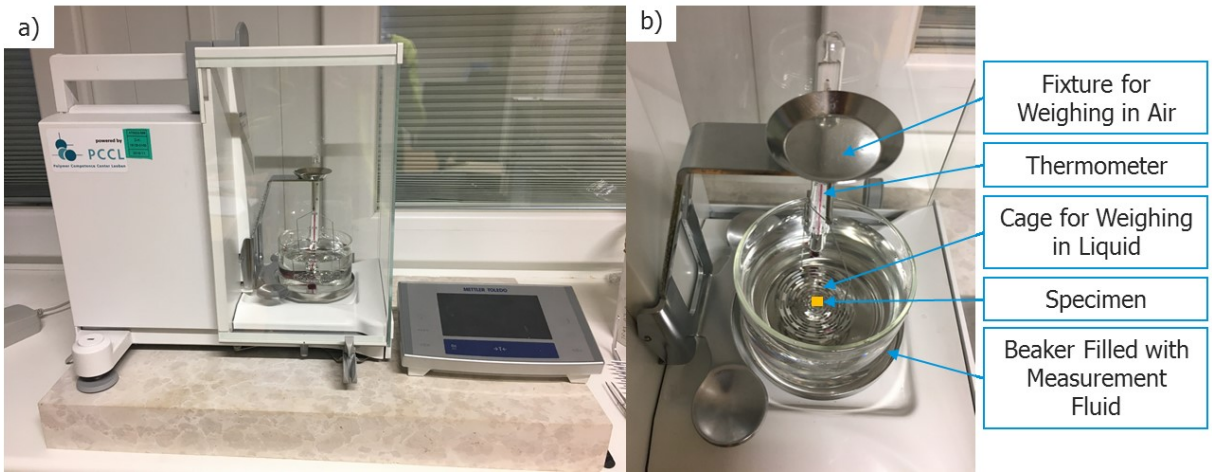

Figure 4-1: a) Analytical balance XS205DU (Mettler Toledo International Inc., Schwerzenbach, Switzerland). b) Measurement set-up with individual components.

4.2 Thermogravimetry

The inorganic filler contents of the materials listed in table 3-2 were analysed by a Netzsch TG 209 F1 Libra® (Netzsch-Gerätebau GmbH, Selb, Deutschland) at AT&S HTB as shown in

figure 4-2. For the numerical calculation, the laminate resin content input can be seen as a very important parameter for a successful micromechanical analysis (Frewein, 2017). Hence, the inorganic filler content of the resin system itself must be characterized to determine the laminate resin content correctly. In order to guarantee reproducibility, four repetition measurements per material were carried out.

To measure the mass loss as a function of the time and temperature, the initial specimen weight must be determined. At first, small quadratic laminate specimens with 3 x 3 mm were gently cut out from the additional added rectangular specimens (figure 3-5), using scissors. Because of the greater thickness of the resin board, small quadratic resin specimens were prepared carefully with a diamond saw. Afterwards the quadratic specimens were put into the Netzsch 85 µl alumina crucibles. As suggested by DIN EN ISO 11358, 19971, the specimen weight should be between 10 and 100 mg. In order to achieve a suitable specimen weight, the thin laminate specimens were stacked in the crucible. The stack height was 10 to 20 layers depending on the initial laminate thickness. Figure 4-3 shows the stacked quadratic specimens in the alumina crucible. All specimens were manually weighed before the measurements by using the analytical balance XS104 from Mettler Toledo International Inc.. Table 4-1 shows the measured specimen weights for the TGA.

In the next step, the filled crucibles were placed in the automatic sample changer tray. The weight data from table 4-1 were entered into the Netzsch Asc-Manager software. For the experiment, a first heating segment from 25°C to 800°C with a heating rate of 10 K/min was defined, as suggested by Ehrenstein et al., 2003. In addition, a second isothermal heating segment with 150 minutes at 800°C was added. This approach ensured that the measured mass function reached a plateau. According to Netzsch, 2018, the decomposition of inorganic fillers takes place between 900°C and 1100°C. Consequently, the selected maximum temperature during the experiment was 800°C. The measurements were conducted in a nitrogen atmosphere.

After performing the measurements, the inorganic content of the tested material can be evaluated with the corresponding Netzsch Proteus-Thermal Analysis software. Furthermore, the mass resin content of the laminates can be determined by applying a simple "Two-Step" procedure. The basic methodology is shown in figure 4-4. This procedure can be seen as a further development of the IPC-TM-650 2.3.13, 1994, where the resin content is evaluated by using a burn-off step in a furnace. By applying equation (2.1):

$$RC=100-\left[M^{IF+IR}-\left(\frac{M^{IF+IR}\cdot M^{IR}}{100}\right)\right] \quad (2.1)$$

the laminate mass resin content (RC) can be calculated. The evaluated inorganic mass content of the resin after step 1 is denoted as M^{IR}. In equation (2.1), M^{IF+IR} represents the inorganic content of the laminate, determined after the second step. The M^{IF+IR} consists of the inorganic glass fibre mass content (IF) and the inorganic mass content of the resin (IR).

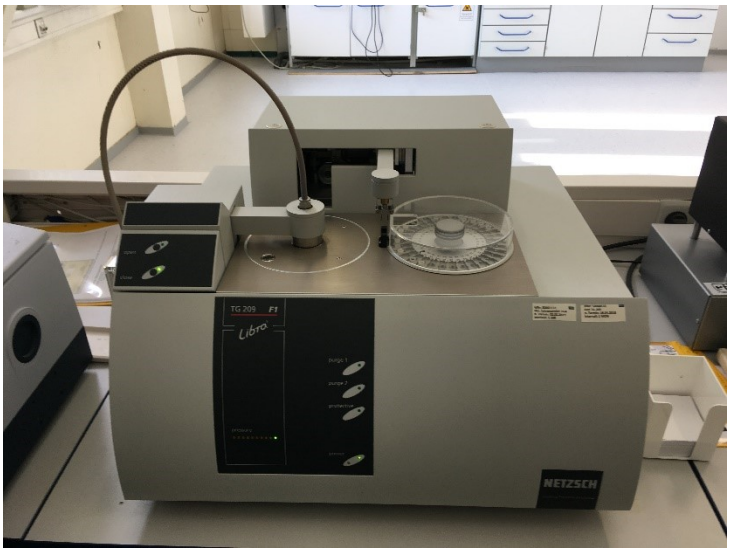

Figure 4-2: Used TGA apparatus TG 209 F1 Libra® from Netzsch-Gerätebau GmbH.

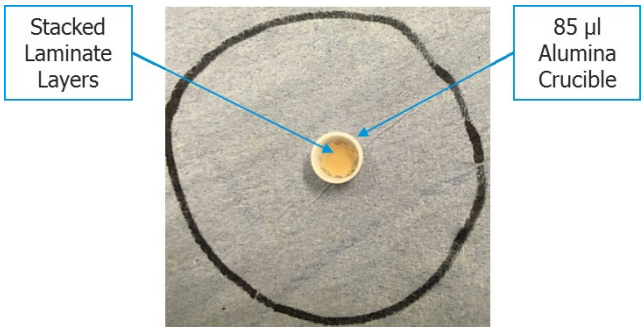

Figure 4-3: Stacked laminate specimens in crucible.

Table 4-1: Measured specimen weights for the TGA.

		Resin	Laminate 1	Laminate 2	Laminate 3
Measurement 1	[mg]	20,82	15,13	15,36	16,12
Measurement 2	[mg]	10,25	14,85	16,22	17,19
Measurement 3	[mg]	16,31	15,2	16,49	15,88
Measurement 4	[mg]	15,52	15,96	16,62	17,39

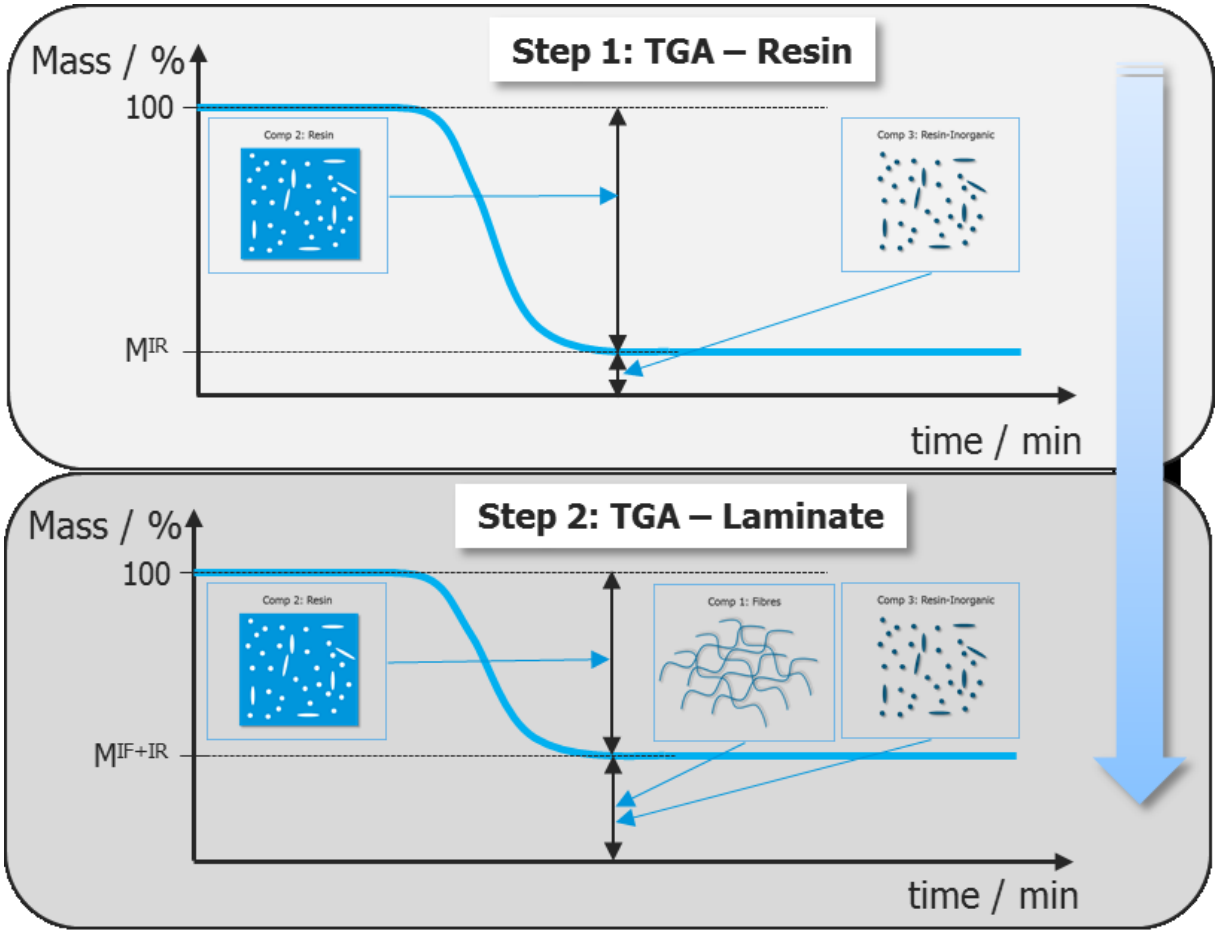

Figure 4-4: Two-Step procedure to determine the laminate resin content.

4.3 Monotonic Tensile Test

The experimental setup for the determination of the Poisson's ratio and Young's modulus is shown in figure 4-5. The monotonic tensile test was performed at the Institute of Materials Science and Testing of Polymers at the Montanuniversität Leoben under laboratory enviroment. All materials listed in table 3-2 were tested at room temperature and elevated temperatures (from 80°C to 240°C). The laminate specimens were tested in the 1, 2 and 45° direction. The influence of the panel position to the Young's modulus due to the lamination procedure was investigated more closely at room temperature. Therefore, the Young's modulus of laminate 2 was measured in direction 1 at different panel positions. The modulus in the 45° direction was measured at room temperature to check the specimen preparation methodology, especially the cutting reliability and quality. Four repetition measurements per temperature and direction were performed for the tested materials. The detailed measurement matrix of the tensile tests is represented in table 4-2.

Table 4-2: Measurement matrix for the monotonic tensile tests at room temperature and elevated temperatures.

Material	**Direction**	**Specimens per Temperature**						**Total**
		23°C	80°C	120°C	160°C	200°C	240°C	
Resin	-	4	4	4	4	4	4	24
Laminate 1	1	4	4	-	4	-	4	16
	2	4	4	-	4	-	4	16
	45°	4	-	-	-	-	-	4
Laminate 2	1	16[1)]	4	-	4	-	4	28
	2	4	4	-	4	-	4	16
	45°	4	-	-	-	-	-	4
Laminate 3	1	4	4	-	4	-	4	16
	2	4	4	-	4	-	4	16
	45°	4	-	-	-	-	-	4

[1)] Four measurements per panel position Pos. 2, Pos. 3, Pos. 5 and Pos. 6 at room temperature.

The universal tensile/pressure testing machine ZWICK Z010 (Zwick/Roell GmbH & KG, Ulm, Deutschland) was used for the test. For the measurements at elevated temperatures, the corresponding temperature chamber was utilized. A DIC system for 3-dimensional deformation analysis, was implemented to track the displacement. The ARAMIS (GOM – Gesellschaft für Optische Messtechnik GmbH, Braunschweig, Deutschland) was the applied tool. In addition, the specimens for the DIC were preliminarily coated with a layer of white varnish. Afterwards, a layer of black dye points was randomly sprayed on the white varnish layer. Appropriately, a thermocouple with an attached thermometer was used to monitor the temperature of the 500 N load cell, as can be seen in the laboratory setup for elevated temperatures in figure 4-5. The maximum allowable temperature of the load cell is 60 °C. To ensure no overheating of the load cell, a fan was placed behind it. With respect to the elevated temperatures, suitable high temperature pneumatic hoses were applied for the pneumatic opening and closing of the grips inside the oven.

Before executing the measurement, the specimen thickness and the width of the plane-parallel middle section of the specimen were measured to calculate the corresponding stress with the recorded force signal after the measurement. In the first step, the tensile specimen was fixed in the upper grip. In the second step, the force of the load cell was adjusted to zero. The corresponding software testXpert II of the universal tensile device offers the

function to maintain a constant gripping force, to eliminate unwanted loads on the specimen. As explained by Fahrenholz H., 2016, consequently the Young's modulus can vary up to 3% due to a compressive force to the specimen. This function was activated and the lower grip was pneumatically closed. After this procedure, the DIC could be started and the tensile test was executed. The procedure was used for the execution of the tensile test at room temperature. However, at elevated temperatures minor differences were introduced; after fixing the specimen in the upper grip, the door of the temperature chamber was closed. When the chamber reached the set temperature value, the specimen was fully fixed by closing the lower grip after giving the specimen an appropriate time to develop a homogenous heat profile. This procedure can be seen as quite challenging regarding specimen warpage, centric specimen fixation and safety measures due to the hot chamber.

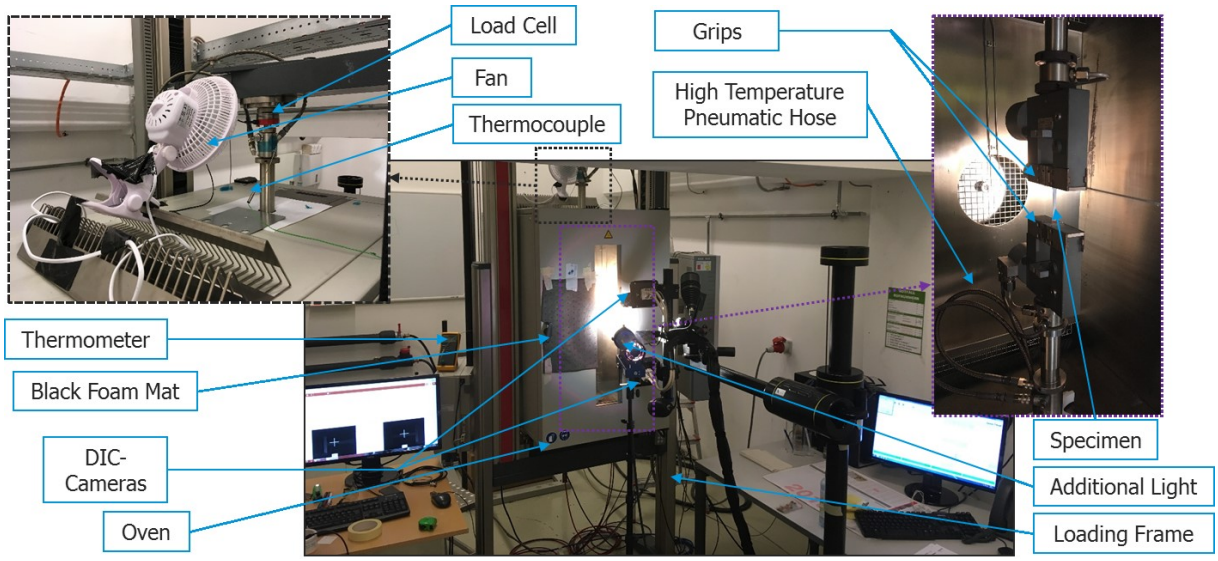

Figure 4-5: Experimental setup of the monotonic tensile test at elevated temperatures with a specimen inside the temperature chamber and additional, important components as marked.

In order to determine the above mentioned properties, the testing speed 1 mm/min was chosen according DIN EN ISO 572-1, 2010. As represented in equation (2.2), the evaluation of the Young's modulus was executed as secant modulus, at 0.05 (ε_2) and 0.25% (ε_2) strain at the corresponding stress level (Grellmann and Seidler, 2007). The Poisson's ratio is defined in equation (1.7). For the experimental evaluation, an optimization strategy according equation (2.3) was performed:

$$E=\frac{\sigma_2-\sigma_1}{\varepsilon_2-\varepsilon_1} \tag{2.2}$$

$$v_j^a = (v_1 + v_2)\frac{1}{2} + \left((v_1 + v_2)\frac{1}{2} + v_3\right) + \ldots + (v_{j-1}^a + v_j)\frac{1}{2} \tag{2.3}$$

where v_j is the actual calculated Poisson's ratio per increment, v_{j-1}^a is the averaged Poisson's ratio from the previous increment and v_j^a is the final Poisson's ratio from the last calculated increment. A result of this optimization procedure is plotted in the appendix (figure A-2).

4.3.1 Implementation of the DIC

Table 4-3 summarizes the applied parameters for the implementation of the DIC at room temperature and elevated temperatures.

The DIC cameras were calibrated before the measurement. The calibration gage CP20/55x45 was used and the calibration deviation for the laboratory setup was determined. At elevated temperatures, the DIC cameras had to record the images through the glass window of the oven door. This fact can be seen as problematic, because the inner side of the glass window unavoidably showed minor pollution. Light reflections due to the metallic inner surface of the oven caused difficulties as well. A black foam mat (marked figure 4-5) was pinned to the oven door to decrease the light reflection from the door itself. Because of this, the test parameters at elevated temperatures could not be adjusted to the room temperature parameters. Necessarily the calibration deviation was not within the specification of less than 0.05 pixels at elevated temperatures. However, the calibration deviation did not exceed 0.075 pixels. This increase has been considered as not significant and acceptable. Increasing the shutter time before the measurement and using more points for the strain distribution evaluation, enabled the evaluation of reasonable results at elevated temperatures, with respect to the Young's modulus. Figure 4-6a shows a shutter time response of a specimen surface at room temperature and elevated temperatures.

Table 4-3: Applied parameters for the DIC implementation at room temperature and elevated temperatures.

	Room Temperature	**Elevated Temperatures**
Calibration Deviation (Threshold Value: 0,5)	< 0,05 Pixels	0,05 - 0,075 Pixels
Calibration Object	CP20/55x45	CP20/55x45
Facet Size	20 Pixels	20 Pixels
Step Size	15 Pixels	15 Pixels
Calculation	Simple	More Points
Shutter Time	15 - 17 ms	20 - 25 ms
Recording Image Sequence	4 image/s	4 image/s

For the evaluation of the axial normal strain and transversal normal strain, the mean 1 and 2 strain components were calculated from the measured strain distribution. The resulting strain components are plotted in the appendix figure A-2a, respectively. Figure 4-6b represents a measured strain distribution map over the tested surface.

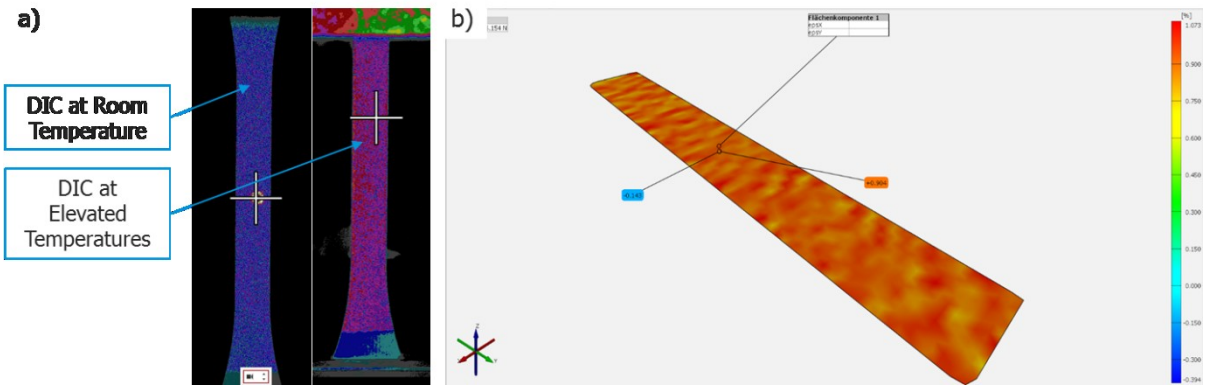

Figure 4-6: a) Shutter time response at room temperature and elevated temperatures. b) Measured strain distribution map.

4.4 Dynamic Mechanical Analysis

The storage modulus measurements of the materials listed in table 3-2 were implemented with a DMA/SDTA861^{e} (Mettler Toledo International Inc., Schwerzenbach, Switzerland) at AT&S HTB (Figure 4-7). Laminate specimens were tested in 1, 2 and 45° direction. The influence of the panel position to the storage modulus due to the lamination procedure was also investigated. Therefore, the temperature scanning of the storage modulus of laminate 2 was performed in direction 1 at different panel positions (similar to the 23°C entries in table 4-2). The DMA measurement is more sensitive to the T_g than the differential scanning calorimetry and thermo-mechanical analysis (Foreman et al., 2006). For this reason, the

DMA was also used to investigate the T_g of the materials to get also a first indicator of the transitions during the heating phase. Four repetition measurements were performed per direction for the sake of reproducibility.

A tensile cyclic loading mode was applied to all laminate specimens. According to Ehrenstein et al., 2003, the tensile mode is particularly suitable for thin fibre-reinforced composite materials. In addition, a static pre-load is suggested to exclude buckling of the specimens during the measurement. The DMA/SDTA861^e is unfortunately not capable of defining a static pre-force. As shown by Guttmann P., 2009, differences between the tensile and 3 point bending mode before the T_g could not be observed, with respect to epoxy materials. Because of these results, the resin specimens were also measured in the tensile mode. During the measurement the displacement was controlled and the force was indirectly measured by the spring deflection.

Before performing the DMA measurements, the specimen width and thickness were recorded. The tensile clamp which was used limits the specimen length to 9 mm, and is device-dependent. These values are needed by the DMA to calculate the stress from the measured force and the corresponding strains via the crosshead travel. Afterwards, the prepared DMA tensile strips were inserted in the tensile clamp as shown in figure 4-8b. The components of the used tensile clamp are represented in figure 4-8a. Particular care was taken to fix the specimens in the clamp by applying an approximately similar torque moment to each fixation screw, by feeling. In order to ensure reproducibility, practically the same torque moment was applied manually to the clamps before every measurement.

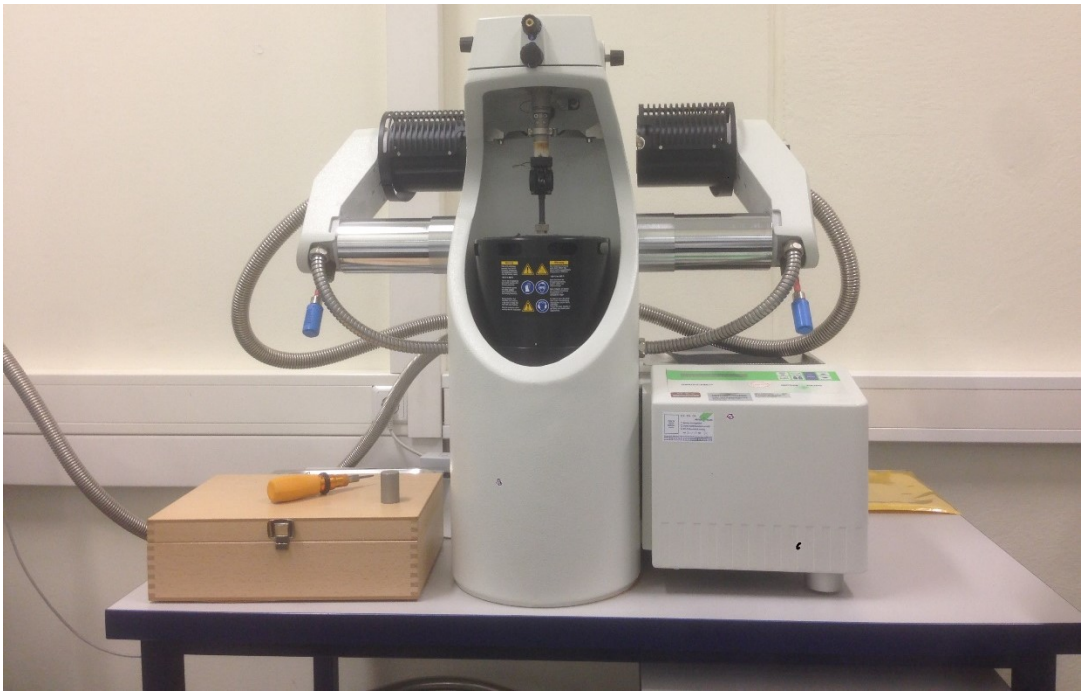

Figure 4-7: Dynamic Mechanical Analyser DMA/SDTA861[e] from Mettler Toledo International Inc..

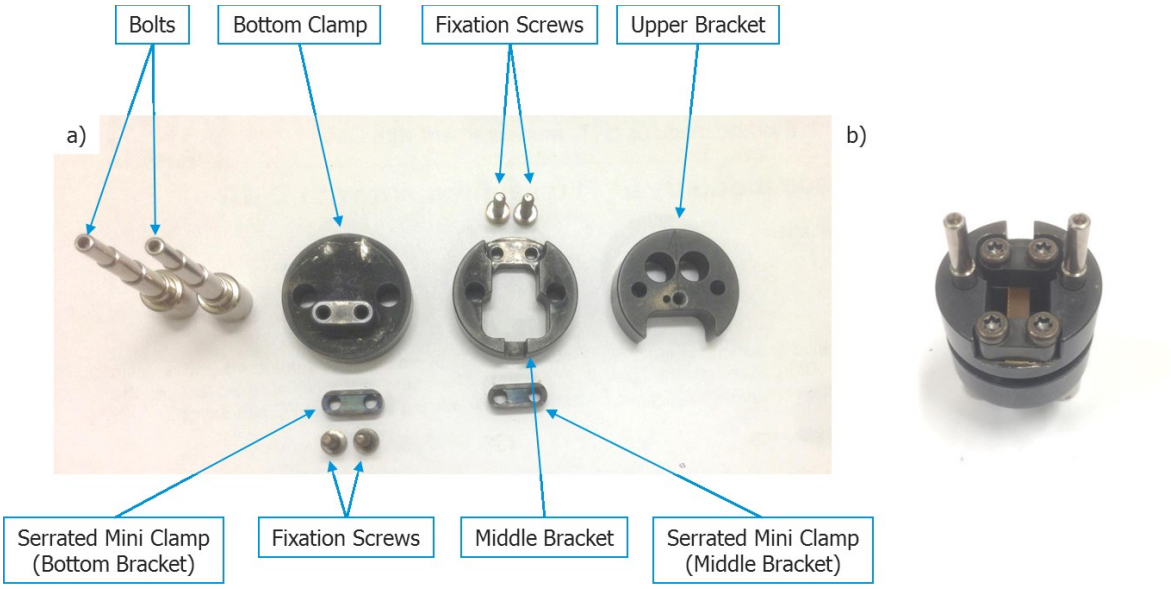

Figure 4-8: Individual components (a) and the assembled (b) tensile clamp used for the DMA measurements.

Table 4-4 shows the implemented test parameters. All measurements were made in the temperature range from 20°C to 260°C. The linear-viscoelastic region was determined as outlined in chapter 2.5.4. The results of the force scan, with respect to the laminate specimens, are shown in the appendix (figure A-3). Referring to these results, an 8 µm displacement amplitude was applied to the laminate specimens and a 2 µm amplitude to the resin specimens. As described by Mettler Toledo, 2005, the static offset is especially

recommended for fragile specimens. Consequently, a 150% static force offset depending on the applied amplitude was chosen. The static offset ensured a constant tension of the thin laminate specimens during the measurement to exclude buckling effects without using a static pre-load. The DMA/SDTA861^e applies the static offset at the start of the measurement. In some cases the DMA/SDTA861^e started the measurements somewhere around 25°C. Therefore, a linear interpolation was done to describe the modulus in the missing temperature window between 20 to 25°C.

The peak temperature of the tan(δ) $T_{g_tan(\delta)}$ was used for the evaluation of the glass transition temperature. The chance of evaluation errors is usually minimised by using the peak temperature of the loss factor. This can be attributed to the fact that the evaluation is easier to perform than, for example, by using the onset/offset method. For the evaluation, a linear representation of the loss factor was used. Alternatively, the peak of the loss modulus can also be used for the T_g (Ehrenstein et al, 2003). The T_g evaluation method used in this study is shown in the appendix Figure A-1, respectively.

Table 4-4: Test parameters for measurements in the tensile mode of the DMA/SDTA861^e.

Auto-Offset:	150%
Atmosphere:	Nitrogen
Displacement Amplitude Laminate:	8 µm
Displacement Amplitude Resin:	2 µm
Controlled:	Displacement
Frequency	1 Hz
Heating Rate	2 K/min

4.5 Cross Sectioning

The cross sections of the laminate specimens (direction 1 and 2) were prepared by the physics laboratory in AT&S HTB. A Nikon eclipse LV100DA-U microscope was used for the analysis of the yarn geometry. Optical magnifications between 50X and 200X were used.

5 NUMERICAL

In order to investigate the engineering constants at the numerical level, another purpose of this study was the generation of a micromechanical model based on the experimental results. Consequently, the numerical outcome should be compared to the experimental results.

5.1 General Considerations

In general, the temperature dependent engineering constant (EC(T)) of a two-phase laminate structure can be written as a function of:

$$EC(T)=f\left[E(T)^{(m)},\ E^{(f)},\xi^{(m)},\xi^{(f)},v(T)^{(m)},v^{(f)},\ Ge^{(f)}\right] \tag{4.1}$$

where $E(T)^{(m)}$, $\xi^{(m)}$ and $v(T)^{(m)}$ are the temperature dependent Young's modulus, volume content and temperature dependent Poisson's ratio of the resin, respectively; $E^{(f)}$, $\xi^{(f)}$ and $v^{(f)}$ are the Young's modulus, volume content and Poisson's ratio of the fibres, respectively; and $Ge^{(f)}$ is the fibre architecture. These property definitions are shown in figure 5-1. The properties of the glass fibres are assumed to be non temperature dependent.

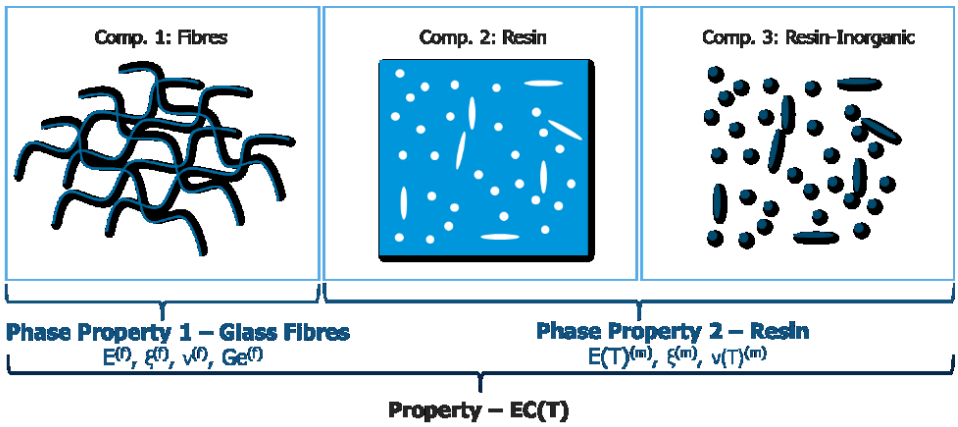

Figure 5-1: Property definition of a two-phase laminate structure.

In order to improve the micromechanical assumption, the different fibre volume fractions in 1 and 2 direction are taken into account by using the following equations:

$$\xi^{(f)}_{overall}=\frac{1}{1+\left(\frac{1-\xi^{(f)}_{m}}{\xi^{(f)}_{m}}\right)\frac{\rho^{(f)}}{\rho^{(m)}}} \tag{4.2}$$

$$\xi^{(f)}_{1}=\xi^{(f)}_{overall}\left(\frac{\text{WARP count}}{\text{WARP count + FILL count}}\right) \tag{4.3}$$

$$\xi_2^{(f)} = \xi_{overall}^{(f)} \left(\frac{\text{FILL count}}{\text{FILL count + WARP count}} \right) \tag{4.4}$$

where $\rho^{(m)}$ and $\rho^{(f)}$ are the densities from the resin and the fibres, respectively; $\xi_{overall}^{(f)}$, $\xi_1^{(f)}$ and $\xi_2^{(f)}$ are the overall volume content (Ehrenstein, 2006), volume content in direction 1 and volume content in direction 2 of the fibres, respectively; and $\xi_m^{(f)}$ is the mass fibre content. The corresponding WARP and WEFT count per cm are defined in the IPC-4412A, 2008, specification. With the intention of enhancing the micromechanical assumption further, the ellipsoidal yarn aspect ratio r can was taken into account by utilizing following assumption for a two yarn minimum size unit cell:

$$\xi_D^{(f)} = \frac{2 \cdot A_D^{(f)}}{A_D} \tag{4.5}$$

where $\xi_D^{(f)}$ is the fibre volume fraction in direction 1 or 2, similar to equation 4.3 and 4.4. The index D in equation 4.5 and the following equations stand respectively for the direction 1 or 2. These volume fractions are in direct correlation with the total fibre area (A_D) of a rectangular cuboid and a two-yarn fibre-only area ($2 \cdot A_D^{(f)}$) of an ellipse, in the corresponding direction 1 or 2. The area of one side of a rectangular cuboid in the direction 1 or 2 can by expressed by equation 4.6:

$$A_D = t \cdot s_D \cdot 2 \tag{4.6}$$

where t is the cuboid thickness and s_D is the spacing between two yarns, in the direction 1 or 2. The spacing can be calculated as the inverse of the fabric count per cm in the corresponding direction. The area ($A_D^{(f)}$) and the aspect ratio of an ellipse are defined in equation 4.7 and 4.8, with respect to the ellipse semi-major axis a and semi-minor axis b.

$$A_D^{(f)} = a \cdot b \cdot \pi \tag{4.7}$$

$$r = \frac{a}{b} \tag{4.8}$$

Thus, putting equation 4.6, 4.7 and 4.8 into Equation 4.5, the ellipse axis b_D can be deduced as a function of the aspect ratio, in the direction 1 or 2:

$$b_D = \sqrt{\frac{\xi_D^{(f)} \cdot A_D}{\pi \cdot r \cdot 2}} \tag{4.6}$$

5.2 Micromechanical Modelling

The geometrical computing and FE-Mesh generation of the periodically repeating unit cell (RUC) was executed by using the textile geometric modeller TexGen v3.9.0 (Composites Research Group, Nottingham, England). Table 5-1 summarises the TexGen input data for the RUC modelling based on the IPC-4412A, 2008, specification and the analytical equations established in the previous chapter 5.1.

Therefore, the density of the resin and the resin mass content of the laminates were determined in the experimental part of the presented study. These experimental outcomes are reviewed in the results section (chapter 6.1.1 and chapter 6.1.2). The density of the fibres ($\rho^{(f)}$) were assumed as 2,59 g/cm^3 (Jawitz and Jawitz, 2007). The RUC thickness is listed in table 3-2. Two different yarn aspect ratios were implemented; an aspect ratio of 7, in both 1 and 2 direction according AT&S internal suggestions, and the measured aspect ratios based on the performed cross-sectioning. The individual results are presented in appendix table A-1 and table A-2. Adapted from Frewein, 2017, no further homogenization of the yarn itself was executed to ensure a correct representation of the overall RUC resin content; this means that the yarn itself is represented as a glass-only structure.

Table 5-1: Input parameter for the RUC generation in TexGen. The (1 / 2) entries are the parameters in 1 and 2 direction, respectively.

RUC	Aspect Ratio (1 / 2)	Spacing (1 / 2)	Overall Fibre Volume Content	Fibre Volume Fraction (1 / 2)	Yarn width (1 / 2)	Yarn height (1 / 2)
	[-]	[µm]	%	%	[µm]	[µm]
Lam 1_v1	7 / 7	362 / 348	21,6	10,6 / 11,0	131 / 131	19 / 19
Lam 1_v2	25,7 / 7,5	363 / 348	21,8	10,9 / 10,9	136 / 251	18 / 10
Lam 2_v1	7 / 7	339 / 339	25,9	13,0 / 13,0	115 / 115	16 / 16
Lam 2_v2	9,6 / 28,1	339 / 339	21,6	10,6 / 11,0	230 / 134	8 / 14
Lam 3_v1	7 / 7	469 / 469	21,8	10,9 / 10,9	180 / 180	26 / 26
Lam 3_v2	14,9 / 9,9	470 / 469	25,9	13,0 / 13,0	214 / 263	21 / 18

For example, the RUC Lam 1_v2 is shown in figure 5-1 a. To ensure a stable and fast calculation approach, a simple voxel meshing technique was applied to all RUCs; the shape of the mesh is constructed entirely from orthogonal elements (Crookston et al., 2007). Pre-defined voxel count values of 50x50x50 were the parameters used. The voxel meshing technique guarantees a periodically repeating mesh, which is a base requirement for the

application of a periodic boundary condition, according to Dassault Systèmes, 2017. However, a more detailed representation of the RUC was not within the scope of this thesis and the present approach had to be sufficient to generate first results. The generated RUC's were transferred to the FE-Software Abaqus® 2017 (Dassault Systemes Simulia Corp., Waltham, USA). Figure 5-2 b) represents the model of the RUC Lam 1_v2 with the generated voxel mesh in Abaqus®. Linear reduced hexahedral elements (C3D8R) were assigned to the mesh. The Young's modulus and Poisson's ratio from the tensile test were applied as input data for the virtual resin property definition; the input data for E-glass were selected according to Jawitz and Jawitz, 2007.

To investigate the effects of the chosen boundary condition (BC) on the modulus and Poisson's ratio more closely, periodic (PBCs) and periodic shell boundary conditions (PSBCs) were applied to the RUCs. As mentioned in Dassault Systèmes, 2017, the PSBCs is suitable to predict properties of thin shell-like structures. The micromechanics plugin for Abaqus®/CAE offers the possibility to apply the two mentioned BCs and was therefore the selected tool. There are two options to apply the BCs with the Plugin: First, the BC is applied automatically to the RUC; second, the BC is applied manually by defining a load history. By choosing option one, usually the engineering constants are calculated automatically. Option two offers the possibility to calculate the averaged strain and stress concentration tensors, and then the corresponding EC by utilizing equations presented in chapter 2.4 and 2.5.3. The PBCs were applied automatically to the RUCs. By contrast, for the investigation of the PSBCs the far-field loads were applied manually in the 1 and 2 direction to investigate the RUC response. This procedure allowed a very basic and careful investigation of the response, because there is very little experience with this type of BC at AT&S HTB. The shear moduli were not investigated in this study.

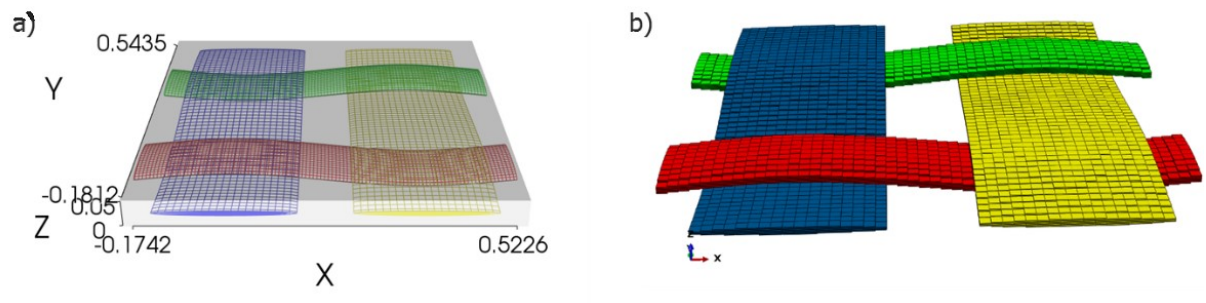

Figure 5-2: a) Geometric implementation of the RUC in TexGen. b) Model of the RUC in the FE-Software Abaqus® represented with a voxel mesh (only the yarn is shown).

Figure 5-3 summarizes the strategy used for implementing the micromechanical model in this thesis. All numerical investigations were executed at room temperature.

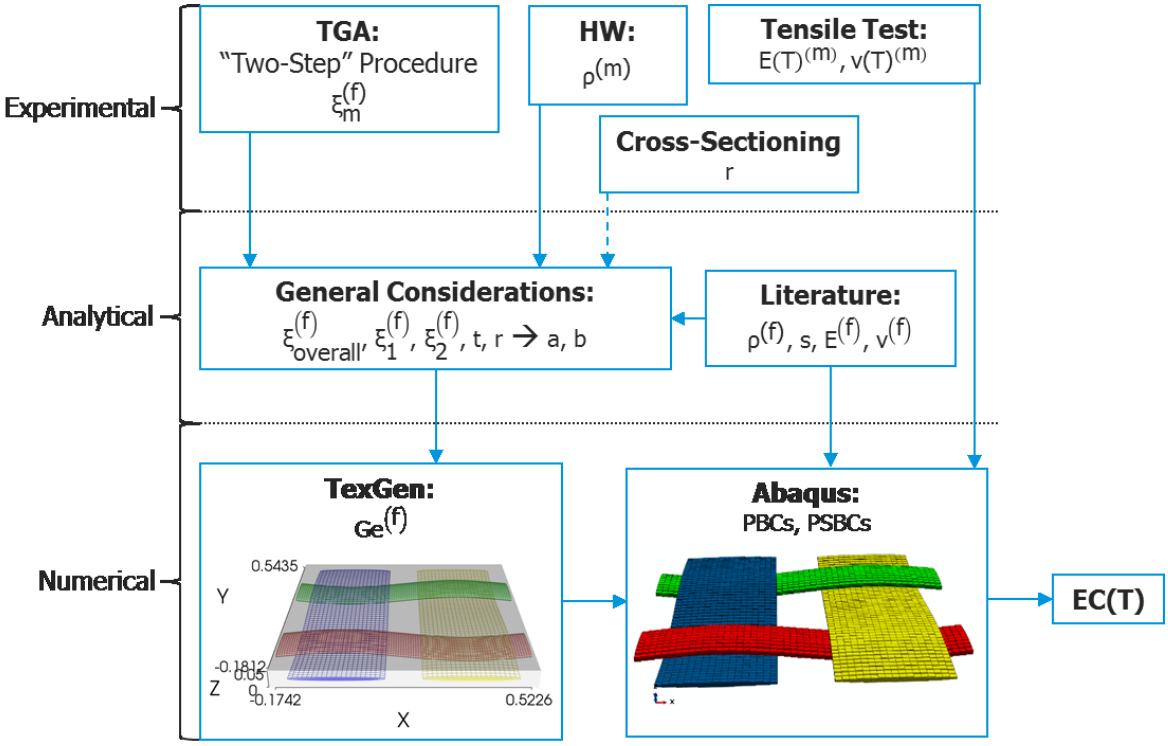

Figure 5-3: Summarized strategy for implementing the micromechanical model.

6 RESULTS

6.1 Experimental Results

6.1.1 Evaluation of the Density

The hydrostatic weighing measurements were carried out to determine the density of the resin for the numerical part and for getting a first indicator of the laminate composition. The mean density results obtained from the hydrostatic weighing measurements are plotted with their standard deviation (SD) in figure 6-1. Table 6-1 lists the individual measurement results. Generally, all results are in a good agreement with the literature and the data scattering is in an acceptable range. As can be seen in figure 6-1, the resin has the lowest density. Meanwhile, the density of the laminates, starting from laminate 1 to laminate 3, increases.

As found in Ehrenstein et al., 2013, the density of an unreinforced epoxy resin is between 1.17 and 1.25 g/cm^3. It seems highly possible that a high amount of fillers or other possible additives caused the increased measured resin density of 1.41 g/cm^3. The consequence of the higher laminate density can be derived by the presence of glass fibres. Fellner, 2012, mentioned that the density of the laminates is linked to the resin content; the density decreases with increasing resin content. This assumption indicates that laminates 1 and 2 should have a similar resin content. Hence, laminate 3 should have the lowest resin content. The observed laminate densities are consistent with reported results from Fellner, 2012 and Coombs, 2001.

Table 6-1: Individual density results with mean values and standard deviation (SD) from the hydrostatic weighing measurements.

Matetrial	[-]	**Resin**	**Laminate 1**	**Laminate 2**	**Laminate 3**
Mesurement 1	[g/cm^3]	1,415	1,684	1,693	1,915
Mesurement 2	[g/cm^3]	1,406	1,438	1,548	1,798
Mesurement 3	[g/cm^3]	1,392	1,519	1,438	1,767
Mesurement 4	[g/cm^3]	1,408	1,424	1,466	1,632
Mean of Measurements	[g/cm^3]	1,405	1,516	1,536	1,778
SD of Mean Results	[g/cm^3]	0,008	0,103	0,100	0,101

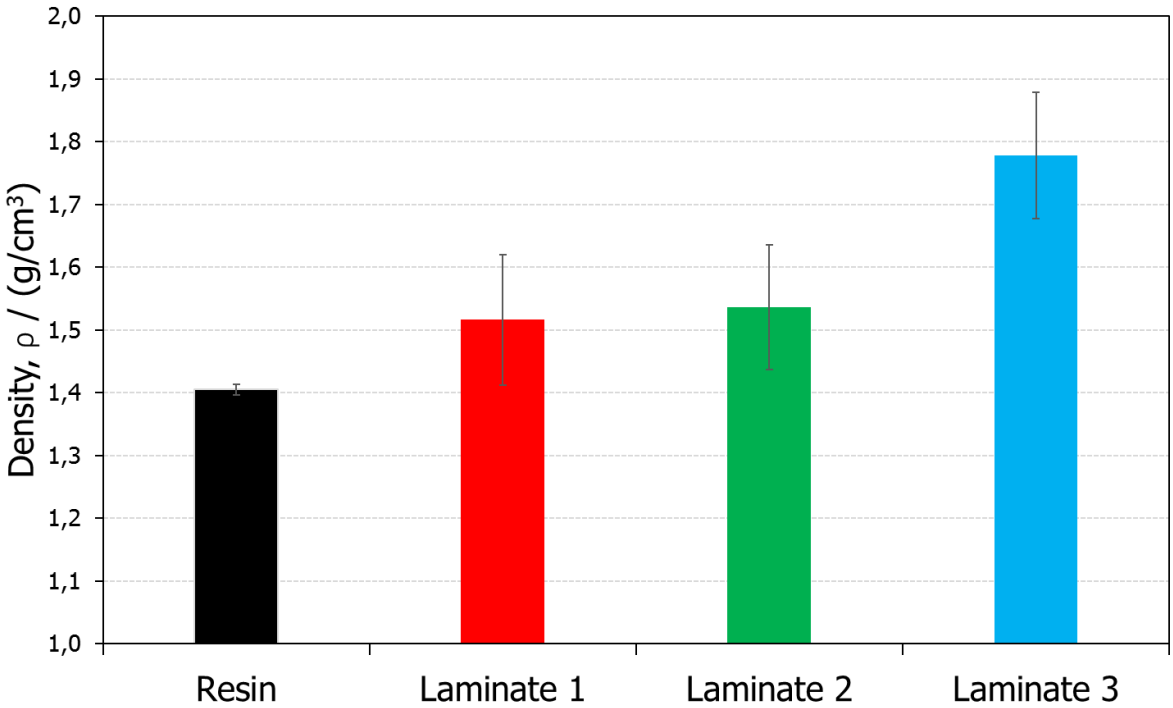

Figure 6-1: Measured mean densities of the investigated materials with standard deviation.

6.1.2 Evaluation of the Inorganic Filler Content

To investigate the inorganic filler content of the materials, the TGA was carried out. Figure 6-2 represents the mean mass loss as a function of the oven temperature and the time. In general, the standard deviations of the individual results were marginally low. The results at 200 minutes represent the rest mass after the measurement. As mentioned in chapter 4.2, by using a maximum oven temperature of 800°C the inorganic contents should not decompose.

Several interesting characteristics of the examined materials can be seen in figure 6-2. For all materials the decomposition started somewhere around 300°C. The resin shows an inorganic content of 38.5 mass percentage after holding 120 minutes at 800°C. This result can be seen as a quite significant inorganic content. First of all, as already mentioned in the introduction, small particles are added to the resin in order to improve the properties of the compound. It can be assumed that this amount of inorganic particles is added in order to enhance specific properties of the resin in the product application. Since the composition of the epoxy is unknown, only assumptions could be made of the inorganic filler types.

According to the results in figure 6-2, laminate 1 and 2 should have a similar inorganic filler and glass fibre content. Meanwhile laminate 3 shows the highest amount of fillers and glass fibres. In order to evaluate the resin content of the laminates for the numerical part of this

study, the "Two-Step" procedure descript in chapter 4.2 was utilized. The outcome of this method is shown in table 6-2. To check the plausibility of the laminate resin content, a simple "Rule of Mixture" formulation according to Reuss, 1929, can be used:

$$\rho=\left(\frac{\xi_m^{(m)}}{\rho^{(m)}}+\frac{1-\xi_m^{(m)}}{\rho^{(f)}}\right)^{-1} \tag{6.1}$$

where $\xi_m^{(m)}$ is the observed resin content; $\rho^{(m)}$ and $\rho^{(f)}$ are the densities of the resin and the fibres, respectively; and ρ is the homogenised laminate density. The fibre density is assumed to be 2.59 g/cm^3 (Jawitz and Jawitz, 2007) and the resin density is taken from the hydrostatic weighing results. Applying equation (6.1) results in a density of 1.662 g/cm^3, 1.663 g/cm^3 and 1.712 g/cm^3 for laminate 1, laminate 2 and laminate 3, respectively. These calculated densities, based on the measured resin content, are in quite similar ranges as the experimental results shown chapter 6.1.1.

Frick and Stern, 2011, recommended a combination of two individual purge gas phases during the heating up segment for the determination of the inorganic filler content. In the first heating phase, a nitrogen atmosphere is recommended. By doing so, only pyrolized carbon black and fillers should remain in the crucible afterwards. In the second step it is suggested to blow an oxygen atmosphere into the oven in order to burn off of the remaining carbon black; only inorganic fillers should be present after the oxygen burn-off inside the crucible. The TGA apparatus at AT&S HTB is not able to use oxygen as a purge gas, because an oxygen supply is not available. Therefore, investigations regarding the use of oxygen to the inorganic filler content after the burn-off were not made. The influence of the chosen purge gas may have an influence on the measurement outcome and should be investigated in future studies.

However, the observed TGA results are in the expected ranges. To determine the correct laminate resin content, the inorganic filler content of the highly filled resin itself can be seen as an important parameter. The evaluated laminate resin content in table 6-2 was used as an input for the numerical part of the present study.

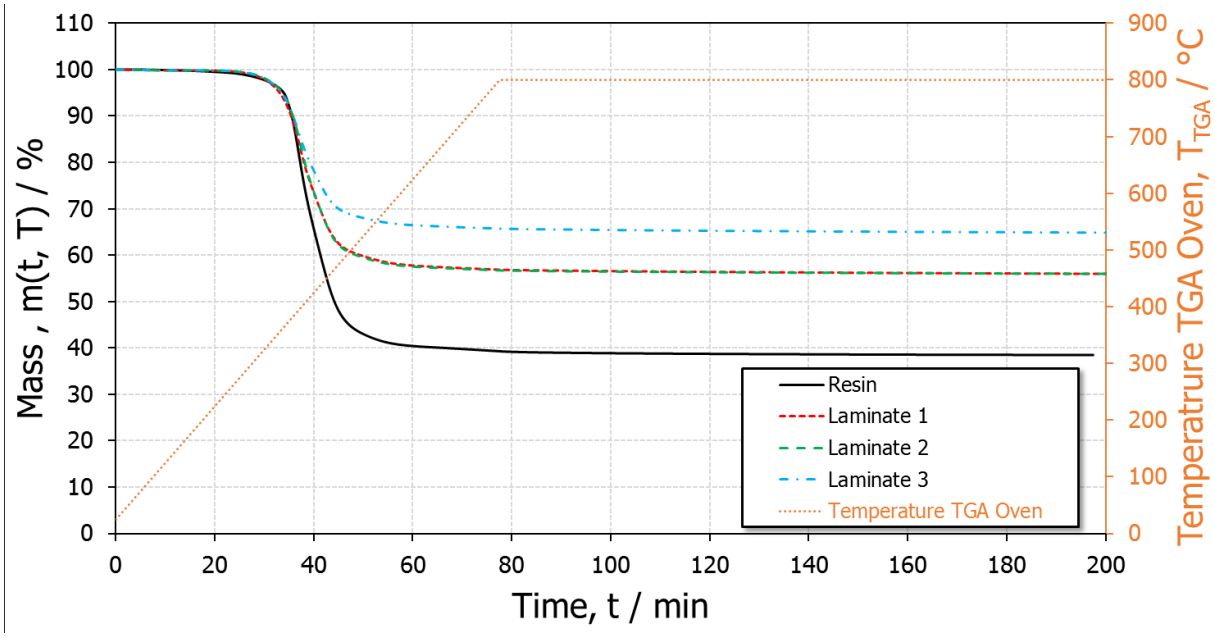

Figure 6-2: Mean mass loss as a function of the oven temperature and time, obtained from the TGA.

Table 6-2: Results obtained from the TGA measurement by applying the "Two-Step" procedure.

Material	**M^{IR}**	**M^{IF+IR}**	**RC**
[-]	[%]	[%]	[%]
Resin	38,5	-	-
Laminate 1	-	54,8	66,3
Laminate 2	-	55,1	66,1
Laminate 3	-	63,7	60,8

6.1.3 Evaluation of the Poisson's Ratio

In order to investigate the resin and in-plane laminate Poisson's ratio at room temperature and elevated temperatures, the monotonic tensile test implemented with DIC was conducted. Figure 6-3 represents the mean Poisson's ratio of the resin specimens obtained from the tensile test with standard deviation over the temperature.

The mean resin Poisson's ratio results can be seen as reasonable over the measured temperature range by using the optimization strategy for the evaluation described in chapter 4.3, shown in the appendix figure-A2. In addition, a stable Poisson's ratio development over the whole temperature range was observed; the Poisson's ratio increased from its initial value of 0.32 at room temperature close to 0.5 at elevated temperatures. The sudden slight decrease of the mean resin Poisson's ratio at 240°C can be seen as not

significant. As depicted in figure 6-3, the standard deviations of the mean results at the individual temperature steps are reasonably good, except for the results at 120°C and 200°C. During the measurements at those temperature levels significant problems with the lower pneumatic grips occurred due to a damaged pneumatic valve; the gripping force of the lower grip decreased and slipping effects occurred.

Previous studies showed that the Poisson's ratio of an epoxy-based thermosetting material can be between 0.27 and 0.38 at room temperature (Amber et al., 2012, Grellmann and Seidler, 2007). This literature supports the measured mean Poisson's ratio at room temperature. The limit of the Poisson's ratio of an isotropic body is 0.5 (Callister and Rethwisch, 2013). The rapidly increasing Poisson's ratio between 80°C and 160°C implies that the cross-linked polymer chains gain more mobility, owing to a significant increase of the free volume. This result can be associated with a glass transition. The detailed analysis of the glass transition temperature takes place in chapter 6.1.5. After 160°C, the Poisson's ratio asymptotically approaches the 0.5 limit and therefore incompressible rubberlike material behaviour. This trend of the investigated epoxy at elevated temperatures are in good agreement with another well reported study of a different epoxy resin system (Amber et al., 2012). The obtained resin Poisson's ratio at elevated temperature can be seen as a valuable input for future micromechanical studies.

The results of the mean in-plane Poisson's ratio at room temperature and elevated temperatures obtained from the monotonic tensile test are illustrated in figure 6-4 and figure 6-5. The in-plane Poisson's ratio v12 was obtained from tensile specimens in direction 1 (figure 6-4) and the in-plane Poisson's ratio v21 was obtained from tensile specimens in direction 2 (figure 6-5). Equation (1.4) defines the relationship between v12 and v21. Generally speaking, a high standard deviation for all measurements at elevated temperatures was observed. Figure A-4 in the appendix shows the increasing standard deviation of the mean v12 over the temperature from laminate 1. Table A-3 in the appendix lists all the Poisson's ratio results which were obtained.

The results at room temperature are close to each other for v12 and v21. In addition, generally low standard deviations were obtained. As displayed in figure 6-4, the mean v12 of Laminate 1 and 2 shows an almost stable behaviour with a slight tendency to decrease with increasing temperature. Meanwhile, the mean v12 of laminate 3 suddenly increases at 240°C. Comparing figure 6-4 to figure 6-5, a similar behaviour of laminate 3 can be observed. The mean v21 of laminate 2 shows also a stable trend with a slight tendency to

decrease. For laminate 1, inconsistent trends between the two in-plane Poisson's ratios were observed.

Previously obtained results at AT&S HTB of the in-plane Poisson's ratio for related fabric styles are in good agreement with the measured results, with respect to the observations at room temperature. Cerbu et al., 2011, presented similar results for a seven-layer epoxy fabric. As mentioned before, the results at room temperature are close to each other. This finding can conclude that the in-plane Poisson's ratio is not strongly dependent on the investigated fabric types, the pressed layers and the fibre volume fraction. Similar conclusions regarding the effects of the fibre volume fraction were reported by Okoli and Smith, 2000. In this study, it is assumed that with a certain fibre fraction (15 to 40 mass percentage) the Poisson's ratio approaches the value of a glass-only specimen. It is likely that this assumption can be supported in the present study.

There is a strong possibility that the excessive data scattering of the laminate results at elevated temperatures can be linked to measurement problems attributed to the high temperatures. As mentioned in chapter 4.3.1, the standard deviation of the DIC was not within the suggested tolerance. Additionally, the specimens showed significant warpage after being put into the temperature chamber and heated up to the predefined temperature level. This suddenly appearing warpage can be attributed to the coefficient of thermal expansion mismatch, due to the sprayed layer of dye and additionally to low specimen thickness. When closing the lower grip, the specimen was twisted in the fixation and was not in a centric position. A consequence of a not centric, twisted laminate specimen is a wrong axial normal and transverse normal strain outcome from the DIC. Unfortunately, this occurred quite frequently at elevated temperatures. Measures such as repositioning a not centric specimen were not always successful and quite challenging because of the hot environment. It can be assumed that the obtained data at elevated temperatures should not be used for the implementation in a FEA material model. When applying equation (1.4) with the obtained moduli from the tensile test, unrealistic and incompatible results were observed.

Nevertheless, the Poisson's ratio evaluation of the thin laminate specimens at elevated temperatures was a valuable trial. There is a lot of room for improvement in future studies.

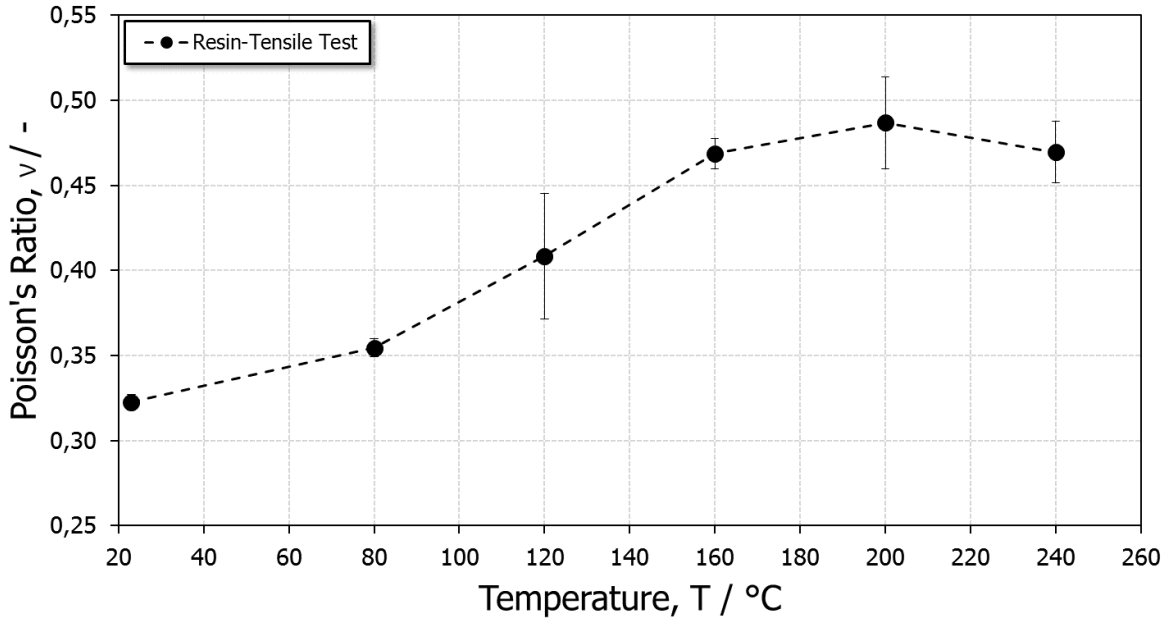

Figure 6-3: Mean Poisson's ratio results of the resin with standard deviation obtained from the monotonic tensile test over the temperature.

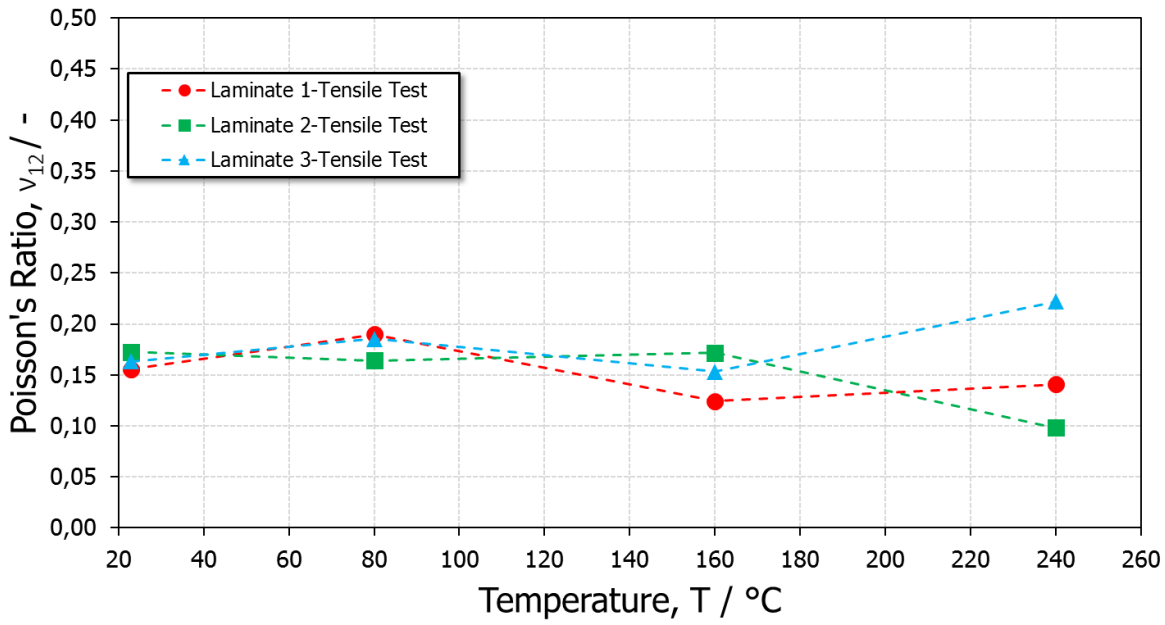

Figure 6-4: Mean in-plane Poisson's ratio v12 of the investigated laminates over the temperature.

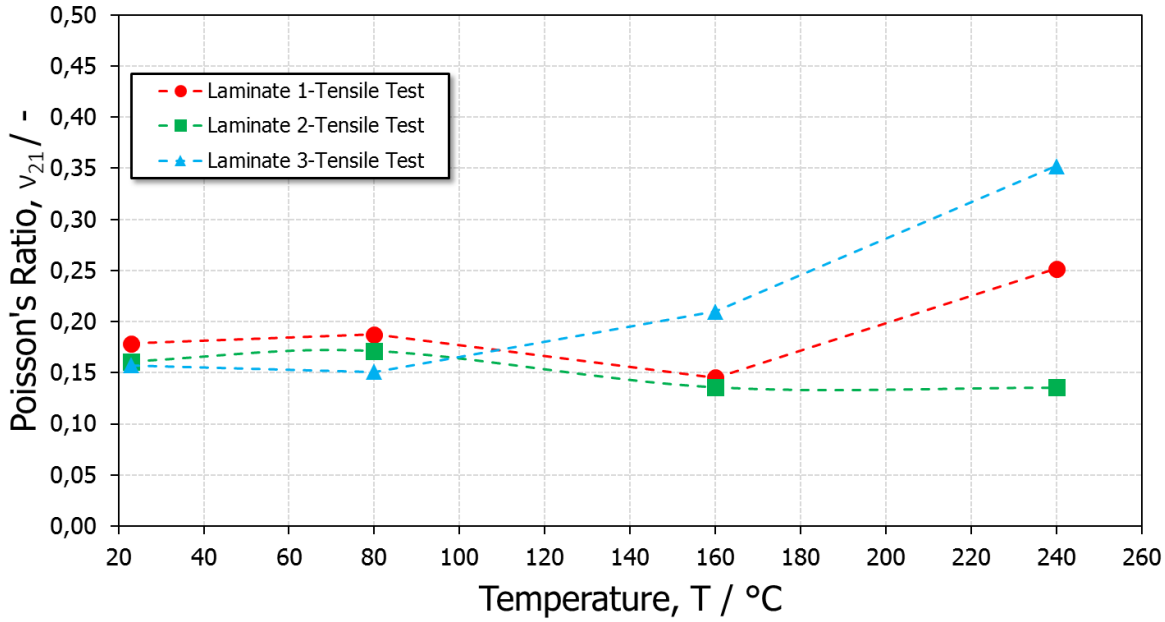

Figure 6-5: Mean in-plane Poisson's ratio v21 of the investigated laminates over the temperature.

6.1.4 Evaluation of the Modulus at Different Panel Positions and in 45° Direction

As outlined in chapter 3, the modulus in direction 1 of laminate 2 was investigated at different panel positions by monotonic tensile tests at room temperature and DMA measurements, to check the influence of the press procedure. Figure 6-6 shows the experimental findings at room temperature.

As illustrated in figure 6-6, the moduli at different positions are noticeably close to each other, for both tensile test and DMA. The different modulus outcome regarding the measurement technology is discussed in chapter 6.1.5. There seems to be no significant tendency to resin rich or poor spots at different panel positions, due to the assumption that the modulus is driven by the volume content.

The temperature scanning of the modulus executed by the DMA, is represented in figure 6-7. The drop of the storage modulus between 120 and 240°C indicates a glass transition. However, the evaluated glass transition temperatures are listed in the following chapter in table 6-3. The storage modulus shows higher values at the outer panel position 3 and 6 before and after the T_g. It can be assumed that at these positions higher fibre volume fractions can be expected due to a resin loss at the panel edges. Unfortunately, specimens

at position 1 and 4 were not available to support this assumption further, in terms of the other panel edge. As already outlined in figure 3-8, after conditioning the specimens, significant warpage occurred. It seems plausible that this warpage occurred due to the chemical shrinkage of the epoxy (Zündel, 2018) when post-curing the specimens in the temperature chamber. The chemical shrinkage combined with an additional fabric shift initiated by the resin flow during lamination could be a first indicator for a not fully developed homogenous resin distribution after laminating the PPs. To more scientifically support this theory, TGA measurements can be performed at the different panel positions in a systematic way to evaluate the correct fibre content.

It should be mentioned that the individual results obtained by the DMA showed a noticeable data scattering (appendix figure A-7). However, the individual results of laminate 1 and 3 showed only a marginal data scattering by utilizing the same specimen preparation approach (appendix figure A-5 and A-6). Thus, careful interpretation of this finding leads to the assumption that the expected data scattering can be attributed to the press procedure and the influence of the introduced specimen warpage of the two-layer build-up after the post-curing conditioning.

However, this observed position dependency of the modulus can be seen as minor. Previous studies at AT&S HTB showed: using the in-house laboratory press for the specimen preparation lead to considerable modulus differences at different panel positions, even at room temperature. In the present study, effects at room temperature were not significantly noticeable (figure 6-6). The modulus position dependency observed by the DMA can be seen as not ideal but within an acceptable range.

To investigate the cutting reliability of the automated specimen preparation methodology, the modulus in 45° direction of all three laminate materials was investigated. The tensile test at room temperature and the DMA were the applied tools. According to AT&S internal experience, usually the modulus of manually prepared tensile test or DMA tensile strip specimens in the 45° direction show a bigger data scattering. As could be shown in figure 6-8 when comparing tensile test and DMA results at room temperature, the standard deviation of the mean results differs only slightly. Typically, the modulus dependency of the resin content is also noticeable. Although laminates 1 and 2 have similar resin contents (chapter 6.1.2), the individual laminate moduli in 45° direction differ quite strongly. The spacing between the fibre bundles, shown in table 5-1, could have caused this interesting effect; laminate 2 has a smaller spacing than laminate 1, hence, this smaller spacing could

cause a stiffer response when loading the specimens in the 45° direction. Nevertheless, the results are in a good range and the standard deviation is quite low, which indicates a reliable cutting procedure in the 45° direction. Observing curves obtained from the DMA temperature scanning in appendix figure A-8, similar conclusions can be drawn.

The results point out that the methodology from chapter 3.2 can produce reliable moduli results with respect to the different experimental methods.

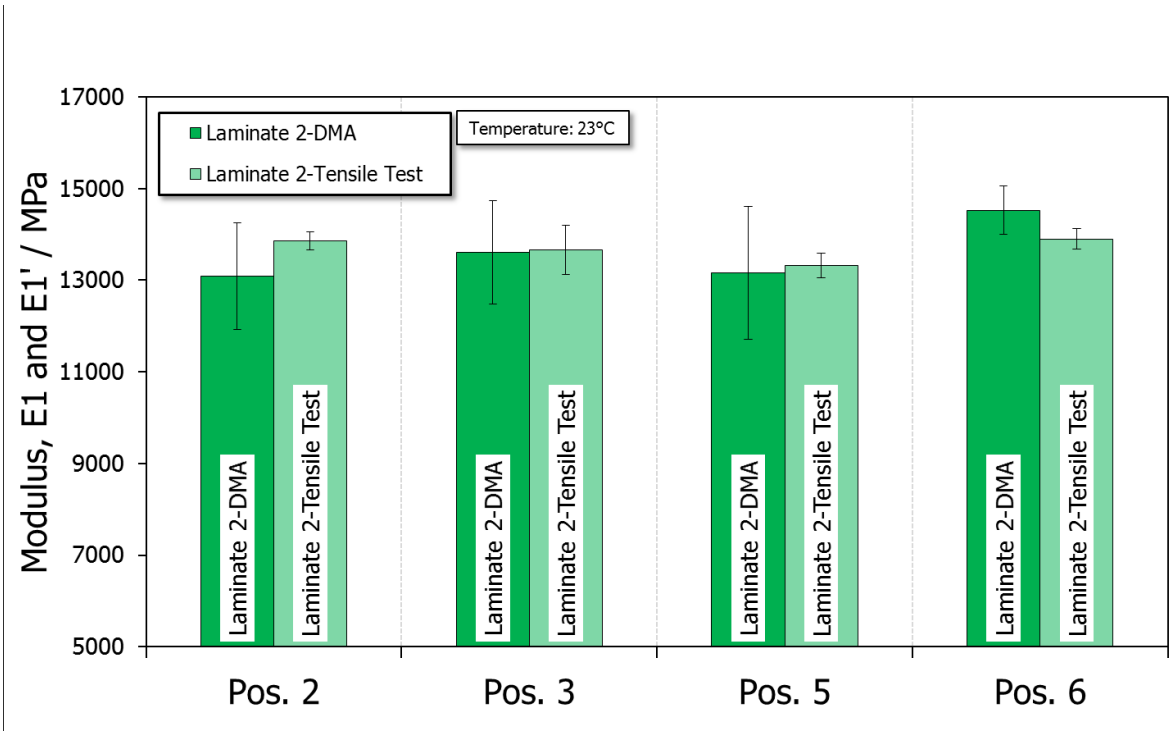

Figure 6-6: Modulus at different panel positions from tensile test and DMA measurements with standard deviation.

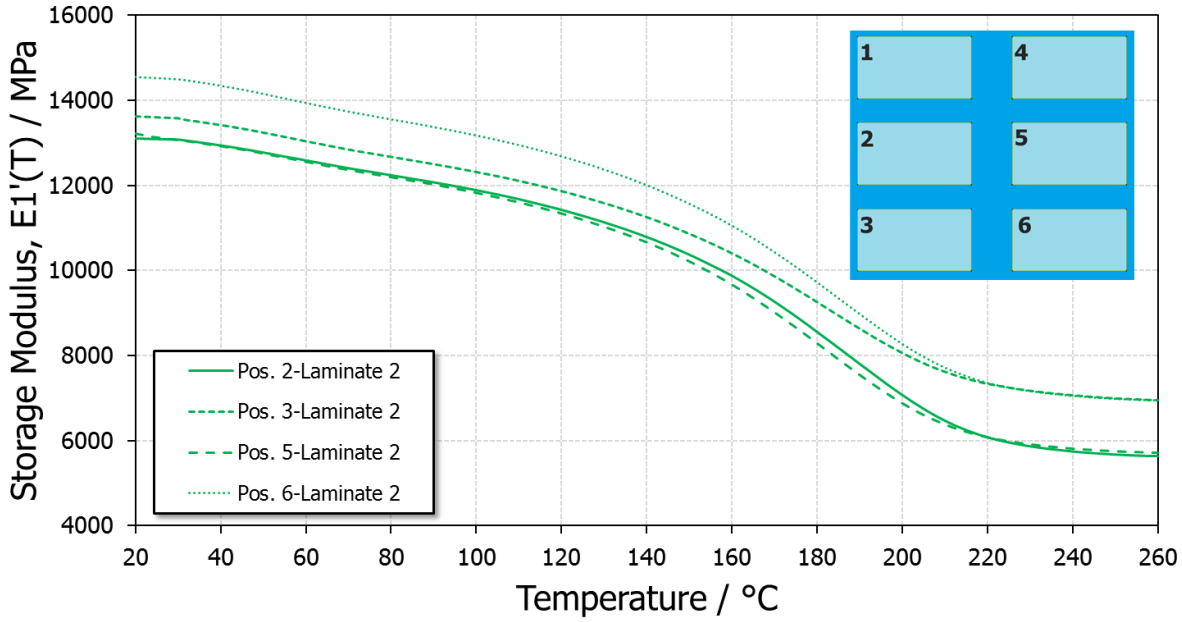

Figure 6-7: Mean modulus results from the temperature scanning by DMA, at different panel positions.

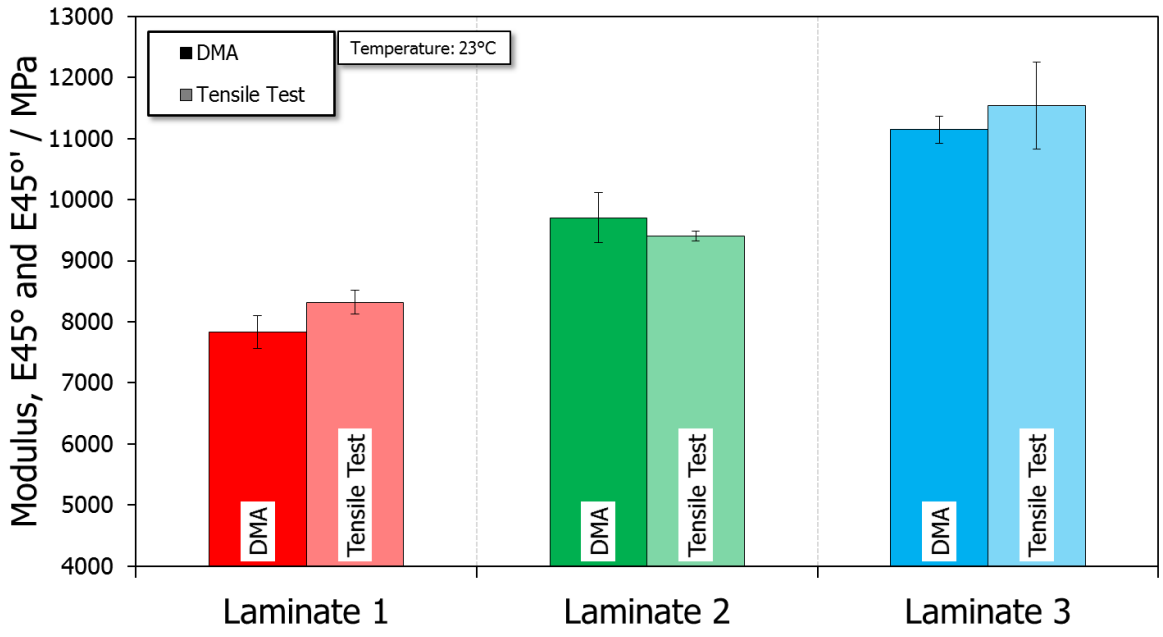

Figure 6-8: Mean Young's and storage modulus at room temperature with standard deviation

6.1.5 Evaluation of the Modulus at Elevated Temperatures

To investigate the Poisson's ratio and the Young's modulus of the materials listed in table 3-2, the monotonic tensile test implemented with DIC was conducted at room temperature and at elevated temperatures. The Poisson's ratio results were already discussed in chapter 6.1.3. Typical stress-strain curves from the tensile test of the investigated materials are shown in figure 6-9. All individual results, including fracture properties, are listed in the appendix table A-3. For the sake of completeness it should be mentioned that some specimens did not fracture in the shoulder area. A picture of various fractured specimens is shown in the appendix figure A-5. In general, the trend of a dropping slope by increasing measurement temperature can be observed for all tested materials (figure 6-9).

DMA measurements were also conducted for all the materials in order to investigate the differences between the Young's and storage modulus at elevated temperatures and to check the T_g. The individual results of the DMA measurements are shown in the appendix from figure A-6 to figure A-9.

Figure 6-10 represents the measured mean resin Young's and storage modulus in a logarithmic scale as a function of the temperature. The modulus outcome at room temperature of somewhere at around 4700 MPa is also with slight differences reported in the literature, for brittle epoxy resins (Ehrenstein et al., 2003, Tao, 2018). Slight differences between the two moduli can be observed before and after the T_g. During the glass transition, major differences are evident. They might be linked to the specimen thickness, the heating rate of the DMA and the heat distribution of the specimen inside the DMA. As described by Menard, 1999, with an increasing specimen size, the temperature field across the specimen cross-section varies and this can result in anomalies. It can be assumed that the heating rate of 2 K/min caused the differences; the inner section of the large resin specimen could not develop a fully homogenous temperature profile during the heating ramp. Apparently, the inner layer delays the glass transition to higher temperatures, with a corresponding higher modulus during this period. Ehrenstein et al., 2003, described the effects of the heating rate to the viscoelastic functions and pointed out that the chosen heating rate has a major impact.

Figure 6-11 and 6-12 represent the mean measured moduli of the laminates in 1 and 2 direction. In addition, the mean Young's modulus is represented with the standard deviation. During the glass transition of the laminate specimens, similar effects regarding the different moduli from the tensile test and DMA measurements were observed, as

mentioned above. The shift between the Young's and storage modulus of the laminates is relatively low compared to the shift between the moduli of the resin, during the glass transition. It seems plausible that the thinner specimen thickness supports a more homogenous temperature field development during the heating procedure. On the other hand, the presence of fibres limits the decrease of the storage modulus below the glass transition temperature. The fibre volume fraction is highly relevant for the level of the remaining storage modulus after T_g. The modulus does not decrease over decades during the glass transition, as observed in the resin without fibre reinforcement. This fact could lead to the assumption that the above mentioned effect is less dominant and cannot be observed anymore clearly.

When comparing the two figures 6-11 and 6-12, the first thing to be noticed is the different laminate moduli in direction 1 and 2. As described in chapter 3.3, the in-plane moduli of laminate 1 should differ in 1 and 2 directions due to the un-balanced woven fibre architecture. In contrast, laminate 2 and 3 also show differences. It is reasonable to assume that the laminate manufacturing process and measurement-dependent effects caused the differences. The second thing to be noticed is the dependency of the measured moduli on resin content; the moduli of laminates 1 and 2 are close to each other, while laminate 3 shows the highest moduli. The slightly higher modulus of laminate 2 could also be addressed to the slightly thicker two-layer build-up, the specimen conditioning and the general specimen warpage. With respect to the two-layer build-up: it can be assumed that with more stacked layers the pressure loss at the panel edges increases because of a higher gap. Thus, more resin is flowing during the press procedure towards the edges and the fibre volume fraction increases; the overall modulus response of a multi-layer build-up will be higher compared to a single-layer build-up. However, those influences can be seen as quite insignificant to the modulus. These experimental findings match well with the experimental findings from the TGA and hydrostatic weighing. In the studies of Fellner, 2012, similar results in 1 and 2 directions for similar materials used in PCB applications were observed.

However, the Young's modulus is slightly higher than the storage modulus before and after the T_g for all laminates in both directions, as can be seen figure 6-11 and figure 6-12. It is believed that, on the one hand, the evaluation method of the Young's modulus as secant modulus (DIN EN ISO 572-1, 2010) generally leads to a different modulus result compared to the sinusoidally defined dynamic modulus of the DMA measurement (the complex modulus can be split up to an elastic and a viscous response). Moreover, the compliance of

the DMA loading frame is lower compared to the loading frame compliance from the tensile test. The overall tensile test setup, presented in figure 4-5, can generally be seen as stiffer. Consequently, the stiffness of the loading frame and the clamps and the dimensions of the loading frame are much higher than those of the investigated specimens. It seems plausible that the influence of the tensile test compliance is negligible. By contrast, the loading frame of a DMA is usually much smaller and therefore effects attributed to the DMA instrument compliance could influence the resulting modulus. This could result in a lower storage modulus. Furthermore, effects attributed to specimen fixation, test parameters, specimen scaling, DMA loading mode, measurement data scattering and the test equipment utilized can cause the small differences. In the studies of Deng et al., 2007, similar instrument dependent compliance effects and conclusions were discussed.

In terms of composite testing, another factor could also make a contribution to the differences between the Young's and storage modulus. The applied loading range differs quite significantly between the tensile test and the DMA measurement, especially above the glass transition temperature. At the start of the DMA measurement, the applied force range was between 1 N and 9 N, by taking the static-offset into account. After the T_g, the resulting total force is usually somewhere in the range of 0.5 N up to maximum 4 N, depending on the specimen. It may be reasonable to suppose that the fibre bundles could not have been fully stretched/loaded by the tensile force during the DMA measurement after the T_g. Eventually, the waviness of the fibre architecture and the softened resin could have caused this not fully developed loading condition of the fibre bundles. On the other hand, the applied force range during the tensile test starts somewhere around 2 N and reaches its maximum at around 55 N, for all temperatures. Therefore, the consequence is that during the tensile test procedure the fibre bundles are fully stretched in the loading direction. The conclusion out of this assumption could be that the stiffer fibres affecting the Young's modulus after the T_g also noticeable.

Table 6-3 represents the mean T_g values with standard deviation from the evaluation of the DMA measurements. According to the material supplier, the T_g obtained by DMA should be at 200°C. The measured glass transition temperatures between 175°C and nearly 200°C are in similar ranges. However, a direct comparison is not appropriate because the manufacturer did not provide information with respect to the used DMA deformation mode, T_g evaluation technique and the specimen conditioning. As can be derived from table 6-3, a discrepancy of the measured T_g between the resin and the laminates has been observed in the DMA studies. In addition, the laminates 1 and 3 tend to a significantly lower T_g in

direction 1. This interesting finding was unexpected, because a difference of more than 10°C are observed in the individual directions.

With respect to the cause of the T_g direction dependency of the laminates 1 and 3, two possible explanations exist for this unusual behaviour. For one thing, laminate 2 did not show a varying T_g in different directions. The same test parameters were applied for all examined laminates. Therefore, one of the main differences from a sample point of view was the conditioning; laminate 2 was pre-cured in the oven above T_g. This fact could indicate that the laminates 1 and 3 show post-curing effects during the DMA measurement. Nevertheless, this reason can be seen as highly unusual because it does not fully explain the direction dependency, but it should not stay unconsidered. Additionally executed differential scanning calorimetry (DSC) measurements could not fully exclude curing effects. For another thing, the already discussed effects regarding the influence of the loading range of the DMA apparatus may have caused these anomalies. Upon a closer look at the figure A-8 in the appendix, the modulus slightly increases after the T_g in direction 1 of the laminates 1 and 3. This effect is more dominant for laminate 3. The modulus upward kink during the measurement directly above the T_g could be caused by a reorientation/retightening of the fibre bundles. In addition, another assumption could be the appearance of slipping effects during or above the glass transition, attributed to the gained mobility of the thermosetting matrix of the very thin specimens. Nevertheless, also this hypothetical cause can be seen as highly unusual because the contribution of these effects to the loss factor should be non-existent. Unfortunately, the cause of the observed very uncommon direction dependency of the T_g cannot be clearly identified at this point.

However, in future work post-cured laminate core specimens could be also measured as reference by DMA, to exclude effects attributed to the unusual direction-dependent behaviour based on the curing degree to the T_g. In addition, it is recommended to use also a higher static offset of 300% in pre-trails with an additional, marginally higher torque moment of the fixation screws, to detect possible loading and clamping phenomena beforehand. It should be also mentioned that the post-curing conditioning of laminate 2 could have caused a slight T_g shift compared to the other two laminates, but under these circumstances a direct comparison to results of laminate 1 and 3 could lead to wrong conclusions. The glass transition temperatures at the four positions of laminate 2 in direction 1 were in a good agreement. Only position 3 shows a trend to a lower glass transition temperature, but this can be seen as minor when taking the other mean results with their standard deviation at the other panel positions into account.

It can be assumed that the differences in the T_g between the resin and the laminate materials listed in table 6-3 may have caused a different curing degree. Even after 8 hours of conditioning a thermosetting material, usually differences in the peak temperature of the tan(δ) can be observed due to the sensitivity of the DMA measurement to transitions (Menard, 1999). To observe this slight mismatch, a longer conditioning time is recommended in future work for both resin and laminate specimens. On the other hand, Ehrenstein et al., 2003, pointed out that a thermal conductivity gradient between a resin and fibres can influence the temperature development of the specimen inside the DMA oven. This could result in different glass transition temperatures between the resin and laminates due to differences in the thermal inertia during the heating inside the DMA oven. Hence, there might be two possible effects attributed to the thermal conductivity: first, the thermal conductivity of the resin is higher than that of the laminates. This assumption would result in a lower T_g of the resin system because the thermal inertia of the resin would be lower compared to the laminate during the heating segment. Second, if the thermal conductivity of the resin were lower, the T_g of the resin would be higher because of a hypothetically higher thermal inertia of the resin during the heating phase. Datasheets regarding thermal properties of the investigated resin system are not available. However, without knowing the exact thermal conductivity of the resin and the individual laminate materials, assumptions about this effect are not reasonable. Effects regarding the curing conditioning should be investigated first.

Nevertheless, the modulus results obtained by the tensile test and DMA measurements were quite reproducible for the resin and laminate specimens. Depending on the measurement method used, the modulus outcome varies slightly. All standard deviations of the mean results can be seen as quite low, except the individual results of the DMA from laminate 2 in direction 1 (discussed in the previous chapter). This fact validates also a stable and reliable specimen preparation approach.

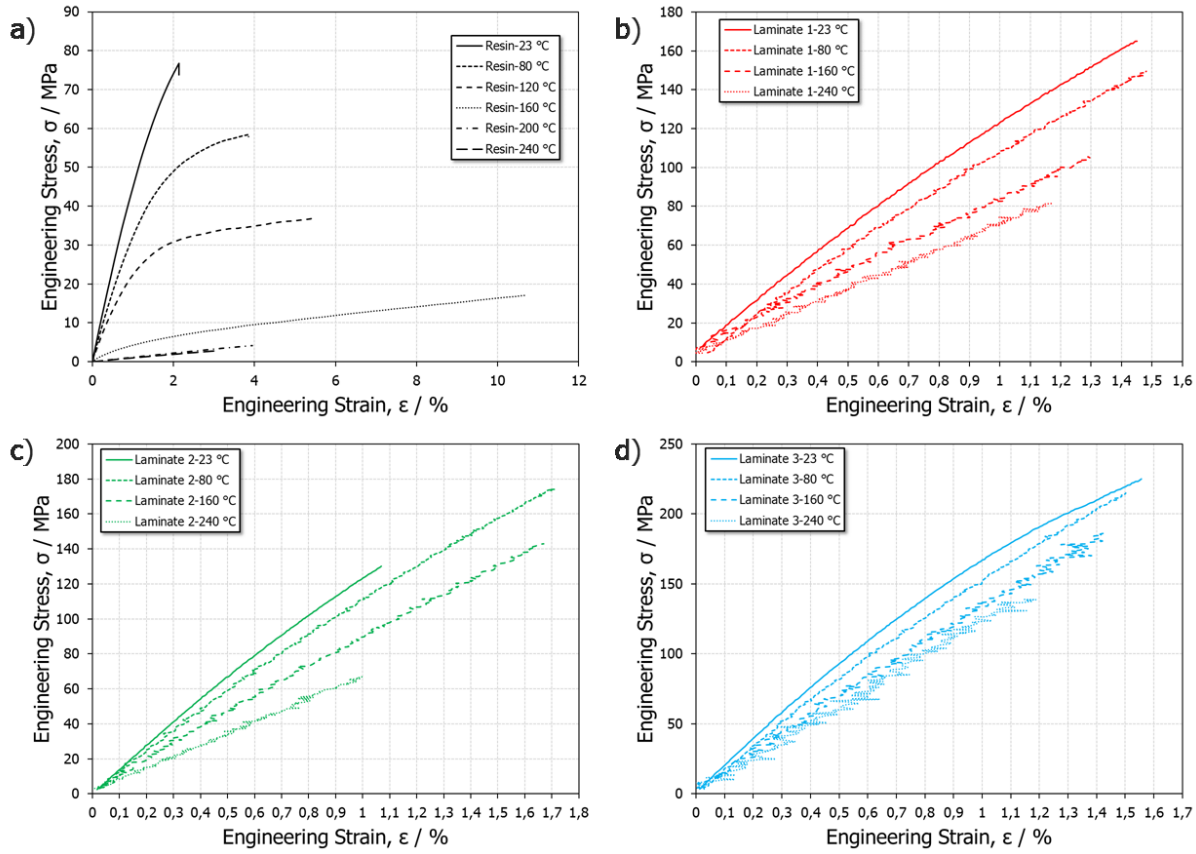

Figure 6-9: Typical stress-strain curves of the resin (a), laminate 1 (b), laminate 2 (c) and laminate 3 (d).

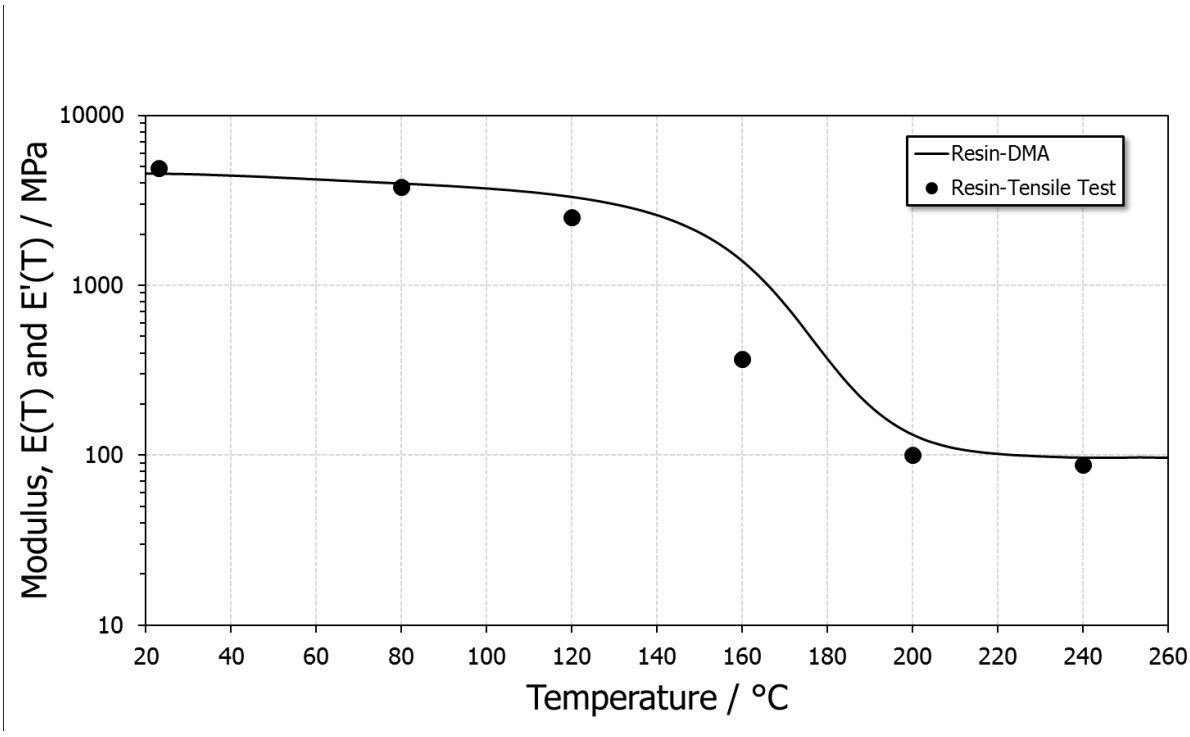

Figure 6-10: Mean resin Young's and storage modulus over the temperature.

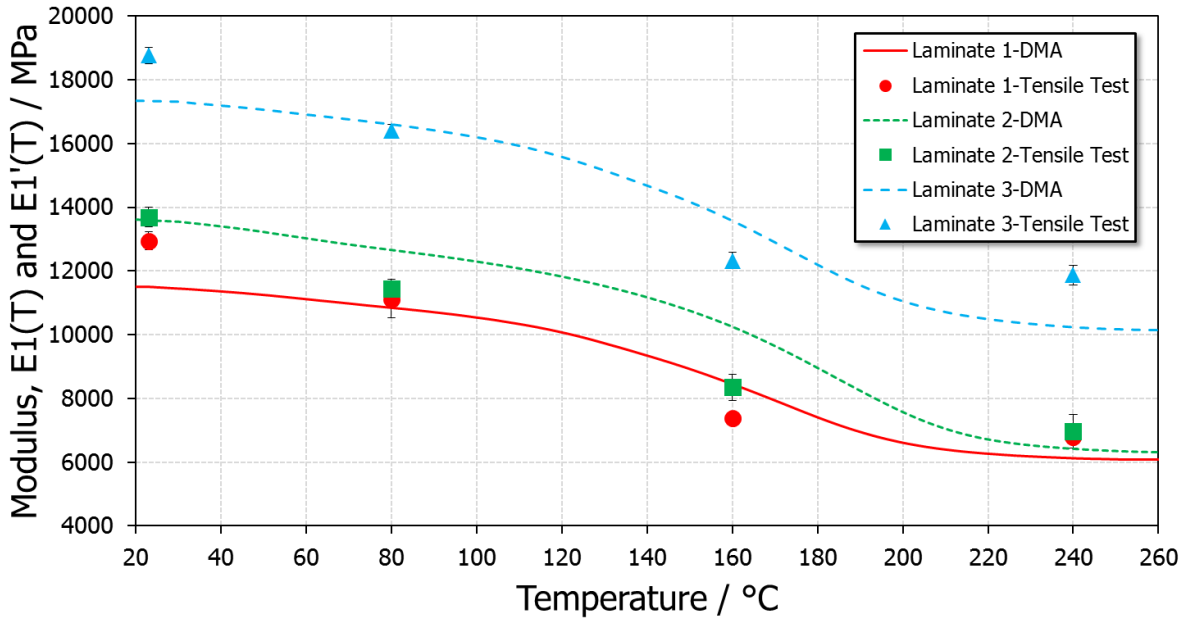

Figure 6-11: Mean Young's and storage modulus over the temperature in direction 1 of all laminates.

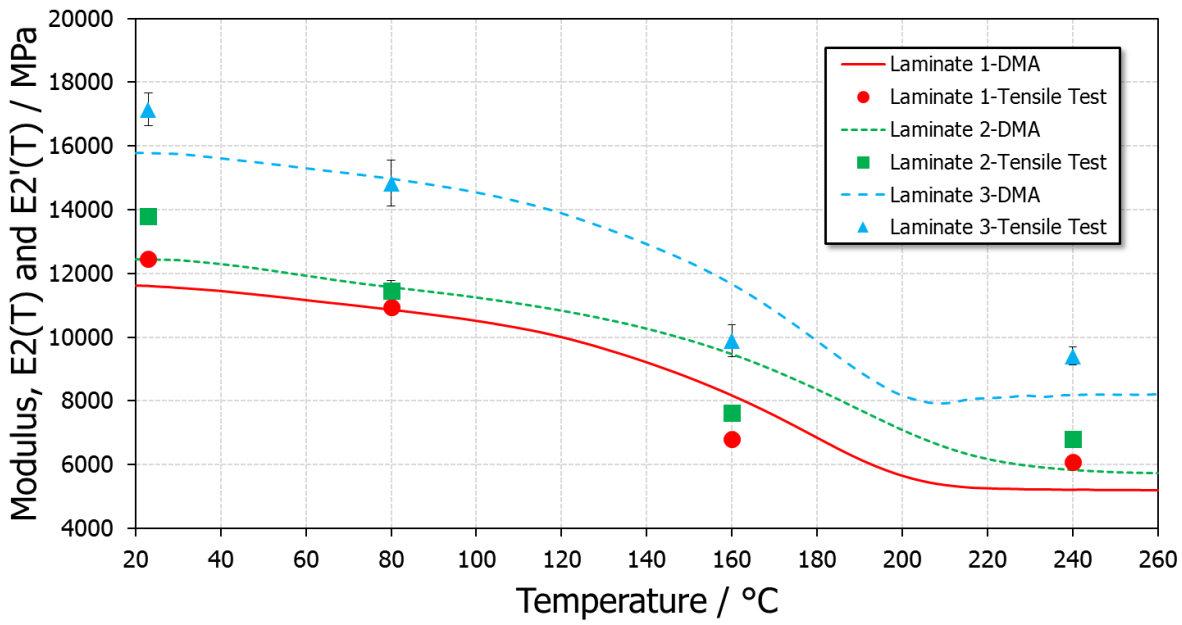

Figure 6-12: Mean Young's and storage modulus over the temperature in direction 2 of all laminates.

Table 6-3: Mean T_g values obtained from the DMA measurements evaluated as peak temperature of the loss factor tan(δ).

Material	Direction	Position	Mean $T_{g_tan(\delta)}$	SD of Mean Results
[-]	[-]	[-]	[°C]	[°C]
Resin	-	-	180,7	2,1
Laminate 1	1	-	181,1	2,0
	2	-	190,2	1,2
	45°	-	194,4	0,4
Laminate 2	1	Pos. A2	194,0	4,3
	1	Pos. A3	190,0	1,4
	1	Pos. A5	191,8	1,0
	1	Pos. A6	193,9	2,9
	2	-	195,2	1,7
	45°	-	195,0	1,1
Laminate 3	1	-	175,9	2,1
	2	-	189,1	1,7
	45°	-	196,1	1,0

6.1.6 Evaluation of the Cross Sectioning

The individual results and mean values with the standard deviation of the cross sectioning provided by the physics laboratory of AT&S HTB are listed in the appendix table A-1 and table A-2. Figure 6-13 represents a cross section with yarn width and height definition, respectively.

As shown in figure 6-13, the limits to evaluate the yarn width and height were defined by the laboratory technician manually. The yarn width and height of the three investigated laminates differ in the 1 and 2 directions, as represented in the appendix table A-1 and table A-2. These differences could be explained by a different press and manufacturing procedure, different resin contents and different woven fibre architectures of the investigated laminates. However, the observed mean aspect ratios were used in the micromechanical study.

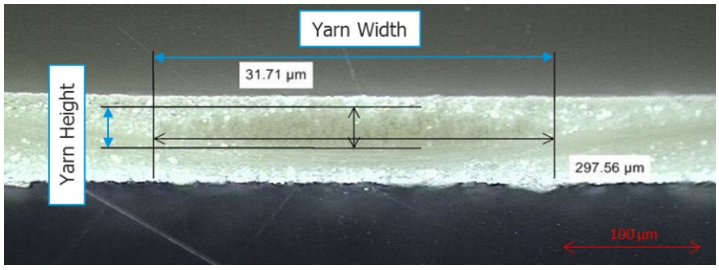

Figure 6-13: Laminate cross sectioning with yarn width and height definition.

6.2 Numerical Results

6.2.1 Evaluation of the General RUC Response and the Influence of the Yarn Aspect Ratio

Table 6-4 lists the calculated engineering constants of the implemented models with different yarn aspect ratios. In order to get a first indicator of the general RUC response and the influence of different yarn aspect ratios, only PBCs were applied. Figure 6-14 shows a schematic RUC response by applying different loading situations (automatically applied PBCs by the Abaqus® Micromechanics Plugin) in order to determine the engineering constants.

The first thing to notice is the influence of the resin content on the modulus in all three directions. The RUCs Lam 1_v1 and Lam 2_v1 predict a nearly similar modulus with a corresponding similar resin content. Meanwhile, the overall stiffness response of the RUC Lam 3_v1 is higher, due to a higher fibre volume fraction. The effect is more dominant to the in-plane moduli. Comparing the RUCs Lam 1_v2, Lam 2_v2 and Lam 3_v2, the same trend can be observed. The general impact of the volume content of two-phase systems in simple micromechanical assumptions can be addressed by the "Rule of Mixture" (Reuss, 1929, Voigt, 1889).

Differences between the aspect ratio of 7 and the measured aspect ratios can be clearly identified in table 6-4. An indication of the influence of the measured yarn aspect ratio can be seen by comparing the in-plane modulus (E1 and E2) of the RUC Lam 1_v2, Lam 2_v2 and Lam 3_v2: the highest in-plane modulus of each RUC is linked to the biggest yarn aspect ratio in the corresponding direction. The generated cross-sectional virtual aspect ratio in Abaqus®/CAE of the voxel yarn does not geometrically correspond to the measured aspect ratios, which are the aspect ratio 25.7 and 28.1, respectively. Meanwhile, the cross-sectional virtual aspect ratios in Abaqus®/CAE of the voxel yarns below 15 are, with slight differences, comparable to the measured aspect ratios by cross sectioning. Hence, the high

aspect ratios cannot be correctly represented by the pre-defined voxel count of 50x50x50 in the virtual environment. It appears that the fibre volume fraction was overestimated in the direction where the aspect ratio cannot be represented in a correct way. This assumption correlates with similar reported effects by Crookston et al., 2007.

In addition, the RUC Lam1_v1 shows different in-plane moduli with similar aspect ratios. Due to the non-symmetrical woven fibre architecture of the 1037 fabric, the fibre volume fraction differs in 1 and 2 direction. This fact results in different in-plane moduli.

In the following chapters, the RUCs with the measured aspect ratio will not be represented any more, because of the unreliable results observed.

Table 6-4: Numerically calculated engineering constants of different yarn aspect ratios by PBCs. The (1 / 2) entries are the parameters in 1 and 2 direction respectively.

RUC	[-]	**Lam 1_v1**	**Lam 1_v2**	**Lam 2_v1**	**Lam 2_v2**	**Lam 3_v1**	**Lam 3_v2**
Aspect Ratio (1 / 2)	[-]	7 / 7	25,7 / 7,5	7 / 7	9,6 / 28,1	7 / 7	14,9 / 9,9
Resin Content	[%]	66,3		66,1		60,1	
E1	[MPa]	14504	16609	14739	14857	16470	17792
E2	[MPa]	14721	14683	14739	16739	16470	16980
E3	[MPa]	8082	7852	8270	7868	9104	8574
v12	[-]	0,191	0,220	0,193	0,196	0,186	0,201
v13	[-]	0,335	0,333	0,327	0,338	0,317	0,327
v23	[-]	0,333	0,341	0,327	0,331	0,317	0,328
G12	[MPa]	3654	4688	3621	4729	3905	4833
G13	[MPa]	2479	2456	2489	2377	2674	2598
G23	[MPa]	2482	2392	2489	2434	2674	2560

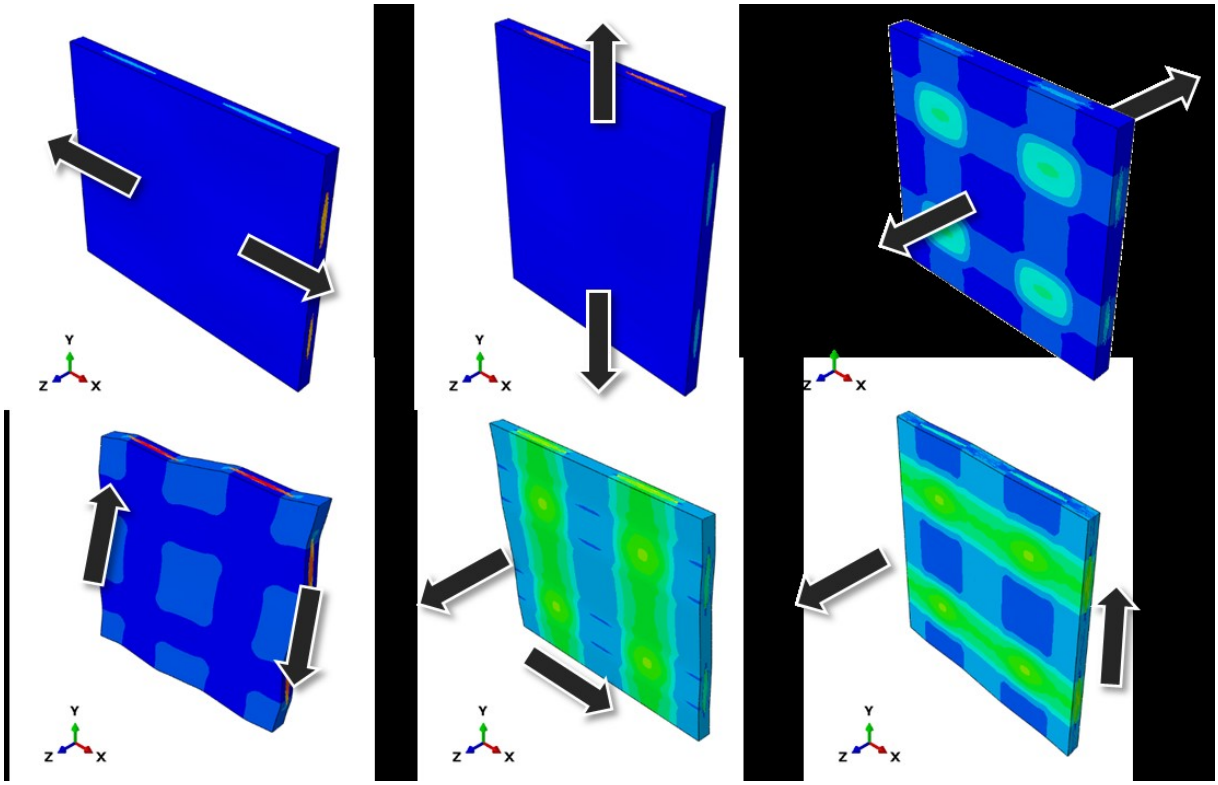

Figure 6-14: Schematic representation of the RUC loading situations needed to evaluate the 9 orthotropic engineering constants by PBCs.

6.2.2 Evaluation of the Applied Boundary Condition

As already outlined in chapter 5.2, the basic differences between the RUC response of PBCs and PSBCs were also investigated. Figure 6-15 shows the deformation plot of the RUC responses by applying manually a far-field strain load history in direction 1 of 1% strain. The first thing to be noticed is the restricted out of plane movement of the PBCs, shown in figure 6-15a. The RUC surface did not deform freely in the out-of-plane direction 3. On the other hand, the PSBCs allowed a free deformation of the RUC surface in the 12 plane, presented in figure 6-15b.

Table 6-5 lists the predicted engineering constants calculated by different BCs. Out-of-plane moduli were not calculated by the PSBCs, because a far-field load would have to have been applied in direction 3. This would result in free surfaces of the 13 and 23 planes. The corresponding modulus response cannot be seen as reasonable, because these surfaces should be restricted.

Depending on the applied BC, the results differ moderately. As shown in table 6-5, the moduli of the PSBCs tend to be slightly lower. The Poisson's ratios calculated by the PSBCs are a bit higher compared to the PBCs. These results can be explained on the basis of the

varying mathematical formulation of the BCs. The PBCs applies the vectors of periodicity to every node in the model in all three directions. Meanwhile, the PSBDs applies the vectors of periodicity only to the in-plane components (direction 1 and 2) of the nodes. This formulation leads to a free surface like state, when applying the PSBCs correctly (Dassault Systèmes, 2017). In the studies of Gigliotti and Pinho, 2015, a more detailed mathematical description of the PSBCs formulation is represented in their appendix.

A PBCs formulation is represented in chapter 2.6.2. The free surface affects the stress and strain situation inside the RUC significantly. Figure 6-16 compares the stress and strain component from the averaged concentration components in direction 1 of the RUC Lam 3_v1 from both BCs over the calculation time. The resulting modulus response is also plotted. It is highly possible that the free surface of the PSBCs lowers the averaged stress and strain situation inside the RUC. Hence, the in-plane moduli will respond lower with an additional lower stress to strain ratio. The examined PSBCs results show also that the calculated Poisson's ratios will respond higher, compared to the PBCs.

However, the effect of the resin content and the mentioned not-balanced woven fibre architecture of laminate 1 is also noticeable, by both BCs. It is also interesting, that the out-of-plane Poisson's ratios (v13 and v23) calculated by the PSBCs are somewhere at around 0.05 higher, compared to the PBCs results. The reliability of the results is discussed in the verification chapter 6.3.

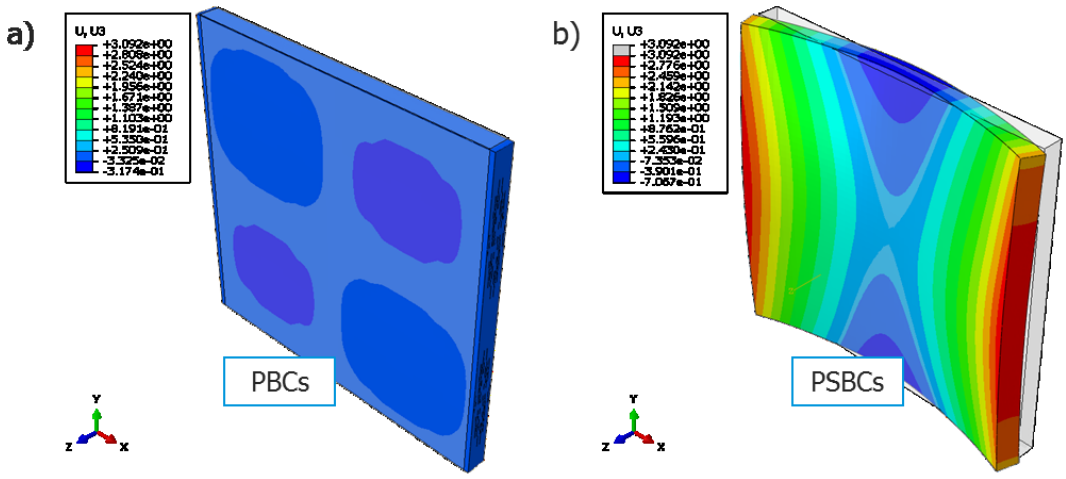

Figure 6-15: RUC responses by applying a far-field strain load in direction 1 with boundary conditions of PBCs (a) and PSBCs (b).

Table 6-5: Calculated engineering constants obtained from the RUC response by the PBCs and PSBCs.

RUC	[-]	**Lam 1_v1**	**Lam 1_v1**	**Lam 2_v1**	**Lam 2_v1**	**Lam 3_v1**	**Lam 3_v1**
Aspect Ratio (1 / 2)	[-]	7 / 7		7 / 7		7 / 7	
Resin Content	[%]	66,3		66,1		60,1	
BC	[-]	PBCs	PSBCs	PBCs	PSBCs	PBCs	PSBCs
E1	[MPa]	14504	13394	14739	13567	16470	15071
E2	[MPa]	14721	13644	14739	13567	16470	15071
E3	[MPa]	8082	-	8270	-	9104	-
v12	[-]	0,191	0,201	0,193	0,201	0,186	0,195
v13	[-]	0,335	0,367	0,327	0,367	0,317	0,365
v23	[-]	0,333	0,365	0,327	0,367	0,317	0,365

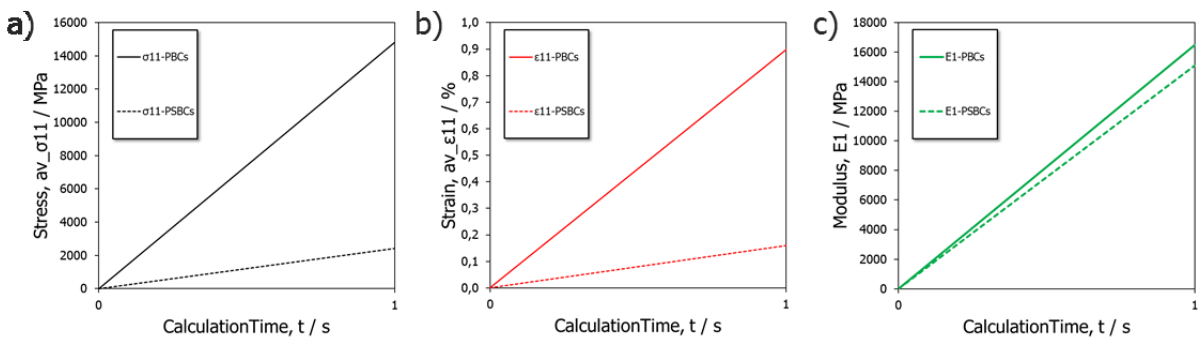

Figure 6-16: Averaged RUC stress (a) and strain (b) components over calculation time in direction 1 of RUC Lam 3_v1, with calculated modulus (c).

6.3 Verification of Numerical Results

Figure 6-17, figure 6-18 and figure 6-19 represent the in-plane Poisson's ratio, the modulus in direction 1 and 2 from the experimental and numerical evaluation at room temperature, respectively. The experimental results are depicted with their standard deviation.

All in-plane Poisson's ratios from the numerical part are slightly overestimated compared to the experimental findings, as can be seen in figure 6-17. Only the numerical results from Laminate 2 (RUC: Lam 2_v1) can be seen somewhere close to the experimental observations, by taking the standard deviation of the tensile test into account. Another interesting observation is that obviously the numerical in-plane Poisson's ratio seems not to

be significant depending on the fibre volume fraction and the investigated woven fibre architecture. This indication supports the assumptions established in chapter 6.1.3.

For both measured in-plane moduli, shown in figure 6-18 and figure 6-19 the numerical predictions are in quite similar ranges. Trends regarding the resin content are also noticeably similar. The PSBCs calculate remarkably comparable results for laminate 1 and 2 in both directions. On the other hand, the PBCs slightly overestimates the experimental moduli. By contrast, the PBC predicts the moduli of laminate 3 very close to the experimental findings. Unfortunately, the PSBCs is not able predict the modulus of laminate 3 as precisely as the PBCs.

However, the established simple numerical implementation of the RUCs can be seen as quite reliable. Both investigated BCs are able to predict the experimental results at room temperature accurately. Additionally, the numerical modulus results are also highly driven by the resin content. There is evidence to indicate that the implemented "Two-Step" procedure, presented in chapter 4.2, predicted the resin content quite accurately.

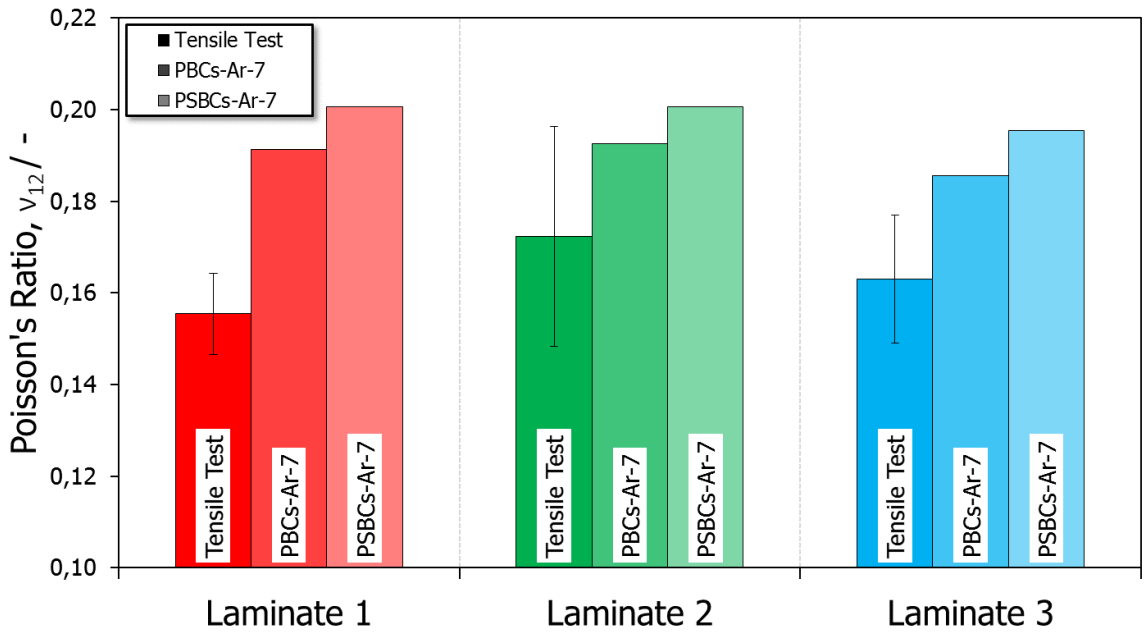

Figure 6-17: In-plane Poisson's ratio obtained from the experimental and numerical study.

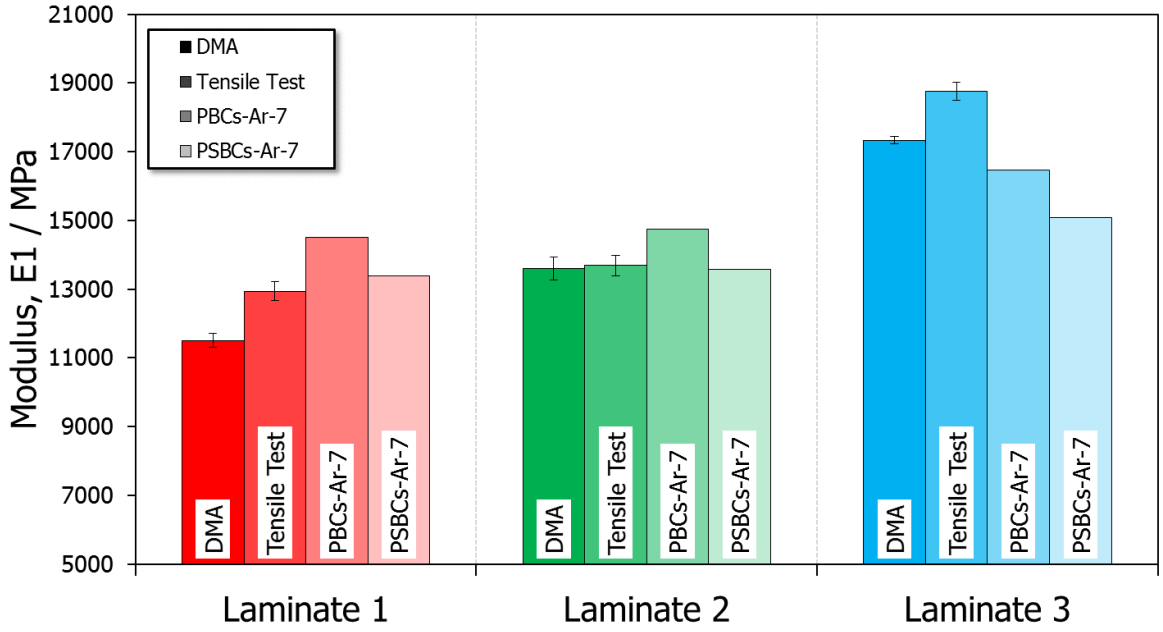

Figure 6-18: Modulus in direction 1, obtained from the experimental and numerical study.

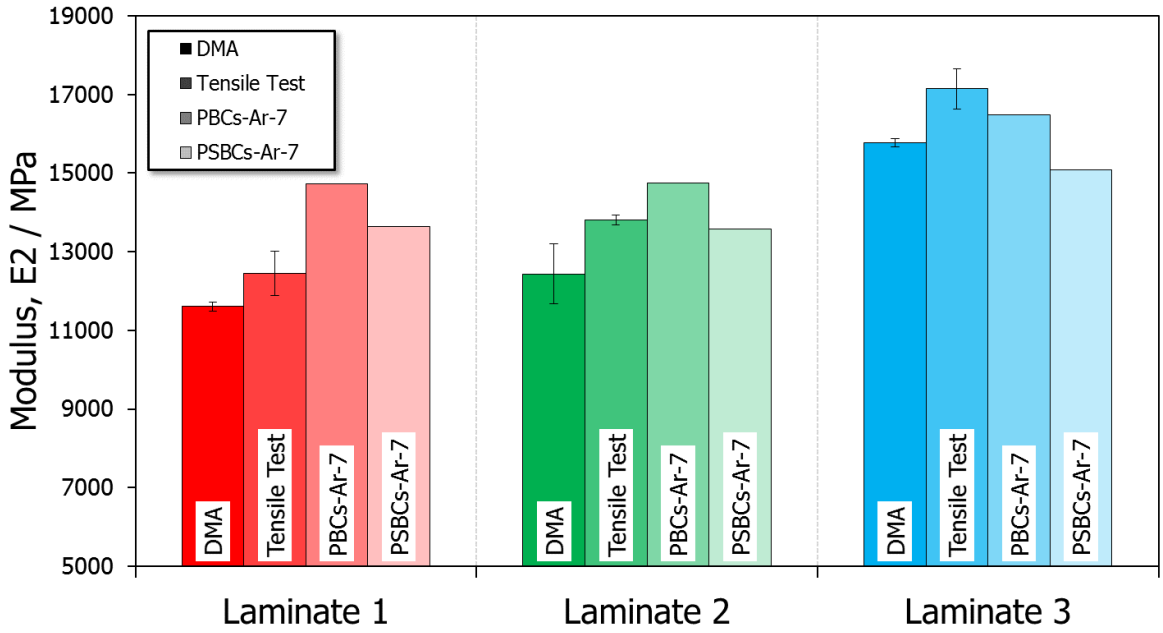

Figure 6-19: Modulus in direction 2, obtained from the experimental and numerical study.

6.4 Suggestions for the Final Material Model

As outlined in the introduction, for implementing a fully orthotropic material model usually a combination of experimental and numerical results has to be utilized. Table 6-6 represents

a suggestion for the implementation of the material parameters of the investigated materials for the FEA in order to perform a PCB simulation at room temperature.

The in-plane moduli were taken from the DMA measurements, because a tensile testing device was not available in AT&S HTB. On the other hand, only minor differences to the tensile test results were observed in the experimental part of this study. The in-plane Poisson's ratio was taken from the tensile tests. The out-of-plane modulus E3, the out-of-plane Poisson's ratios (v13 and v23) and the shear moduli (G12, G13 and G23) were taken from micromechanics with PBCs. On the other hand, the PSBCs offers also an attractive and reliable way of predicting the out-of-plane properties. However, more investigations of the PSBCs have to be carried out in future work.

In order to create a fully temperature-dependent orthotropic material model, tensile test and DMA measurement data should be available for the in-plane properties E1(T), E2(T) and v12(T). The corresponding temperature-dependent shear modulus G12(T) could be calculated by using a simple analytical approach and an additionally measured temperature dependent modulus in 45° direction (E45°(T)). Therefore, an equation shown in Tuttle, 2004, with some slight modifications could be used:

$$G12(T)=\frac{E1(T)\cdot E2(T)\cdot E45°(T)}{4\cdot E1(T)\cdot E2(T)-E45°(T)\cdot(E2(T)-2\cdot v12(T)\cdot E2(T)+E1(T))} \tag{6.2}$$

Nevertheless, the properties G13(T), G23(T), v13(T), v23 and E3(T) are missing. In order to determine these properties, the obtained temperature dependent modulus and Poisson's ratio of the resin could be utilized in a micromechanical simulation at elevated temperatures. The same procedure represented in figure 5-3 could be utilized. In terms of the resin material, all material parameters for the temperature dependent material model are available.

Table 6-6: Suggestions for the final material models of the investigated materials at room temperature.

Material	**E1**	**E2**	**E3**	**v12**	**v13**	**v23**	**G12**	**G13**	**G23**
	[MPa]	[MPa]	[MPa]	[-]	[-]	[-]	[MPa]	[MPa]	[MPa]
Resin	4560			0,323			1723		
Laminate 1	11506	11604	8082	0,155	0,335	0,333	3654	2479	2482
Laminate 2	13598	12429	8270	0,172	0,327	0,327	3621	2489	2489
Laminate 3	17337	15776	9104	0,163	0,317	0,317	3905	2674	2674

7 SUMMERY AND OUTLOOK

The mechanical characterization and micromechanical modelling of woven glass fibre reinforced laminates, for PCB applications have been performed systematically. Three fully orthotropic material models for the implementation into the finite element analysis were generated by using a combination of experimental and numerical state of the art methodologies.

Within the scope of this master thesis, first the theoretical background of the used methods was explained. In the practical part, three different woven fibreglass dielectric PCB materials from the same material family with the corresponding resin matrix were chosen. In order to create reproducible and reliable results, an automated specimen preparation approach was designed. The resin tensile test specimens were prepared at AT&S Hinterberg with a PCB production routing machine. The laminate specimens were prepared at AT&S Shanghai in the PCB production process. For this a card layout design placed in six different panel positions with closely positioned tensile test and DMA test sample strips was developed. This procedure enabled the lamination of a prepreg panel with a PCB production press. Utilizing the PCB production for the specimen preparation allowed the production of high quality specimens for the experimental studies and a fast specimen manufacturing procedure.

In the experimental studies, the introduced "Two-Step" procedure for the determination of the laminate resin content by thermogravimetry provided reasonable and useful input parameters for the numerical studies. These experimental findings were in good agreement with the hydrostatic weighing measurements. All tensile test and DMA results with respect to the measured moduli were in a good agreement over the measured temperature range. Small differences were addressed to the compliance of the used test equipment and the heating ramp during the DMA measurement. The obtained in-plane Poisson's ratios of the laminate specimens at room temperature were reproducible and in the expected ranges. Although, at elevated temperatures the measurement outcome can be seen as not applicable for a finite element analysis, due to the high degree of variations. It is highly possible that effects attributed to the thin specimens and the challenging execution of the tests at the elevated temperatures caused the significant and unpredictable data scattering. On the other hand, the resin specimens provided reasonable Poisson's ratio results.

Regarding the specimen preparation approach, all moduli results showed only minor data scattering. The in-house laminated prepreg specimens showed a position-dependency of the modulus due to the press procedure. Nevertheless, the position dependency was assessed as acceptable. Overall, the developed automated specimen preparation methodology represents a new approach for the specimen preparation at AT&S with the capability to create reliable and reproducible results also in future material testing applications.

In future work it is recommended to study the laminate resin content by thermogravimetric analysis by additionally taking the inorganic content of the resin itself into account, in order to create powerful numerical input data for a micromechanical approach. In addition, the tensile test setup for thin laminate specimens must be modified to create a useful Poisson's ratio outcome at elevated temperatures. Hence, a possible direction might be the utilisation of a geometrically down-scaled tensile test set-up with an additional focus on a reliable and centric specimen fixation. Using grips that are more appropriate for the thin and small specimens could also enhance the quality of the measurement outcome.

In the numerical studies, three simple periodically repeating unit cells based on the examined laminates and measurement data were implemented into a finite element environment. The implementation of the cross-sectional view of the fibre bundles overestimated the experimental results noticeably due to an insufficient mesh resolution. However, both of the investigated periodic boundary conditions predicted the experimental data well, even without taking the exact geometry of the fibre bundles into account. Especially the periodic shell boundary condition offers a new exciting possibility to predict the material properties of thin laminate structures. The next stage should be enhancing the micromechanical models, reinvestigating the effects attributed to the fibre bundle geometry and executing numerical studies at elevated temperatures.

It can be concluded that micromechanical approaches have, in general, a high potential to predict the orthotropic engineering constants in a reliable way. To achieve these results, high quality experimental input data can be seen as one of the key parameters. It should be feasible to create fully orthotropic temperature dependent material models in the future based on resin and glass properties by applying micromechanical approaches.

8 LITERATURE

Amber J.W. McClung, Gyaneshwar P. Tandon,·Jeffery W. Baur (2012). Strain rate- and temperature-dependent tensile properties of an epoxy-based, thermosetting, shape memory polymer (Veriflex-E). Mechanics of Time-Dependent Materials **16**, 205.

AT&S (2017). Training Document – Orthotropic Material Models. Internal

Böhm, H., J. (2017): A short introduction to basic aspects of continuum micromechanics. Institute of Lightweight Design and Structural Biomechanics (ILSB)Vienna University of Technology

Callister, D., W., Rethwisch, D., G. (2013): Materials Science and Engineering: An Introduction. 9th Edition: Wiley

Cerbu, C., Cutu, I., Constantinescu, D., M., Constantin, M., (2011). Aspects Concerning the Transversal Contraction in the Case of Some Composite Materials Reinforced with Glass Fabric. Materiale Plastice **48**, 341

Coombs, C. F. (2001). Printed Circuit Handbook (5th ed.). The McGraw-Hill Companies.

Crookston, J., J., Ruijter, W., Long, A., C., Warrior, N., A., Jones, I., A. (2007). A comparison of mechanical property prediction techniques using conformal tetrahedral and voxel-based finite element meshes for textile composite unit cells. Finite element modelling of textiles and textile composites, St-Petersburg

Deng, S., Houb, M. and Yea, L. (2007). Temperature-dependent elastic moduli of epoxies measured by DMA and their correlations to mechanical testing data. Polymer Testing **26**, 803

Department of Aeronautical and Astronautical Engineering (2004). Homepage of Massachusetts Institute of Technology (USA), http://web.mit.edu/16.810/www/16.810_L4_CAE.pdf, state: 08.02.2018

Dassault Systèmes (November 2017). Micromechanics Plugin for Abaqus/CAE. Version 1.11

DIN 51006 (Oktober 1990). Thermische Analyse (TA), Thermogravimetrie (TG).

DIN EN ISO 572-1 (2010). Kunststoffe – Bestimmung der Zugeigenschaften – Teil 1: Allgemeine Grundsätze (Normentwurf).

DIN EN ISO 6721-1 (Dezember 1996). Bestimmung dynamisch-mechanischer Eigenschaften – allgemeine Grundlagen.

DIN EN ISO 11358 (November 1997). Thermogravimetrie von Polymeren.

Dominighaus, H., Elsner, P., Eyerer, P., Hirth T. (2008). Kunststoffe: Eigenschaften und Anwendungen. 7. Auflage. Berlin: Springer Verlag

Ehrenstein, Gottfried W. (2006). Faserverbund-Kunststoffe, Werkstoffe – Verarbeitung – Eigenschaften. 2. Aufl. München: Hanser.

Ehrenstein, Gottfried W., Riedel, Gabriela, Trawiel, Pia (2003). Praxis der thermischen Analyse von Kunststoffen. 2. Aufl. München: Hanser.

Fahrenholz, H. (October 2016). DIN EN ISO 527, Kunststoffe: Bestimmung der Zugeigenschaften. 27. testXpo - Internationale Fachmesse für Prüftechnik. G.

Fellner, K. (2012). Simulation des "Single Via Thermal Cycle Test" -Modellerstellung und Bestimmung der Materialeingangsparameter. Master Thesis, Institute of Material Science and Testing of Polymers, Montanuniversität Leoben, A.

Fuchs, P., F. (2012). Characterization and Simulation of the Deformation and Failure Behavior of Printed Circuit Boards (PCB). PhD thesis, Institute of Material Science and Testing of Polymers, Montanuniversität Leoben, A

Foreman, J., Sauerbrunn, S., Marcozzi, C., (2006). Exploring the sensitivity of thermal analysis techniques to the glass transition. TA Instruments, Inc.. USA.

Frewein, M. (March 2017). Modelling and characterization of the anisotropic thermal expansion of woven glass fibre reinforced laminates. Bachelor thesis, Institute of Material Science and Testing of Polymers, Montanuniversität Leoben, A.

Gigliotti, L. and Pinho, S., T. (2015). Exploiting symmetries in solid-to-shell homogenization, with application to periodic pin-reinforced sandwich structures. Composite Structures **132**, 995

Grellmann, W., Seidler, S. (2007). Kunstsoffprüfung. 2.Auf. München: Hanser.

Gschwandl, M., Fuchs, P., F. Fellner, K., Antretter, T., Krivec, T. and Tao, Q. (2016) Finite Element Analysis of Arbitrarily Complex Electronic Devices. 18th Electronics Packaging Technology Conference (EPTC). Singapore

Guttmann, P. (November 2009). Dynamisch mechanische Analyse von Epoxidharzen. Master Thesis, Institute of Material Science and Testing of Polymers, Montanuniversität Leoben, A.

Golestanian, H. and Sherif, E. (1996). Cure Dependent Lamina Stiffness Matrices of Resin Transfer Molded Composite Parts with Woven Fiber Mats. Journal of Composite Materials **31**, 2402

IPC-4412A Amendment 1 (March 2008): Specification for Finished Fabric Woven from "E" Glass for Printed Boards.

IPC-TM-650 2.3.13 (1994). Resin Content of Prepreg, by Burn-off. USA

IPC-TM-650 2.4.24C (1994). Glass transition temperature and z-axis thermal expansion by TMA. USA

Jawitz, Martin W., Jawitz, Michael J. (2007). Materials for rigid and flexible printed wiring boards. Boca Raton, Fla: CRC/Taylor & Francis (Electrical and computer engineering, 131).

Jerabek, M., Zoltan, M., Lang, R.W (2010). Strain determination of polymeric materials using Strain determination of polymeric materials using digital image correlation. Polymer Testing **29**, 407.

Kaw, A., K. (2006): Mechanics of composite materials. 2. Aufl. Boca Raton: CRC Taylor & Francis. Mechanical engineering series, 29.

Menard, P. (1999). Dynamic Mechanical Analysis – A Practical Introduction. CRC Press. USA

Mettler Toledo (2005). STARe System DMA/SDTA861e Operating Instructions

Mguil-Touchal, S., Morestin, F., Brunet, M. (1997). Various Experimental Applications of Digital Image Correlation Method. Computational Methods and Experimental Measurements **VIII**, 45.

Moore, A., L., and Shi, L. (2014). Emerging challenges and materials for thermal management of electronics. Materials Today **17**, 163

Netzsch (2018). Thermische Charakterisierung von Polymeren. Homepage of Netzsch (Deustchland), https://www.netzsch-thermal-analysis.com/de/, state: 08.06.2018

Okoli, O., I., Smith, G., F. (2000). The effect of strain rate and fibre content on the Poisson's ratio of glass/epoxy composites. Composite Structures **48**, 157

Reuss, A. (1929): Berechnung der Fließgrenze von Mischkristallen auf Grund der Plastizitätsbedingung für Einkristalle. Zeitschrift für Angewandte Mathematik und Mechanik **9**, 49

Tuttle, M., E. (2004) Structural Analysis of Polymeric Composite Materials. Second edition. CRC/Taylor & Francis

Tao, Q. (2018). Press Cycle Time Reduction of A Reinforced Epoxy Resin and the Influence On Its Mechanical/Thermal Properties. PhD thesis, Institute of Material Science and Testing of Polymers, Montanuniversität Leoben, A

Tao, Q., Krivec, T., Riedler, M. and Frewein, M. (2018). Comparison of finite elements based thermal shock test reliability assessment with a specimen based test approach. IPC APEX EXPO 2018. San Diego

Strommel, Markus, Stojek, Marcus, Korte, Wolfgang (2011). FEM zur Berechnung von Kunststoff- und Elastomerbauteilen. Carl Hanser Verlag GmbH & Co. KG

Sutton, M. A., Wolters, W. J., Peters, W. H., Ranson, W. F., McNeill, S. R. (1983). Determination of displacements using an improved digital correlation method. Image and Vision Computing **1**, 133.

Voigt, W. (1889). Über die Beziehung zwischen den beiden Elasticitätsconstanten isotroper Körper. Annalen der Physik, **274**, 573

Zukowski, E., Kimpel, T., Kraetschmer, D. and Roessle, A. (2015). Efficient modeling of printed circuit boards structures for dynamic simulations. 16th International Conference on Thermal, Mechanical and Multi-Physics Simulation and Experiments in Microelectronics and Microsystems (EuroSimE 2015)

Zündel, J., V. (2018): Characterization and modeling of the cure-induced shrinkage of an epoxy resin used in organic laminate based electronic modules. Master thesis, Institute of Material Science and Testing of Polymers, Montanuniversität Leoben, A

APPENDIX

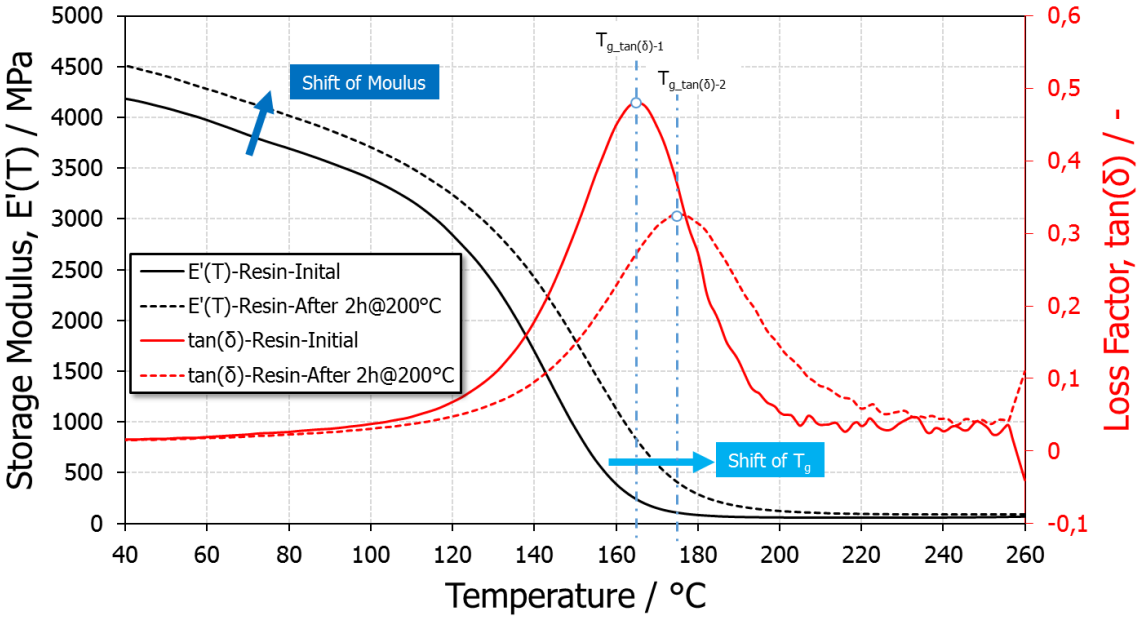

Figure A-1: Storage modulus and loss factor over temperature of two different conditioned resin specimens from the same resin board with depicted shift of the T_g.

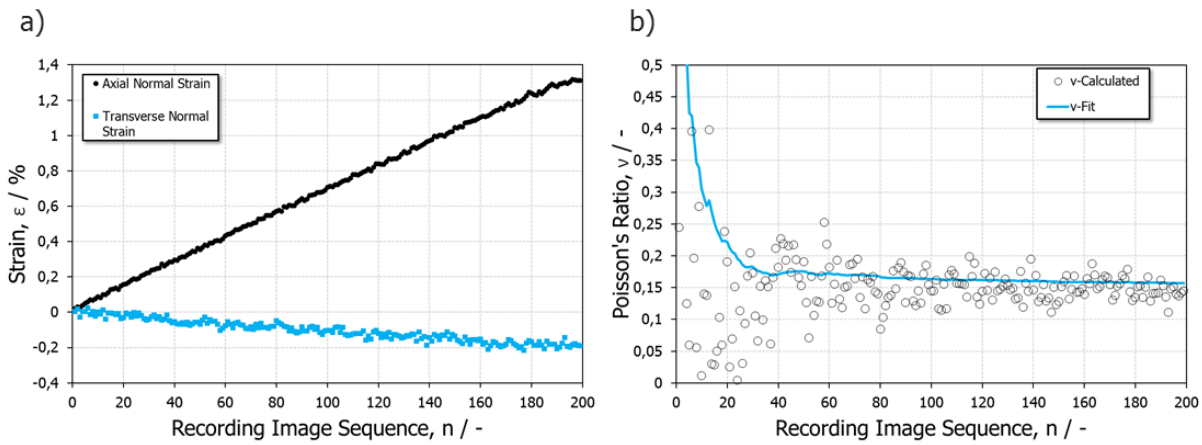

Figure A-2: a) Measured axial normal and transverse normal strain over recording image sequence from DIC. b) Optimized Poisson's ratio fitting.

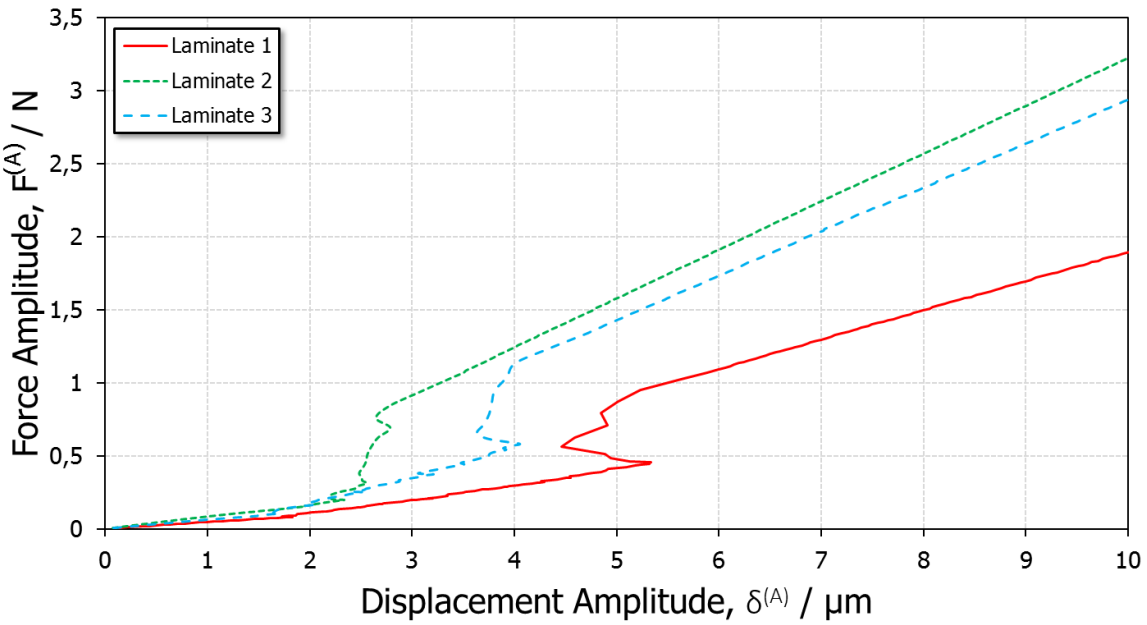

Figure A-3: Force scan results of the laminate specimens.

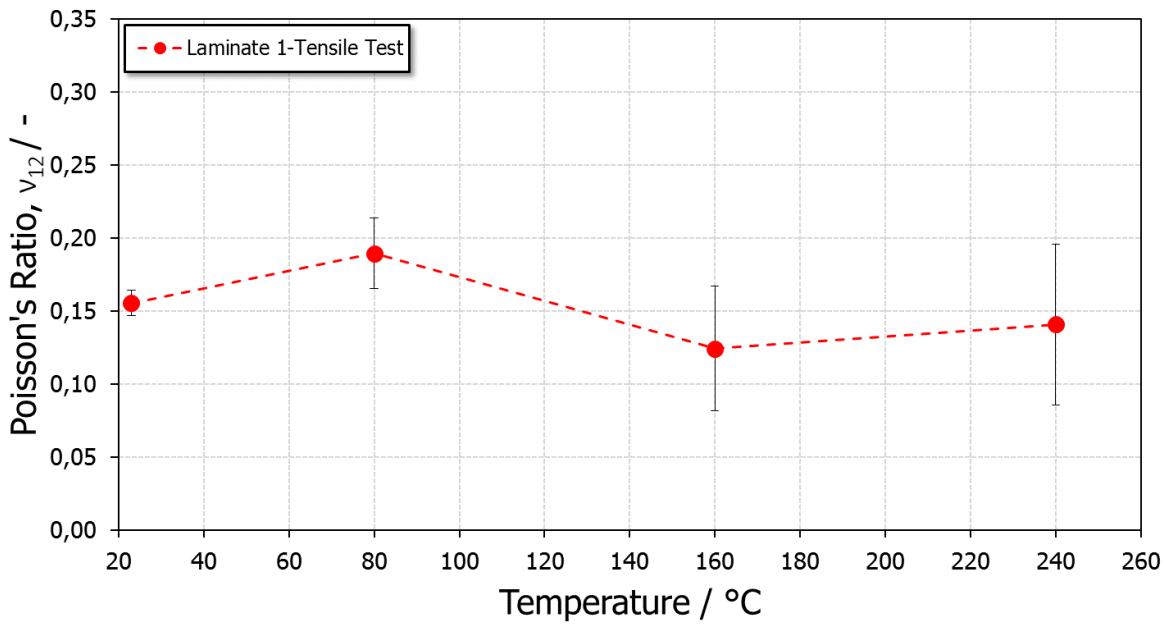

Figure A-4: In-plane Poisson's ratio of laminate 1 depicted with increasing standard deviation over the temperature.

Figure A-5: Fractured specimens after the monotonic tensile test at room temperature and elevated temperatures.

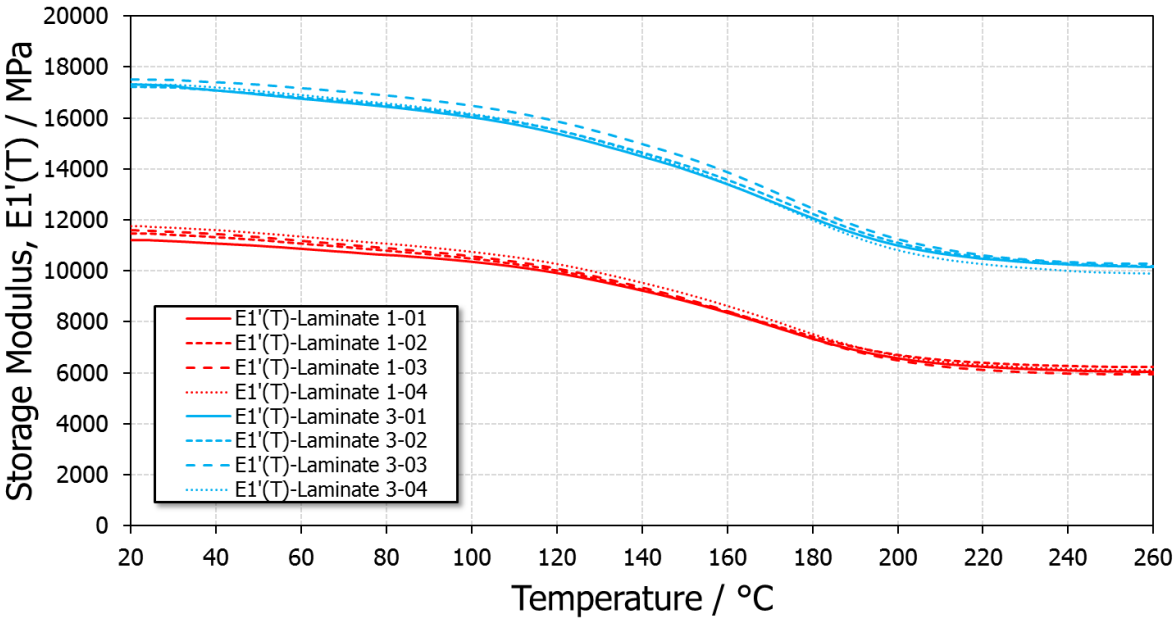

Figure A-6: Storage modulus results in direction 1 from laminate 1 and 3 obtained by DMA.

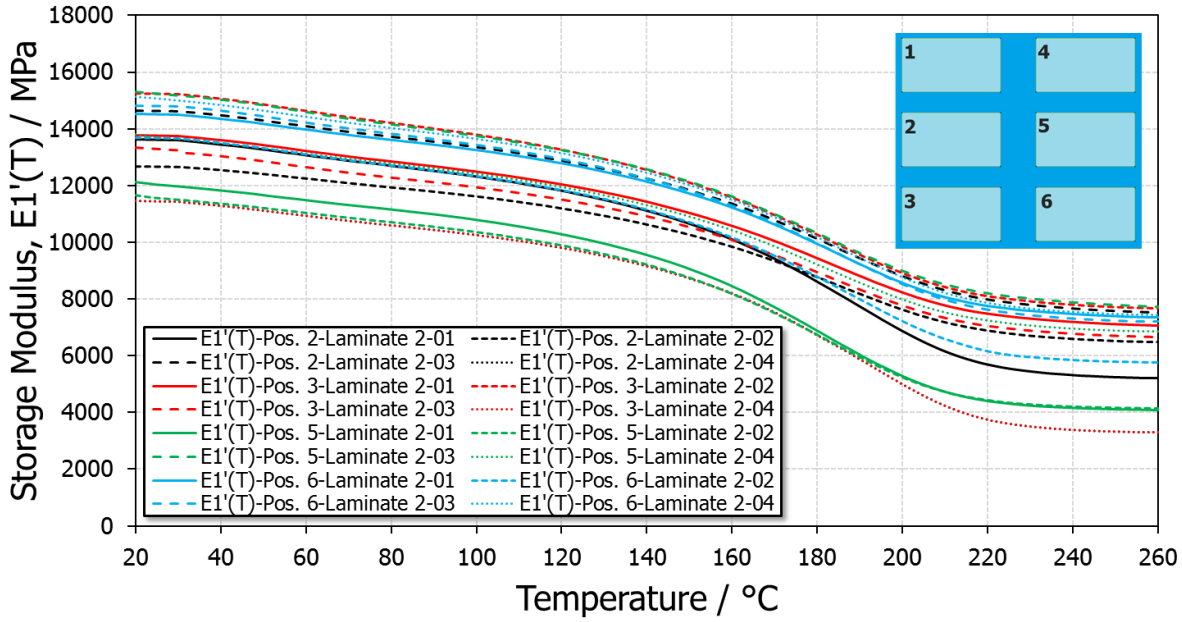

Figure A-7: Storage modulus results in direction 1 from laminate 2 obtained by DMA.

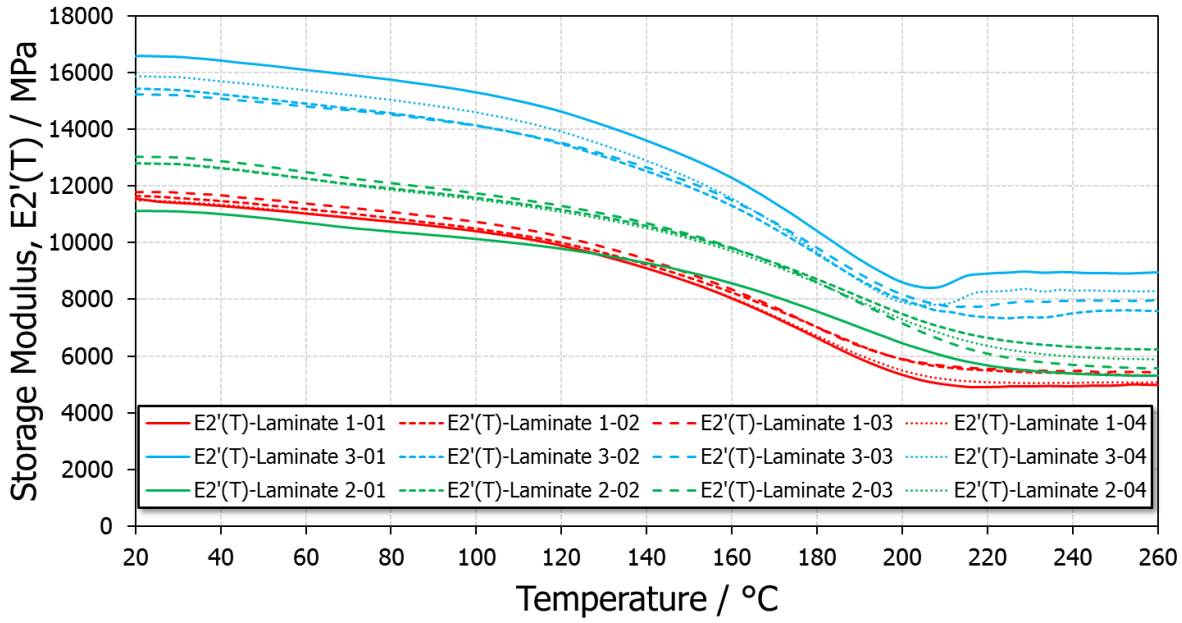

Figure A-8: Storage modulus results in direction 2 from laminate 1, 2 and 3 obtained by DMA.

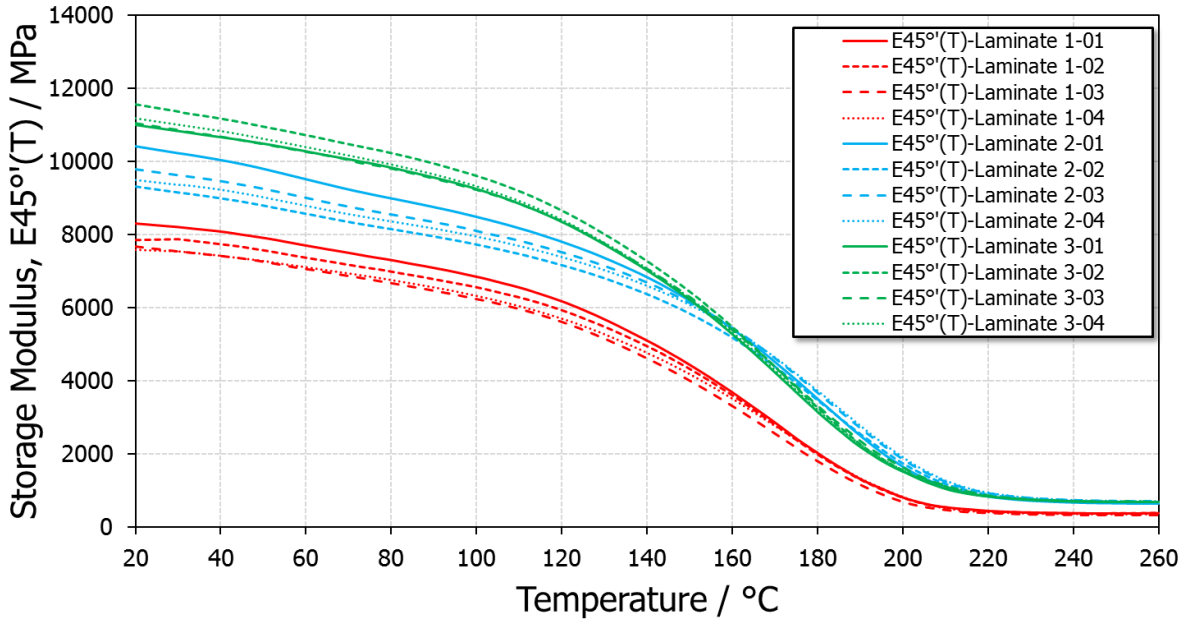

Figure A-9: Storage modulus results in direction 45° from laminate 1, 2 and 3 obtained by DMA.

Table A-1: Measured individual and mean results with standard deviations from the cross sectioning in direction 1.

		Lamiante 1		**Lamiante 2**		**Lamiante 3**	
		Yarn Height	Yarn Width	Yarn Height	Yarn Width	Yarn Height	Yarn Width
		[µm]	[µm]	[µm]	[µm]	[µm]	[µm]
		13,01	308,94	13,04	136,52	31,71	443,90
		14,63	365,85	12,17	115,65	28,70	501,63
		12,20	343,90	13,91	125,22	29,57	460,16
		12,42	408,35	18,26	141,74	31,71	413,82
		11,04	391,80	13,91	134,78	33,91	440,65
		18,62	283,50	13,91	164,35	22,61	427,64
Mean (SD)	[µm]	13,65 (2,47)	350,39 (43,87)	14,20 (1,92)	136,38 (15,10)	30,08 (1,76)	447,97 (27,92)
Aspect Ratio	[-]	25,7		9,6		14,9	

Table A-2: Measured individual and mean results with standard deviations from the cross sectioning in direction 2.

		Lamiante 1		Lamiante 2		Lamiante 3	
		Yarn Height	Yarn Width	Yarn Height	Yarn Width	Yarn Height	Yarn Width
		[µm]	[µm]	[µm]	[µm]	[µm]	[µm]
		20,23	152,03	8,28	315,92	31,71	365,04
		19,51	169,92	11,73	298,68	28,7	289,57
		19,51	160,16	9,66	380,7	29,57	294,78
		19,51	143,09	12,42	321,44	31,71	297,56
		19,51	165,85	14,49	290,4	33,91	257,39
		22,76	120,33	12,42		22,61	251,3
Mean (SD)	[µm]	20,17 (1,18)	151,90 (16,64)	11,50 (2,02)	323,50 (29,30)	29,71 (3,58)	292,61 (37,04)
Aspect Ratio	[-]	7,5		28,1		9,9	

Table A-1: All individual results obtained by the monotonic tensile test. The Materils depicted with R for resin, A for laminate 1, B for laminate 2 and C for laminate 3.

Material	Temperature	Direction / Position	Measurement Specimen Name	Fracture Strain	Fracture Stress	Young's Modulus	Poisson's ratio
[-]	[°C]	[-]	[-]	[%]	[MPa]	[MPa]	[-]
Resin	23	-	R1-RT	2,03	78	4927	0,327
			R2-RT	2,21	80	4801	0,321
			R3-RT	2,30	80	4873	0,327
			R4-RT	2,26	80	4931	0,316
	80		R5-80	4,17	60	3901	0,349
			R6-80	3,92	59	3825	0,350
			R7-80	4,14	61	3692	0,363
			R8-80	3,90	60	3812	0,356
	120		R17-120	2,84	33	2589	0,387
			R18-120	3,22	31	2423	0,365
			R19-120	3,38	34	2637	0,418
			R20-120	3,25	32	2398	0,463
	160		R9-160	7,85	14	415	0,454
			R10-160	1,46	5	347	0,473

			R11-160	3,16	7	315	0,471
			R12-160	3,10	8	392	0,477
	200		R21-200	2,89	3	91	0,495
			R22-200	2,92	3	102	0,466
			R23-200	3,39	4	104	0,527
			R24-200	2,94	3	103	0,458
	240		R13-240	2,29	2	85	0,443
			R14-240	2,88	3	87	0,464
			R15-240	3,05	3	89	0,481
			R16-240	2,47	2	91	0,490
Laminate 1	23	1	A1-RT-1	1,39	152	12612	0,151
			A1-RT-2	1,48	165	13099	0,143
			A1-RT-3	1,45	165	12758	0,164
			A1-RT-4	1,47	165	13308	0,164
	80	1	A1-80-1	1,42	139	11309	0,178
			A1-80-2	1,62	156	10127	0,158
			A1-80-3	1,48	149	11400	0,200
			A1-80-4	1,22	128	11553	0,223
	160	1	A1-160-1	1,57	118	7299	0,081
			A1-160-2	1,40	110	7425	0,126
			A1-160-3	1,46	122	7349	0,097
			A1-160-4	1,48	118	7470	0,193
	240	1	A1-240-1	1,20	91	6928	0,188
			A1-240-2	1,14	78	6698	0,096
			A1-240-3	1,21	83	6672	0,202
			A1-240-4	0,97	68	6808	0,077
	23	2	A2-RT-1	1,20	133	12732	0,150
			A2-RT-2	1,20	133	12362	0,212
			A2-RT-3	0,97	111	12418	0,187
			A2-RT-4	1,20	133	12293	0,166
	80	2	A2-80-1	1,55	144	10577	0,143
			A2-80-2	1,39	131	11120	0,161

			A2-80-3	1,30	128	11038	0,229
			A2-80-4	1,31	130	11006	0,216
	160	2	A2-160-1	1,65	115	6885	0,129
			A2-160-2	1,47	95	6635	0,120
			A2-160-3	0,52	37	6901	0,134
			A2-160-4	1,55	106	6781	0,199
	240	2	A2-240-1	1,26	73	6062	0,371
			A2-240-2	1,29	73	5948	0,245
			A2-240-3	1,20	73	6192	0,200
			A2-240-4	1,22	73	6125	0,191
	23	45°	A3-RT-2	2,58	107	8242	0,472
			A3-RT-3	2,41	110	8587	0,546
			A3-RT-4	2,43	104	8125	0,493
Laminate 2	23	1 / A2	B1A2-RT-1	1,14	141	13965	0,173
			B1A2-RT-2	0,99	124	13686	0,163
			B1A2-RT-3	1,07	130	13660	0,120
			B1A2-RT-4	1,52	181	14139	0,163
	23	1 / A3	B1A3-RT-1	1,48	169	13875	0,173
			B1A3-RT-2	1,18	147	14175	0,220
			B1A3-RT-3	1,67	188	13850	0,160
			B1A3-RT-4	1,69	186	12747	0,169
	23	1 / A5	B1A5-RT-1	0,85	100	13249	0,268
			B1A5-RT-2	1,76	194	13757	0,163
			B1A5-RT-3	0,85	100	13054	0,174
			B1A5-RT-4	0,81	101	13232	0,143
	23	1 / A6	B1A6-RT-1	1,32	152	13675	0,168
			B1A6-RT-2	1,58	180	13709	0,168
			B1A6-RT-3	1,74	195	14205	0,161
			B1A6-RT-4	1,71	191	14011	0,172
	80	1	B1-80-1	1,64	164	11155	0,146
			B1-80-2	1,78	179	11397	0,154
			B1-80-3	1,71	174	11255	0,174

			B1-80-4	1,79	179	11955	0,180
	160	1	B1-160-1	1,74	138	7727	0,095
			B1-160-2	1,60	131	8274	0,268
			B1-160-3	1,67	143	8467	0,161
			B1-160-4	1,71	147	8906	0,164
	240	1	B1-240-1	1,42	103	7310	0,075
			B1-240-2	1,17	73	6354	0,094
			B1-240-3	1,00	67	6549	0,087
			B1-240-4	1,39	102	7634	0,135
	23	2	B2-RT-1	1,61	183	13942	0,187
			B2-RT-2	1,25	149	13890	0,144
			B2-RT-3	1,47	167	13603	0,145
			B2-RT-4	1,71	190	13787	0,167
	80	2	B2-80-1	1,66	164	11363	0,136
			B2-80-2	1,88	184	11359	0,222
			B2-80-3	1,70	170	11967	0,184
			B2-80-4	1,70	165	11119	0,142
	160	2	B2-160-1	1,75	134	7633	0,089
			B2-160-2	1,76	141	7685	0,126
			B2-160-3	1,92	147	7613	0,164
			B2-160-4	1,58	122	7546	0,165
	240	2	B2-240-1	1,20	83	6784	0,107
			B2-240-2	1,32	89	6693	0,216
			B2-240-3	1,20	78	6707	0,088
			B2-240-4	1,44	99	6985	0,131
	23	45°	B3-RT-1	2,78	119	9522	0,572
			B3-RT-2	2,99	113	9351	0,549
			B3-RT-3	2,51	118	9449	0,572
			B3-RT-4	2,26	100	9304	0,511
Laminate 3	23	1	C1-RT-1	1,61	227	18358	0,166
			C1-RT-2	1,45	216	18875	0,165
			C1-RT-3	1,56	225	19069	0,141

			C1-RT-4	1,52	221	18751	0,180
	80	1	C1-80-1	1,61	232	16403	0,197
			C1-80-2	1,32	200	16279	0,150
			C1-80-3	1,53	235	16713	0,248
			C1-80-4	1,50	215	16247	0,146
	160	1	C1-160-1	1,49	177	12072	0,197
			C1-160-2	1,59	192	12201	0,147
			C1-160-3	1,43	186	12752	0,150
			C1-160-4	1,48	183	12268	0,120
	240	1	C1-240-1	0,85	103	12069	0,273
			C1-240-2	1,16	142	11880	0,187
			C1-240-3	1,19	139	12156	0,197
			C1-240-4	1,19	137	11376	0,231
	23	2	C2-RT-1	1,36	180	16292	0,153
			C2-RT-2	1,31	177	17403	0,147
			C2-RT-3	1,42	185	17227	0,152
			C2-RT-4	1,34	181	17651	0,177
	80	2	C2-80-1	1,32	174	15130	0,182
			C2-80-2	1,38	183	15348	0,123
			C2-80-3	1,36	182	15252	0,156
			C2-80-4	1,33	177	13584	0,143
	160	2	C2-160-1	1,52	153	10060	0,199
			C2-160-2	1,23	127	10170	0,209
			C2-160-3	1,49	153	10286	0,139
			C2-160-4	1,20	121	9039	0,293
	240	2	C2-240-1	1,29	110	9059	0,444
			C2-240-2	1,23	107	9196	0,319
			C2-240-3	0,97	98	9620	0,389
			C2-240-4	1,16	110	9734	0,257
	23	45°	C3-RT-1	2,79	129	11452	0,592
			C3-RT-2	2,85	133	10464	0,598
			C3-RT-3	3,47	144	11845	0,612

			C3-RT-4	3,27	133	12396	0,610